ABSTRACT

Title of Dissertation: DEVELOPMENT OF COOLING SYSTEMS WITH ACTIVE ELASTOCALORIC REGENERATORS

By David Catalini, Doctor of Philosophy, 2021

Dissertation directed by: Minta Martin Professor Reinhard Radermacher Department of Mechanical Engineering

The vapor compression cycle (VCC) has been developed and optimized over a century to provide cooling in residential and commercial buildings, and transport systems. However, its usage has resulted in unpredicted environmental damage such as depleting the ozone layer and promoting global warming when its refrigerant leaks into the atmosphere. Because of this, it is important to develop a superior technological alternative without the environmental costs. One way to tackle this problem is to develop heat pumping cycles using solid-state refrigerant since a solid is incapable of leaking into the atmosphere. However, a solid-refrigerant cannot flow to deliver cooling the same way a fluid-refrigerant does. This requires a system conceptual redesign, which started with near-room temperature cooling with magnetocaloric materials in 1976 and elastocaloric materials in 2012.

In this work, four different system configurations were studied with the following objectives: 1) maximizing the system's temperature lift and 2) measuring the cooling capacity as a function of the useful temperature lift of the system when operating as a water chiller. The first configuration was based on the thermowave heat recovery strategy, while the other three were based on a single stage, two-stage and reciprocating variants of the active regeneration cycle. From the studied configurations the thermowave-based cycle achieved a system's temperature lift of 8 K, at large average strain of 4.5%. It produced a maximum useful temperature lift of 5 K and a maximum cooling capacity of 125 W. All active regeneration-based cycles achieved similar final results while the best results was a system's temperature lift of 21.3 K at a low average strain of 3.5% and a maximum useful temperature lift of 6.5 K and a maximum cooling capacity between 16 W and 25 W. The advantage of the reciprocating system integration is that it can achieve these results at lower strain than the one- stage and two-stage configurations.

This dissertation identified a fundamental limitation of the active regeneration cycles using single composition elastocaloric materials. It is due to the fact that the local strain is larger than the average strain where the temperature is lower, which limits the maximum applicable average strain to prevent premature failure. This directly affects both the temperature lift and cooling capacity of the system. Different alternatives to address this issue, as well as how to improve the overall thermal and structural performance of the system within the constraints of the materials commercially available are suggested.

DEVELOPMENT OF COOLING SYSTEMS WITH ACTIVE ELASTOCALORIC REGENERATORS

by

David Catalini

Dissertation submitted to the Faculty of the Graduate School of the
University of Maryland, College Park, in partial fulfillment
of the requirements for the degree of
Doctor of Philosophy
2021

Advisory Committee:
Professor Reinhard Radermacher, Chair
Research Professor Yunho Hwang
Professor Ichiro Takeuchi
Professor Olivier Bauchau
Professor Marino di Marzo
Professor Bao Yang
Chun-Cheng Piao, Ph.D.

Dedication

To my wife, Nadine.

Acknowledgements

This turned out to be a very hard section to write. So many people helped me get to this point, that did so much for me, that a page is not enough to list them all. Their influence goes beyond the limits of what I wrote next and I will be in debt to them for the rest of my life, even if I could not list them all individually.

I would like to thank Prof. Reinhard Radermacher for always leading by example, his intellectual and professional generosity, and for helping me pursue my dreams in a way that made me grow while adding value to my colleagues and students; Prof. Ichiro Takeuchi for his trust, encouragement, openness and vision for this project; Prof. Yunho Hwang for his effort and dedication in managing the progress of this project, his advice and for his invaluable help in revising this manuscript; the committee members for taking the time to review this dissertation and their insightful feedback; Jan Muehlbauer for the time he spent teaching me and answering all my questions; Prof. Suxin Qian, for receiving me at Xi'an Jiaotong University, for helping me understand elastocaloric cooling and develop the numerical model I used in this work; Mary for always helping me get every administrative thing done fast even when I gave her short notice; my colleagues at the Center for Environmental Energy Engineering for having fun with me all these years.

I want to thank Glenn and Terri Grant, for their continuous enthusiasm, for their support, for being an example of generosity and love, and for allowing me to be a part of their lives.

I want to thank Jun Cui, for always encouraging and helping me to grow, professionally and personally and for showing me that it is possible to set and achieve the highest goals and then continue to the next.

I would not be here without the love of my family in Argentina either, not only during the last four years but during all my life. Year after year of support, of giving and teaching me everything, for being with me always and particularly when I needed them the most. They are always on my mind. It is also hard to imagine how going through this program would have been without the continuous support, understanding and encouragement of my family in United States.

I would also like to acknowledge the Energy Efficiency and Heat Pumps Consortium at CEEE, Engie, The Graduate School and ARPA-e for their financial support.

I would like to acknowledge the University of Maryland, for providing with the environment for some of the best memories of my life.

Table of Contents

List of Tables

List of Figures

Nomenclature

A_f	Austenite finish temperature	[K]
A_s	Austenite start temperature	[K]
CHEX	Cold side heat exchanger	
$c_{p,f}$	Heat capacity of heat transfer fluid	[J kg^{-1} K^{-1}]
C_r*	Heat capacitance ratio	[-]
DAQ	Data acquisition	
D_h	Hydraulic diameter	[m]
δQ	Heat	[J]
δW	Work	[J]
ε	Effectiveness	[-]
e	Strain	[-]
E_A	Austenite Young's modulus	[Pa]
e_{HR}	Heat recovery efficiency	[-]
E_M	Martensite Young's modulus	[Pa]
e_T	Martensitic transformation strain	[-]
G	Gibbs free energy	[J]
G^{gen}	Generalized Gibbs free energy	[J]
Gz_D	Graetz number	[-]
H	Enthalpy	[J]
h	Heat transfer coefficient	[W m^{-2} K^{-1}]
HEX-A	Heat exchanger A	
HEX-C	Heat exchanger C	
H^{gen}	Generalized enthalpy	[J]
HHEX	Hot side heat exchanger	
HRV	Heat recovery valve	
k_f	Thermal conductivity of heat transfer fluid	[W m^{-1} K^{-1}]
k_s	Thermal conductivity of solid	[W m^{-1} K^{-1}]
M_f	Martensite finish temperature	[K]
$\dot{m}_f$	Mass flow rate of heat transfer fluid	[kg s^{-1}]
MFM	Mass flow meter	
M_s	Martensite start temperature	[K]
Ni-Ti	Nickel-Titanium	
NTU_0	Number of heat transfer units	[-]

Nu_D	Nusselt number	[-]
P	Pressure	[Pa]
P→M	Parent phase to Martensite	
PEEK	Polyetheretherketone	
P_H	High side pressure	[Pa]
P_L	Low side pressure	[Pa]
PRV	Pressure relief valve	
PTFE	Polytetrafluoroethylene	
Pump C	Cold water loop pump	
Pump H	Hot water loop pump	
Pump HR	Heat recovery pump	
$\dot{Q}$	Cooling capacity	[W]
ρ_f	Density of heat transfer fluid	[kg m^{-3}]
S	Entropy	[J K^{-1}]
σ	Stress	[Pa]
SMA	Shape memory alloy	
SV1	Solenoid valve 1	
SV2	Solenoid valve 2	
SV3	Solenoid valve 3	
SV4	Solenoid valve 4	
T	Temperature	[K]
T_{amb}	Ambient temperature	[K]
T_C	Temperature of cold side/heat reservoir	[K]
T_H	Temperature of hot side/heat sink	[K]
t_{HT}	Heat transfer time	[s]
U	Internal energy	[J]
V	Volume	[m^3]
V*	Utilization factor	[-]
V1	Solenoid valve 1	
V2	Solenoid valve 2	
V3	Solenoid valve 3	
V4	Solenoid valve 4	
V5	Solenoid valve 5	
V6	Solenoid valve 6	
V7	Solenoid valve 7	
V8	Solenoid valve 8	
VCC	Vapor compression cycle	
wt.%	Weight percentage	

Chapter 1: Introduction

The vapor compression cycle (VCC) has been developed and optimized over the last 100 years to provide cooling in buildings (residential and industrial) and vehicles. However, its usage has resulted in unpredicted environmental damage such as depleting the ozone layer and promoting global warming when the refrigerant fluid leaks into the atmosphere. Because of this, it is important to replace the VCC by developing a superior technological alternative without the environmental costs. One way to tackle this problem is to develop heat pumping cycles using solid-state refrigerants instead of refrigerant fluids: a solid is incapable of leaking into the atmosphere. These solid-state refrigerants are called caloric materials.

1.1 General description of cooling with the vapor compression cycle

Refrigerant fluids like R-134a or R-410A are substances that exist in vapor state at normal pressure and temperature conditions. In the most fundamental configuration, a cooling system is a closed circuit consisting of a compressor, a heat exchanger called the condenser where heat is rejected to ambient, an expansion valve and another heat exchanger called the evaporator where heat is absorbed to cool the conditioned space. To supply cooling, the vapor goes through the system following four steps, as shown schematically in Figure 1:

1. The saturated vapor goes through the compressor. During this step it increases its pressure and temperature to become a superheated vapor.
2. The superheated vapor, still at high pressure, goes through the condenser. During this step it rejects latent heat of condensation at constant temperature and pressure, until the vapor becomes a saturated liquid. There is a decrease in entropy during this step due to the phase transition from vapor to liquid.
3. The pressurized saturated liquid goes through an expansion valve. During this step the pressure is suddenly decreased and some of the liquid evaporates resulting in a mixture of liquid and vapor. With no heat transfer at the expansion valve, the energy required for the phase transformation to take place comes at the expense of the internal energy of the liquid and vapor mixture, and thus the temperature decreases.
4. The liquid-vapor mixture goes through the evaporator. During this step the mixture absorbs heat from the conditioned space, allowing the rest of the liquid to evaporate until becomes a saturated vapor and is ready to restart the cycle.

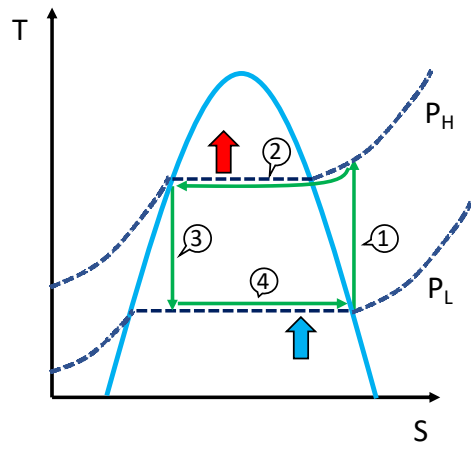

Figure 1: Schematic of the vapor compression cycle

The temperature difference between the pressurized liquid and the liquid and vapor mixture after the expansion valve is the temperature lift of the system, and the amount of heat per unit of time that is absorbed at the evaporator is the cooling capacity. These quantities are two of the main values used to evaluate the capabilities of the system. Schematically, and maintaining all other variables constant, the relationship between the two is similar to what is shown in Figure 2: when no heat is absorbed (i.e., no cooling is supplied) the temperature lift is at a maximum, and the maximum cooling capacity would be achieved when the temperature lift is equal to zero. This can be seen in the schematic in Figure 2, and it will be the way cooling performance is evaluated in the current work.

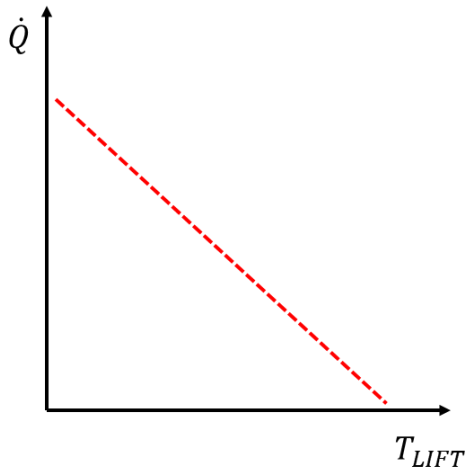

Figure 2: Schematic of cooling capacity and temperature lift relationship

1.2 General perspective of cooling with caloric materials

1.2.1 Caloric materials and entropy

Caloric materials experience a significant change in entropy with the application of an external field at temperatures around room temperature. The entropy change manifests itself as a change in material's temperature when the external field is applied or removed adiabatically; or as a latent heat exchange between the material and the surroundings when the external field is applied or removed isothermally. By integrating the material into a thermodynamic heat pumping cycle, it is possible to supply cooling.

Plainly stated, the entropy change is the energy cost that needs to be paid to go from a low entropy state to a high entropy state, or the energy reimbursement that comes associated with going from a high entropy state to a low entropy state. There is no way around it: when the transition is made isothermally, this energy comes from the surroundings as a heat transfer; and when the transition is made adiabatically, this energy comes from the materials own thermal energy.

In refrigerant fluids, the high entropy state is the vapor state, while the low entropy state is the liquid state. We are most familiar with this type of transition and we know that to effectively evaporate a liquid by heating, at the boiling point we need to supply an additional amount of heat, the latent heat of evaporation, required to force the liquid molecules to break their bonds to separate from each other and become a vapor. And we are also familiar with the reverse process, condensation, and we understand that when the vapor gives up its freedom to become a condensed, liquid phase, it gives back the same latent heat. In the case of elastocaloric materials, the low entropy state is a solid-state phase,

and the high entropy state is also a solid phase. What does the entropy of a solid-state phase depend on? The fundamental definition of entropy is, from the thermal physics point of view, the "logarithm of the number of states accessible to the system" (Kittel, 1969). A system can be defined as a group of elements with a certain measurable property, and the number of states accessible to the system is the number of different configurations this group of elements can be arranged into. Consider the system being a group of elemental crystals with a certain crystallographic structure, it is possible determine their crystallographic orientation in space with respect to a frame of reference. If the crystallographic structure is highly symmetric there are more possible orientations for any elemental crystal that would give equivalent group configurations. This consequently results in a higher entropy value. If the symmetry of the crystallographic structure is lower, the number of possible orientations that would lead to equivalent arrangements is smaller, leading to a lower entropy value.

1.2.2 The martensitic transformation and elastocaloric materials

The change of entropy in elastocaloric materials is caused by a solid-state, diffusionless, phase transition called martensitic transformation. It is the process through which a high entropy phase transitions to a low entropy phase. In the specific case of the Ni-Ti alloy studied in this work, the forward transformation takes the material from Austenite to Martensite. Austenite, which has a body-centered cubic crystal structure, is the high entropy phase because the cubic crystal structure is one of high symmetry. Martensite, which has a monoclinic crystal structure, is the low entropy phase (Brantley et al., 2017). In a diffusionless transformation there is no long-range movement of atoms, in fact, less

than one interatomic spacing. The mechanism that enables this to happen is a shear strain that deforms the parent phase crystallographic structure into the one of the martensite.

While the high entropy phase is stable at high temperatures, the low entropy phase is stable at low temperatures and because of this the phase transition can be induced by cooling. A particularity of elastocaloric materials is that this transition can be reversed by heating.

From the thermodynamic point of view, the description of the equilibrium properties of a two-phase equilibrium like the one between parent and martensite phase is similar to that of the allotropic transformation of a pure element. At constant pressure the thermodynamic equilibrium temperature is defined unambiguously as the temperature at which the Gibbs free energy of the two homogeneous allotropic phases has the same value (Wollants et al., 1993). In practice, however, the forward transformation starts at a temperature M_s (Martensite Start) and it finishes at a lower temperature M_f (Martensite Finish). The reverse transformation starts at a temperature A_s (Austenite Start), and it ends at a higher temperature A_f (Austenite Finish). It is also experimentally observed that A_s is larger than M_f, and that M_s is lower than A_f, which is an indication that the transformation shows hysteresis. It is necessary a certain supercooling to drive the forward transformation, and a certain superheating to drive the reverse transformation. The change in entropy between the parent and the martensitic phase, between the high entropy phase and low entropy phase, can be effectively measured through calorimetry. This is shown schematically in Figure 3.

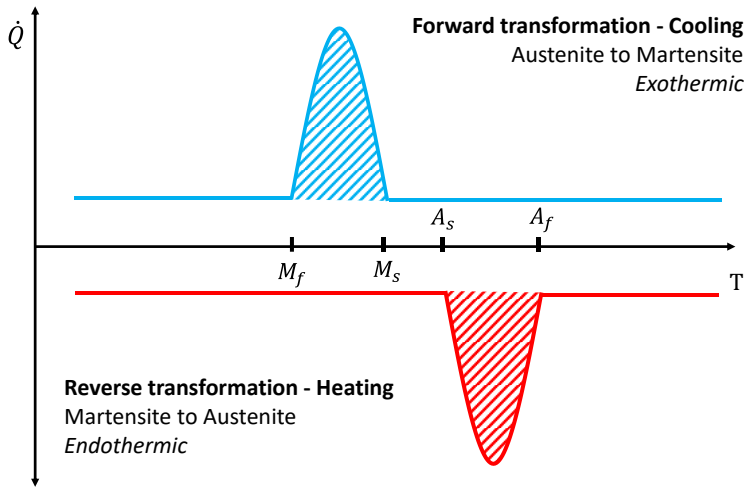

Figure 3: Schematic of differential scanning calorimetry of a thermally induced martensitic transformation

Figure 4 shows an optical micrograph capturing the microstructural visual characteristics of the martensite phase in a Cu -14.2 wt.% Al - 4.2 wt.% Ni alloy (the original photo was trimmed for proper fitting).

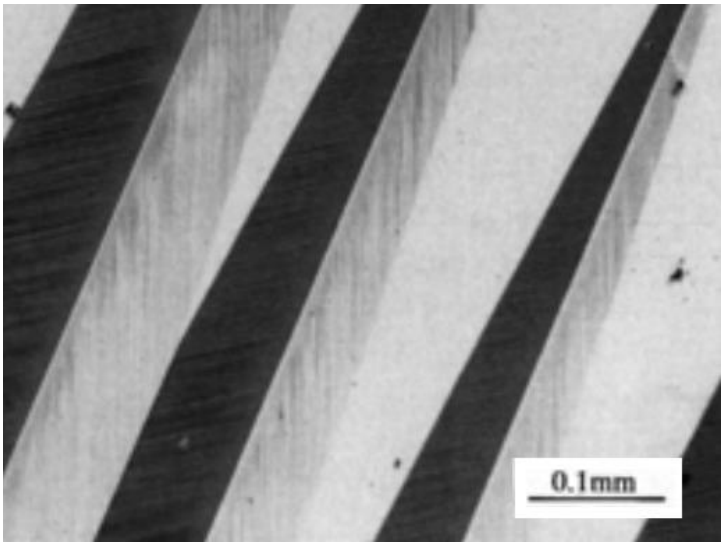

Figure 4: Optical micrograph of a martensite in a 81.6 wt.% Cu - 14.2 wt.% Al - 4.2 wt.% Ni alloy (Otsuka and Wayman, 1999)

As the transformation from Austenite's to Martensite's crystallographic structure, large shear strains need to be accommodated (Figure 5, subfigure a). There are microstructural shear mechanisms, like dislocation glide (Figure 5, subfigure b) and twinning (Figure 5, subfigure c), that allow the decrease of the lattice distortion during the transformation and that Figure 4 shows. At the end of the thermally induced martensitic transformation the microstructure is composed by a mixture of the different martensite variants.

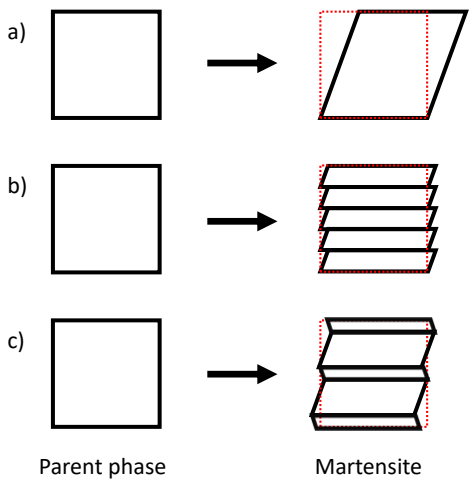

Figure 5: Lattice invariant shear mechanisms to reduce the lattice distortion

This shear strain can also be enforced by the application of a stress, as shown schematically in Figure 6. Depending on the stress, only one martensite variant will remain, that which corresponds to the most energetically favorable with respect to the applied stress.

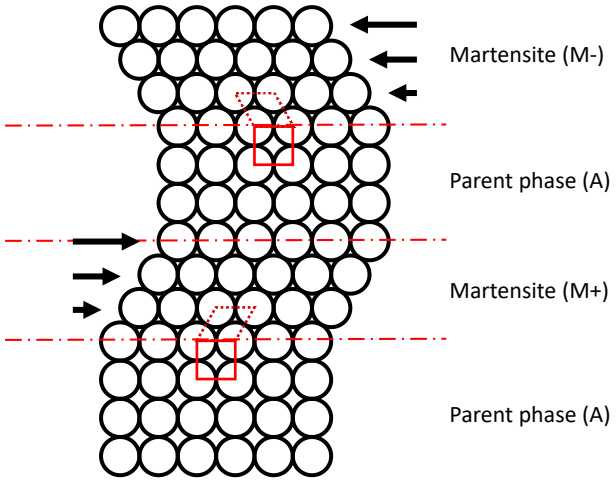

Figure 6: A simplified model of stress-induced martensitic transformation and martensite variants

1.2.3 Thermodynamics of stress-induced martensitic transformation

The procedure described in this section is based on published literature that it is worth revisiting briefly (Wollants et al., 1993). When considering the equilibrium between parent and martensitic phase in thermoelastic alloys it is necessary to introduce some modifications to the thermodynamic equations. The formulation of the first law of thermodynamics is stated in Equation 1 where "δW" represents a summation of all kinds of work that can be exchanged between the system and the surroundings. In the vapor compression cycle, the only way the refrigerant fluid exchanges work with the surroundings is by changing its volume during compression. The work term, P·dV, is referred to as PV-work. In solid state refrigerants, however, this term is not significant because condensed phases are essentially incompressible. These materials are able to exchange other types of work with the surroundings, like elastic work, magnetic work and electric work, so these need to be taken into consideration. The other quantities in the equation are U, which is the internal energy and Q which is heat.

$$dU = \delta Q + \delta W \qquad \text{Equation 1}$$

By applying the second law for a reversible process one obtains Equation 2 which is the primary fundamental equation of the generalized thermodynamic system, where T is the temperature, S is the entropy and Y_i and X_i are a pair of conjugate variables. In the case of elastic work, they can be stress and strain, or force and length, in the case of magnetic work they can be magnetic field and magnetization, and in the case of electric work they can be electric field and polarization.

$$dU = TdS - PdV + \sum_i Y_i dX_i \qquad \text{Equation 2}$$

Based on this formulation, the independent set of variables are S, V and X_i, but if the variables T, P and Y_i are preferred Equation 2 can be modified by taking advantage of this property, $d(TS) = TdS + SdT$, $d(PV) = PdV + VdP$ and $d(X_iY_i) = X_idY_i + Y_idX_i$ to obtain Equation 3.

$$d\left(U + PV - TS - \sum_i Y_i X_i\right) = -SdT + VdP - \sum_i X_i dY_i = dG^{gen} \qquad \text{Equation 3}$$

With this, one can define the "generalized Gibbs free energy function" as shown in Equation 4.

$$G^{gen} = U + PV - TS - \sum_i Y_i X_i = G - \sum_i Y_i X_i \qquad \text{Equation 4}$$

From Equation 1 and Equation 2, and using the same terms used to go from Equation 2 to Equation 3 and considering reversible processes at constant P (dP = 0), T (dT = 0) and Y_i ($dY_i = 0$) one can arrive at Equation 5.

$$(TdS)_{P,T,Y_i} = (\delta Q_{rev})_{P,T,Y_i} = d\left(U + PV - \sum_i Y_i X_i\right)_{P,T,Y_i} = dH^{gen}_{P,T,Y_i} \qquad \text{Equation 5}$$

Analogously to how the Gibbs free energy definition was generalized, the Enthalpy definition can be generalized:

$$H^{gen} = U + PV - \sum_i Y_i X_i = H - \sum_i Y_i X_i \qquad \text{Equation 6}$$

When two phases are in equilibrium at a certain set of (P, T, Y_i) values the condition in Equation 7 is satisfied, where ΔG^{gen} is the difference in Gibbs generalized free energy between the two phases. In the specific case of elastocaloric material: parent phase and martensite. Equation 7 also shows that for a particular value of (P, T) for which the ΔG is larger than zero, which means that the parent phase would be the stable phase, it should be possible via the application of work $\Sigma Y_i \Delta X_i$ to overcome this barrier and induce the transformation.

$$\Delta G^{gen} = 0 \rightarrow \Delta G = \sum_i Y_i \Delta X_i \qquad \text{Equation 7}$$

From Equation 5 and Equation 6 it can be concluded that the latent heat of the transformation equals the change of the generalized enthalpy function, as shown in Equation 8.

$$\Delta H_{T,P,Y_i}^{gen,P\rightarrow M} = \left(\Delta H - \sum_i Y_i \Delta X_i\right)_{T,P,Y_i}^{P\rightarrow M} = Q_{T,P,Y_i}^{P\rightarrow M} \qquad \text{Equation 8}$$

Now, for each combination of two natural independent variables, out of the set (P, T, Y_i), an equation similar to the original Clausius-Clapeyron equation can be obtained. For example, at constant hydrostatic pressure, the equation that links the equilibrium values of T and any of the intensive variables Y_i is shown in Equation 9.

$$\frac{dY_i}{dT} = \left(\frac{\Delta S}{\Delta X_i}\right)^{P\rightarrow M} = -\left(\frac{\Delta H^{gen}}{T\Delta X_i}\right)^{P\rightarrow M} \qquad \text{Equation 9}$$

Equation 9 is a general equation that can be applied to any set of conjugate variables that can express a work exchange between the material and the surroundings. The importance of this with respect to elastocaloric materials is that it states that the stress required to induce the transformation is a function of the temperature. As the temperature is further away from the equilibrium transition temperature, the larger the stress it is required to induce the transformation by stress.

1.2.4 Elastocaloric cooling

The way cooling is commonly demonstrated in elastocaloric materials is through the steps shown in Figure 7.

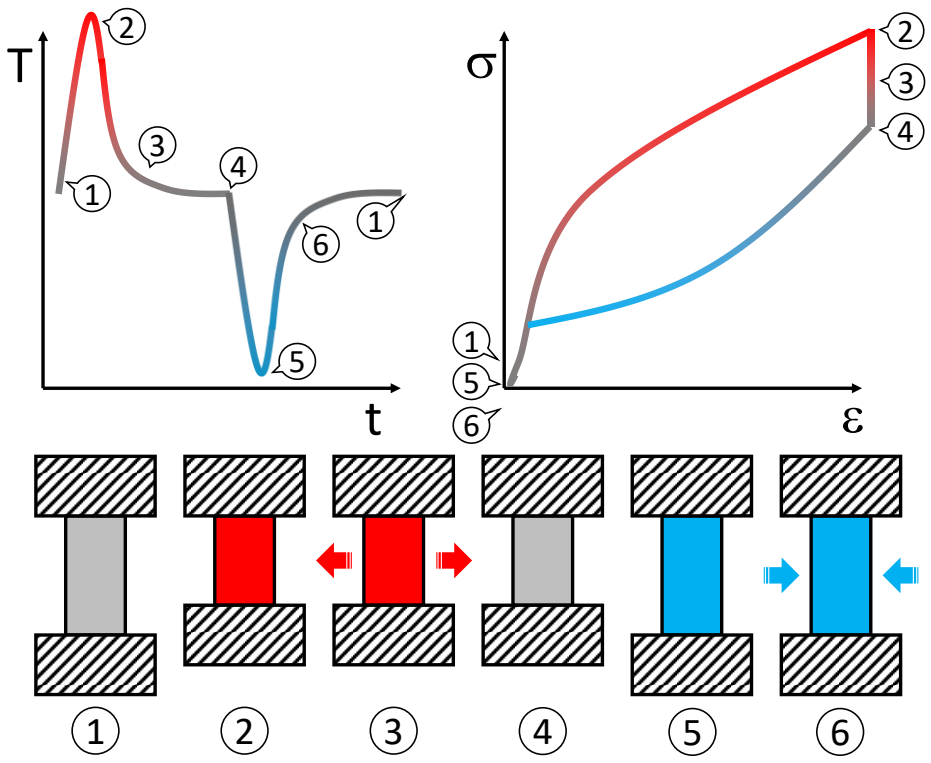

Figure 7: Sequence of steps in elastocaloric cooling

From the sequence 1 to 2 the material is stressed, and the martensitic transformation is induced. For this to happen it is necessary that the material is in the parent phase so the temperature must be higher than A_f. If this process is done adiabatically, the change in entropy results in an increase of the materials temperature. From the sequence 2 to 4 (a snapshot along the way is point 3) heat is rejected, with the stress still applied, until the material goes back to the starting temperature. From the sequence 4 to 5 the stress is

removed. Once this happens the transformation is reversed and if the stress is removed adiabatically, the entropy change will result in the materials decrease in temperature. From 5 to 6 the material can absorb heat and provide cooling.

These are the fundamental steps of elastocaloric cooling. More advanced thermodynamic cycles can be used to pump heat from a heat reservoir at temperature T_C to a heat sink at T_H. Internal heat recovery schemes can be applied to go beyond the adiabatic temperature change of the material and make the temperature lift of the system (T_H-T_C) as large as possible. Two examples of this are the reverse Brayton, shown in Figure 8, and Stirling cycles, shown in Figure 9.

The reverse Brayton cycle consists of two isentropic processes and two iso-stress processes.

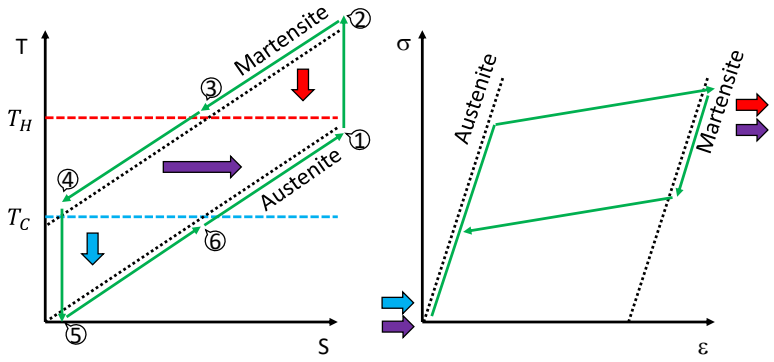

Figure 8: Reverse Brayton cycle

The cycle starts at state 1, with the elastocaloric material in austenitic phase. To reach state 2 the material is adiabatically stressed to induce the martensitic transformation. Because the loading was done adiabatically (isentropically) the material increases its temperature.

To reach step 3 the material rejects heat to the sink at T_H. To improve performance the material in step 3 is allowed to reject sensible heat with another material that is going through the cycle but is in step 6. In principle, it is thermodynamically possible to have a 100% efficiency in this process. With this assumption, the temperature in step 4 can be as low as the temperature in state 6 (and both equal to T_C), and the temperature is state 1 can be as high as the temperature in state 3 (and both equal to T_H). This would allow the temperature in state 4 to be the same as the temperature in state 6, and the temperature in state 1 to reach the same value as in state 3. This is the heat recovery process. Once in state 4, the material is ready be relieved of the stress and transform back to austenite adiabatically. During this step, the temperature of the material decreases and reaches state 5. To reach state 6 the material increases its temperature by absorbing heat from the heat source at T_C, and thus supplying cooling. To reach state 1 and return to the starting point, the material absorbs heat from another material that is going through the cycle and is in state 3.

The reverse Stirling cycle consists of two iso-stress heat transfer processes and two isothermal phase change processes. The cycle starts in state 1 and to reach state 2 the material is stressed while simultaneously rejects heat to the sink at T_H. This is necessary to maintain the temperature constant during the exothermic martensitic transformation. To reach state 3 it is necessary to reject heat with another set of material that is going through the cycle in state 4. This is a heat recovery process. To go from state 3 to state 4 the stress is removed while the material absorbs heat from the heat reservoir at T_C. To go from state 4 back to state 1, the material absorbs sensible heat from another material going through

the cycle at state 2. That completes the cycle. As shown, a heat recovery strategy is necessary to improve the performance of the system.

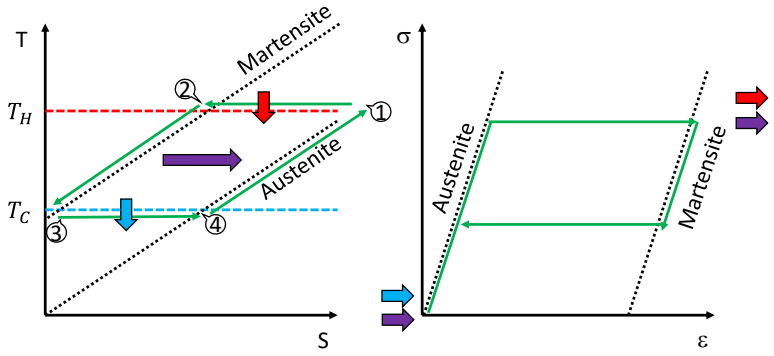

Figure 9: Reverse Stirling cycle

In practice, counterflow heat exchangers (also known as recuperators) are used for heat recovery processes with high efficiency. A recuperator allows a high temperature stream to be precooled, and a low temperature stream to be preheated by exchanging sensible heat with each other continuously through the recuperator wall. If the process had an effectiveness of 1 (or a 100% efficiency), the temperature of the high temperature stream at the outlet of the recuperator would be equal to the temperature of the low temperature stream at the inlet of the recuperator; and equivalently, the temperature of the low temperature stream at the outlet of the recuperator would be equal to the temperature of the high temperature stream at the inlet of the recuperator. This would be the case for an ideal recuperator, of infinite heat transfer area and infinite heat transfer coefficient.

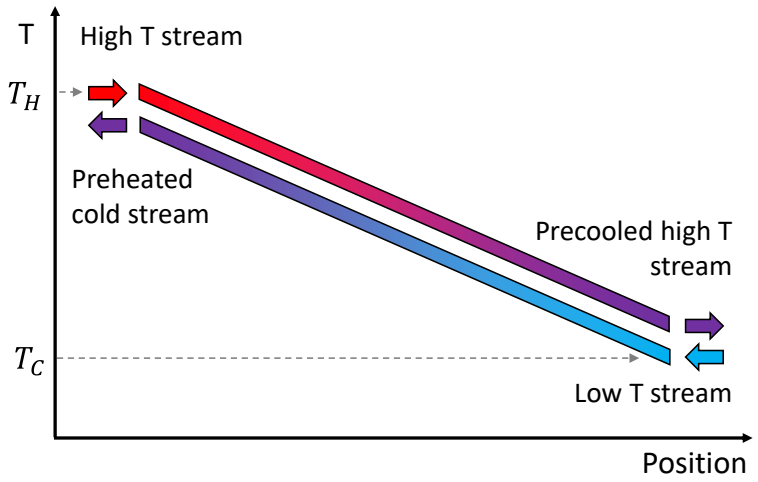

Figure 10: Schematic of steady state temperature profile along a recuperator

For systems in cyclic operation, a more appropriate alternative is having a regenerator (instead of a recuperator) in the system configuration. A regenerator is a storage-type heat exchanger. The heat transfer during the operation of a regenerator, as opposed to the recuperator, is intermittent. There are two main periods during a complete cycle: the hot blow period and the cold blow period. During the hot blow period the high temperature fluid flows through the regenerator passages and the thermal energy from the high temperature fluid is transferred to the regenerator. As a result, the fluid decreases its temperature while the regenerator increases it. During the cold blow period, the cold fluid flows in the opposite direction through the same passages and thermal energy stored in the regenerator is transferred to the fluid. As a result, the regenerator decreases its temperature while the fluid increases it. When the regenerator is in operation for long periods of time, after the initial transient, it reaches a periodic steady state. During each alternating period, hot and cold blow, the regenerator develops a characteristic time-dependent temperature gradient.

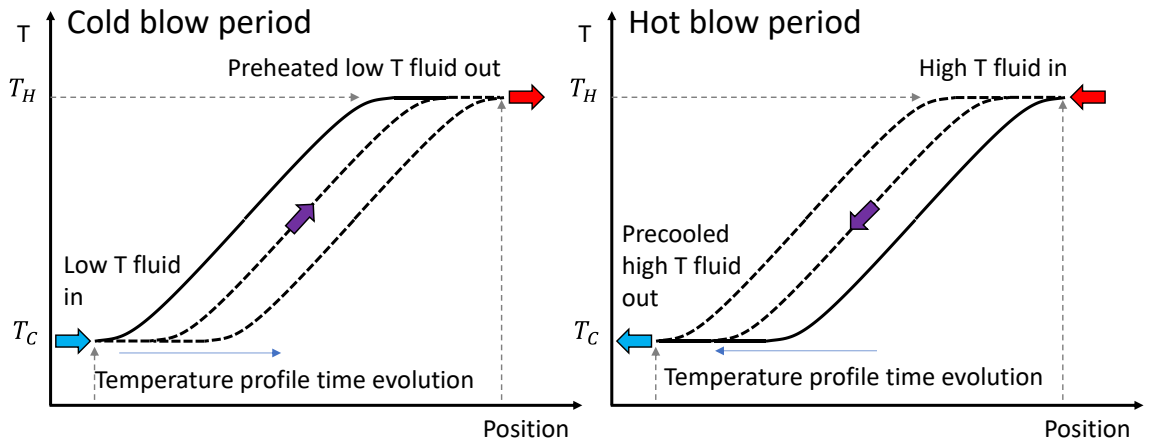

Figure 11: Schematic of regenerator temperature profile during operation.

The temperature gradient is highly dependent on operating conditions, such as cycle time and mass flow rate; geometrical characteristics, such as the dimensions and shape of flow passages, total heat transfer area, between other factors. If the operation and geometry of the regenerator are determined correctly, the regenerator can be as effective as a recuperator (Shah and Sekulic, 2003).

This approach has been applied successfully in magnetocaloric cooling systems, and taken a step further by making the regenerator itself out the magnetocaloric material. When the regenerator is only used to store heat, is referred to as a "passive" regenerator. When besides storing heat, the regenerator goes through the phase transformation with the application of a stress, magnetic or electric field, is referred to as an "active" regenerator.

1.2.5 Concepts about thermal design theory for ideal passive regenerators

Two methods have been used for regenerator thermal performance analysis: ε-NTU_0 and Λ-Π methods (Shah and Sekulic, 2003). These methods were developed for ideal passive regenerators with a very specific set of assumptions that make the heat transfer analysis easier. One of these assumptions is that "*there is no phase change occurring in the regenerator*" which automatically disqualifies active regenerators to be covered by this theory, so a different approach is presented in the next chapter. However, the analysis of design theory for passive regenerators can still offer important insight. It is difficult to imagine that a regenerative heat exchanger made out of a caloric material with the intent of operating as a high performing active regenerator could manage to do that while performing poorly as a passive regenerator. Figure 12 shows the effectiveness of an ideal passive regenerator as a function of two non-dimensional parameters: NTU_0 and C_r.

$$NTU_0 = \frac{hA}{2\dot{m}_f c_{p,f}} \qquad \text{Equation 10}$$

$$C_r^* = \frac{\frac{m_{AER} c_{p,s}}{t_{HT}}}{\dot{m}_f c_{p,f}} = \frac{m_{AER} c_{p,s}}{m_f c_{p,f}} \qquad \text{Equation 11}$$

According to Figure 12, the effectiveness of a regenerator increases as NTU_0 increases, and as C_r* increases. Equation 10 says that large heat transfer coefficient and large heat transfer area will make the value of NTU_0 grow, while larger mass flow rates and using a working fluid with a large heat capacity will make the value of NTU_0 decrease (Equation 10 assumes that the heat transfer coefficient is the same during heating and cooling period).

Equation 11 says that the larger the thermal mass of the regenerator wall in comparison to the thermal mass of the fluid and goes through it during the cycle, the higher the C_r^* will be. For a fixed regenerator geometry, this means that the lower the amount of working fluid that runs through the regenerator during the cycle, the larger C_r^* will be. Finally, the calculation of the effectiveness can be done with Equation 12 (Shah and Sekulic, 2003).

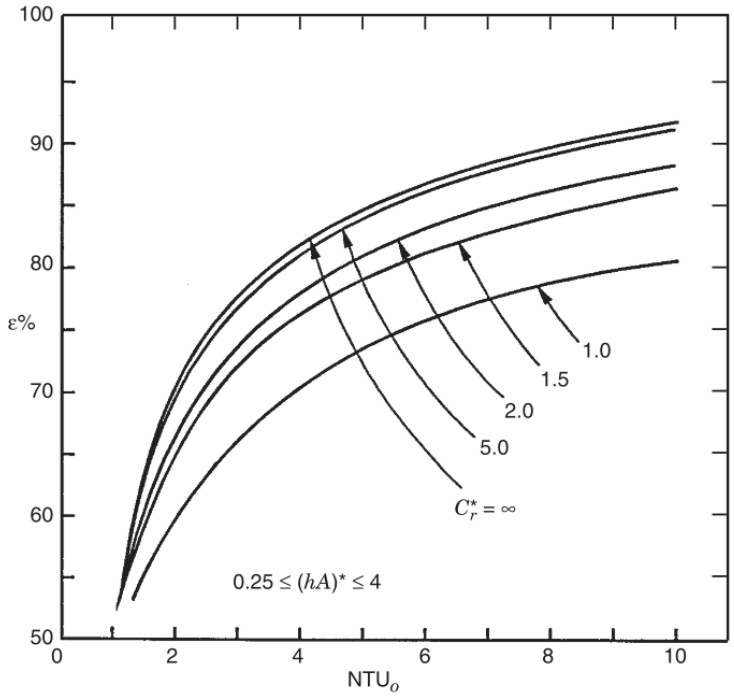

Figure 12: Regenerator effectiveness for the ε-NTU_0 method (Shah and Sekulic, 2003)

$$\varepsilon = \overbrace{\frac{NTU_0}{1 + NTU_0}}^{\varepsilon_{cf}} \left[1 - \frac{1}{9(C_r^*)^{1.93}}\right] \qquad \text{Equation 12}$$

In Equation 12 the quotient that is marked with a bracket and the symbol ε_{cf} is the definition of the effectiveness of a counterflow recuperator and it shows that as NTU_0 approaches

infinity, the effectiveness of the counterflow recuperator will approach to 1. The effectiveness of a counterflow heat regenerator can only approach the effectiveness of the counterflow recuperator and will reach it only when C_r^* equals infinity (in practice, $C_r^*>10$ is close enough to infinity).

1.2.6 Elastocaloric cooling prototypes in the context of solid-state cooling

Near-room temperature solid-state cooling was first achieved by Brown in 1976 using a magnetocaloric material Gd, in a reciprocating system using passive heat regeneration as a very effective heat recovery strategy to develop large temperature lift. His prototype did not supply any cooling, but reached 47 K temperature lift, which remains one of the highest values reported (Brown, 1976). Since then, several groups around the world worked to develop prototype systems that not only develop temperature lift but also supply cooling capacity. Two review articles provide a good summary of the main publications reporting the performance of magnetocaloric cooling prototypes (Yu et al., 2010) (Greco et al., 2019). These review papers provide two significative figures to for each prototype, a maximum cooling capacity and a maximum temperature lift. Even though these two numbers are meaningful achievements of a prototype system, they are not enough to describe the full capabilities. To make a general performance assessment of the actual capabilities of magnetocaloric systems all the articles referred to in the review papers were surveyed and the detailed data used to make the following figures can be found in Appendix A.

Figure 13 shows all performance data pairs of temperature lift and cooling capacity plotted together. This shows a general image of what magnetocaloric cooling systems have been able to produce so far and helps to visualize the Pareto front of the technology today.

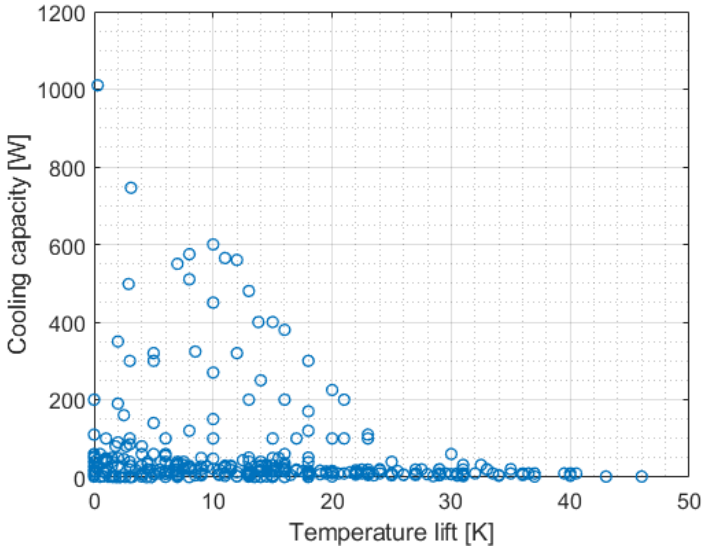

Figure 13: Surveyed data of cooling capacity and temperature lift of magnetocaloric cooling prototypes

It is important to further process this data. To do this three metrics were chosen: temperature lift at zero cooling capacity, cooling capacity and the area below the cooling capacity-temperature lift curve.

Figure 14 shows the temperature lift on the x-axis and the cumulative percentage of published data for each value of temperature lift. The figure can be useful to answer two questions: one, for a certain temperature lift, what is the percentage of published datapoints below or above that value, and two; what temperature lift does a system need to provide to be above a certain percentage of the published data. For magnetocaloric system 25 K seems

to be an inflexion point in the trend, only 10% of the published data points surveyed for this work have surpassed that.

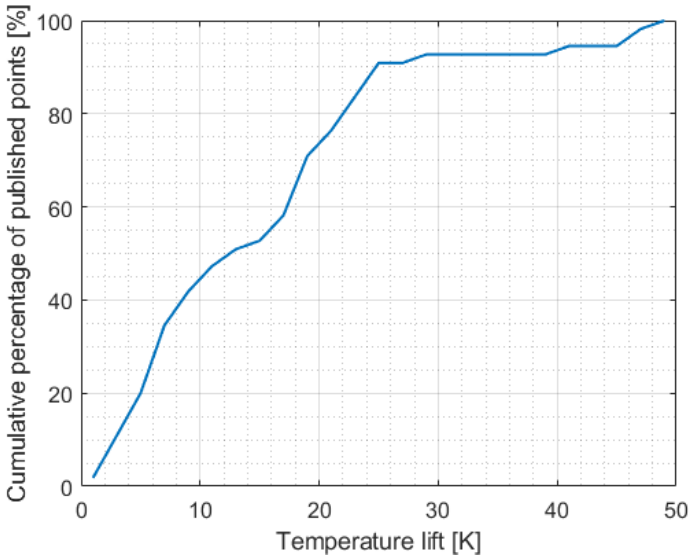

Figure 14: Temperature lift performance of magnetocaloric cooling devices

Figure 15 shows a similar approach applied to cooling capacity.

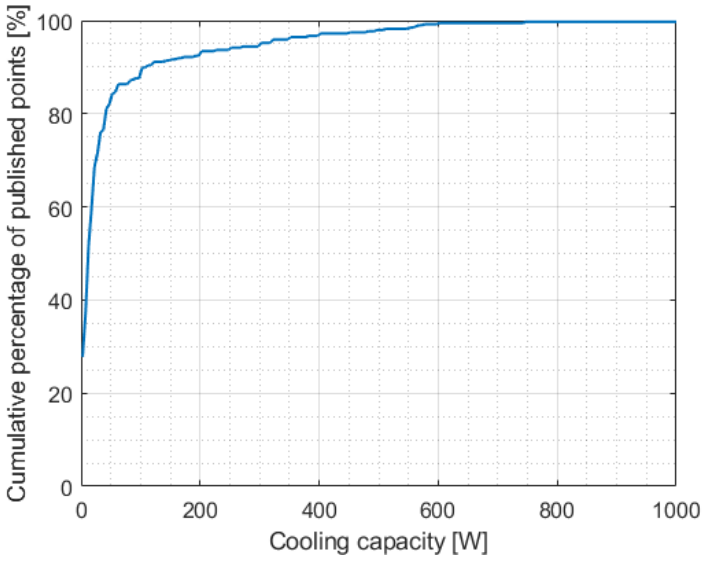

Figure 15: Cooling capacity performance of magnetocaloric cooling devices

In this case the inflexion point appears to be at approximately 100 W. Only 10% of the published data points report values of cooling capacity being above 100 W, without considering what was the system's temperature lift.

Figure 16 shows once again the same approach, but the metric this time is the area under the cooling capacity (CC) -temperature lift (ΔT) curve. The objective is to "reward" operating conditions that are able to supply useful performance: a large temperature lift with small cooling capacity, or a large cooling capacity with small temperature lift are not preferred from the practical point of view of supplying cooling to a moderate cooling capacity at a moderate temperature lift. The inflexion point appears to be around 800 W·K, which again represent the level beyond which only 10% of the data points reached.

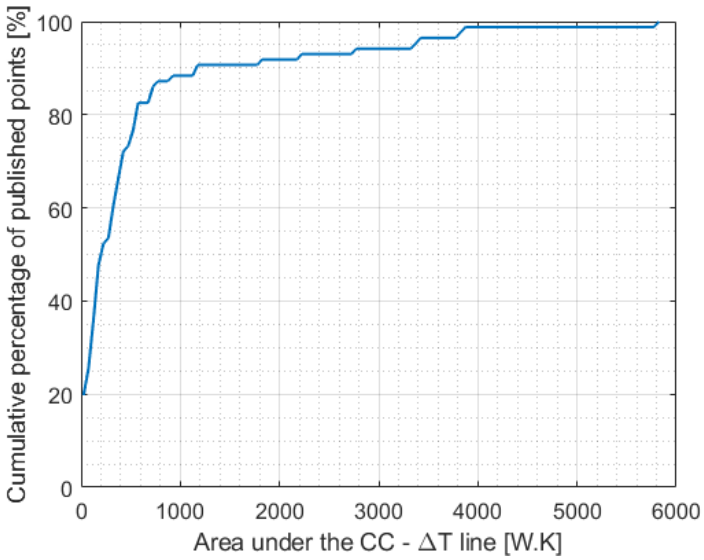

Figure 16: Area under the cooling curve for magnetocaloric cooling devices

To develop a better idea of what this number means one can imagine a cooling system, as Figure 17 shows, that under a certain set of operating conditions could provide a maximum temperature lift of 16 K at zero cooling capacity and 100 W at zero temperature lift. That would be equivalent to 800 W·K.

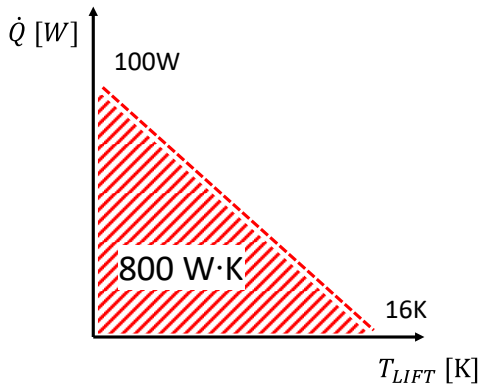

Figure 17: Example of system of to match the area-under-the-curve threshold

Elastocaloric cooling, with a much shorter track record than magnetocaloric cooling, started at the University of Maryland with the demonstration of high efficiency cooling of Ni-Ti wires (Cui et al., 2012). Since then, efforts have geared towards building a high-performing elastocaloric cooling system by developing several prototypes.

The first prototype consisted in a "bird-cage" structure made out of Ni-Ti wires. Figure 18 shows a schematic of the system. In this system, the top and bottom rings are concentric but not parallel causing the distance between the rings to be minimum at one location and maximum at the radially opposite location. As the motor rotates the "bird-cage" around, the wires are pulled and released, inducing the forward transformation by the application of a tensile stress and reversing it when the stress is released. Two air streams exchange

heat with the wires as they are loaded and unloaded. This concept was not able to produce measurable cooling capacity but did produce a temperature lift of 1.7 K.

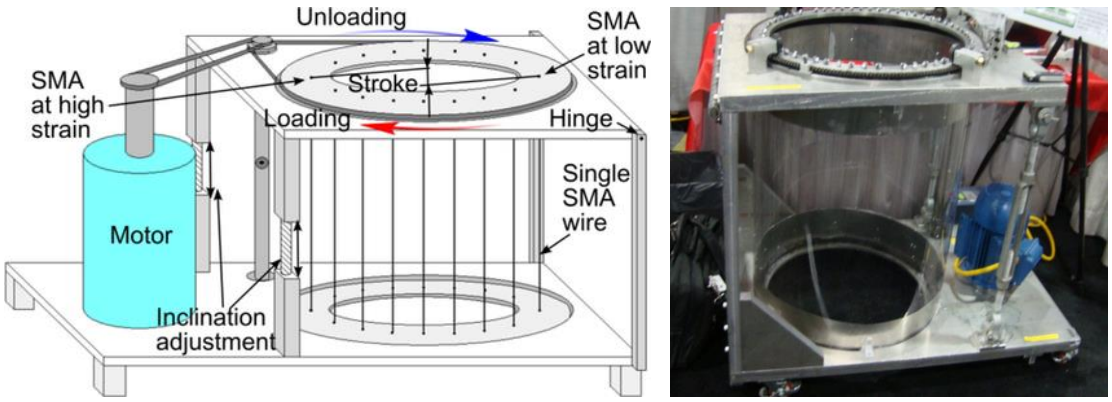

Figure 18: "Bird-cage" prototype schematic and photograph

The second prototype transitioned from the "bird-cage" structure made with Ni-Ti wires to two heat exchangers made out with Ni-Ti tubes, like the one Figure 19 shows.

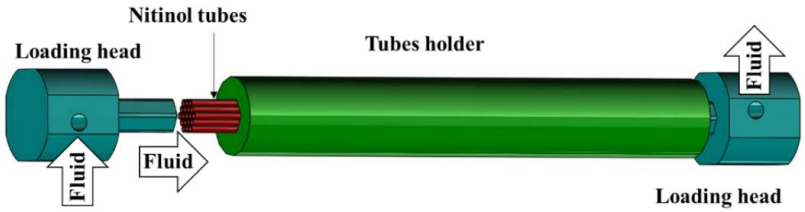

Figure 19: Schematic of Ni-Ti heat exchanger (Qian, 2015)

Instead of inducing the transformation by tensile stress, it was done by compression, and instead of exchanging heat directly with air, water was used as an intermediary heat transfer fluid. After the loading step, water flows from a hot-water loop through the Ni-Ti tubes absorbing the transformation heat being released and rejecting downstream at the heat sink.

After the unloading step, water flows from a cold-water loop through the Ni-Ti tubes rejecting heat and absorbing a certain amount downstream at the heat reservoir (supplying cooling). In addition to these changes two important features were added: work and heat recovery.

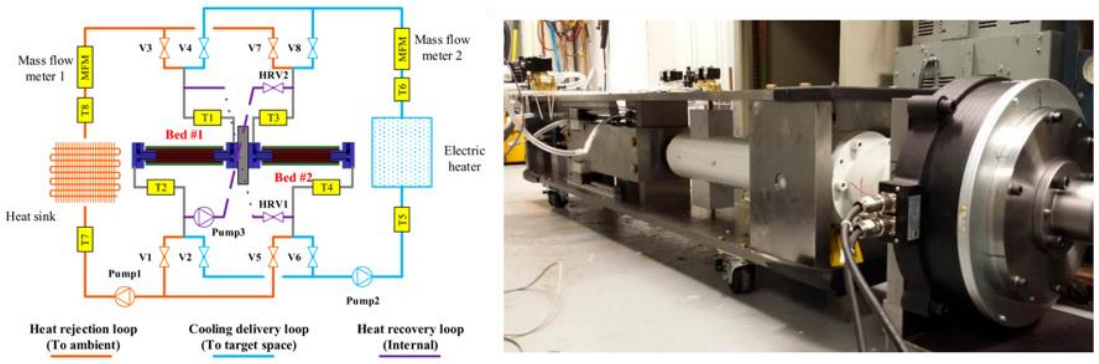

Figure 20: Two-tube holders reciprocating prototype schematic and photograph (Qian, 2015)

Work recovery was achieved by setting up the two Ni-Ti heat exchangers geometrically opposed to each other, constrained by a frame with a moving crossbar in between. When the crossbar is in the middle, both holders are compressed to half of the maximum operating strain. During operation they are compressed in reciprocation, when one is fully compressed the other is fully decompressed such that the unloading work of one was used to assist loading of the other. Heat recovery was achieved through a heat recovery water loop. After rejecting heat to the water in the hot water loop, the Ni-Ti tubes have a final temperature equal to that of the water in the hot water loop. Similarly, after absorbing heat from the water in the cold-water loop, the Ni-Ti tubes have a final temperature equal to that of the water in the cold-water loop. The heat recovery loop allows the first heat exchanger to be precooled before unloading, and the second to be preheated before loading

by exchanging sensible heat between each other. This concept, called “time-scale thermo-wave”, was based on a counterflow heat exchanger and enabled the expansion of the temperature lift of the system (Qian et al., 2015). With this concept, Qian measured a maximum cooling capacity of 65 W and a maximum temperature lift of 4.2 K (Qian, 2015).

The third prototype (Qian et al., 2016), required a complete redesign of the loading frame structure and the utilization of hydraulic actuators as the loading mechanism.

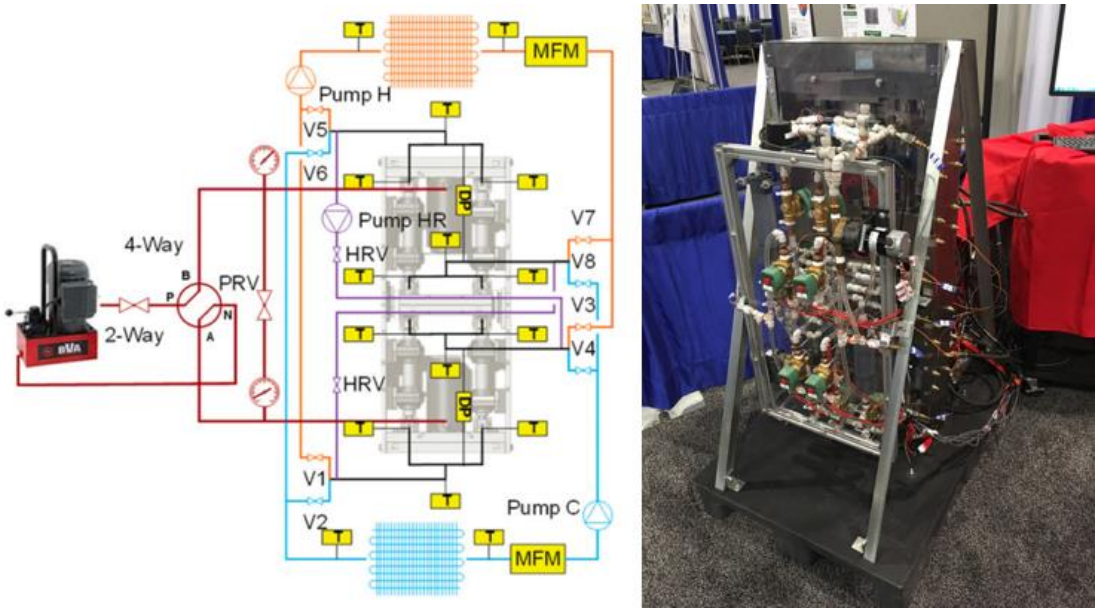

Figure 21: Four-tube holders reciprocating prototype schematic (Qian et al., 2016) and photograph

Conceptually the principle of operation is the same as the second prototype, with the same work and heat recovery mechanisms but in this configuration, there are nineteen Ni-Ti tubes inside each heat exchanger, and also four heat exchangers instead of two. The assembly and testing of this prototype were done as the first task of this dissertation.

The testing procedure of this system consisted first on determining the largest temperature lift that could be achieved with no heat rejected at the sink and no heat absorbed at the reservoir. From now on this will be referred to as the ***"temperature lift"***. Under these conditions, the temperatures of the hot side and cold side continue to increase as the system operates, but the temperature lift will stabilize after an initial transient. Figure 22 shows the time evolution of the hot side and cold side temperatures with an applied strain of 3.6% and 4.5%.

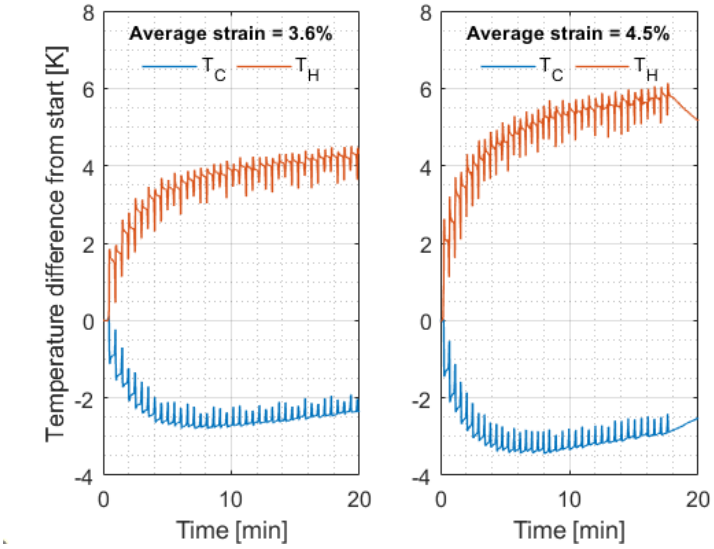

Figure 22: Time evolution of T_H and T_C for two average strain levels of 3.6% and 4.5%

Figure 23 shows how the temperature lift stabilizes after approximately 10 minutes even if the actual temperature continues to increase. For the 3.6% average strain test, the system temperature lift is 6.7 K while for the 4.5% average strain it is 8 K. These two values represent an improvement with respect to the maximum measured in the previous prototype of 4.2 K at 4% average strain.

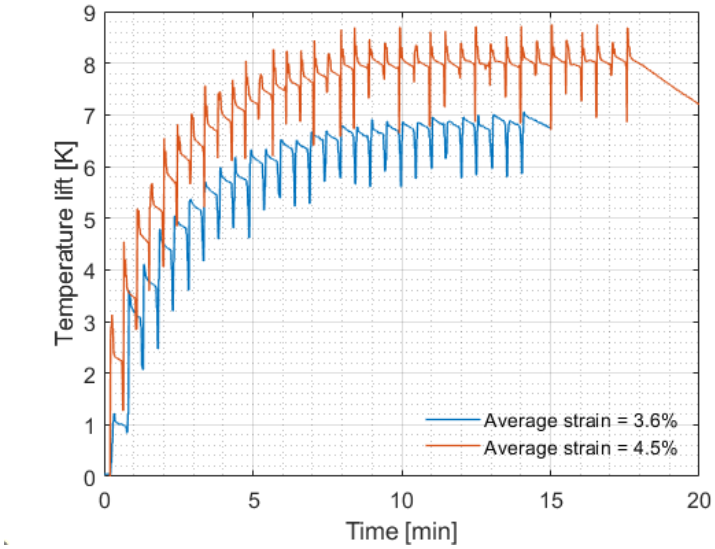

Figure 23: Temperature lift for an average strain of 3.6% and 4.5%

Figure 24 shows the detailed time evolution of the temperature measurement at the inlet and outlet of two opposing Ni-Ti (HEX-A and HEX-C) heat exchangers and an identifier of the cycle step according to Table 1.

Table 1: Identification of the steps of the cycle

Step	Function	Time [s]
1	Loading HEX-A and unloading HEX-C	6
2	Heat rejection HEX-A and Heat absorption HEX-C	8
3	Heat recovery	15
4	Hydraulic pressure balance	1
5	Unloading HEX-A and loading HEX-C	6
6	Heat absorption HEX-A and heat rejection HEX-C	8
7	Heat recovery	15
8	Hydraulic pressure balance	1
Total cycle time = 60 s		

The precooling of HEX-A and preheating of HEX-C can be seen by following the water temperature evolution at the outlet during cycle step 3 in Figure 24.

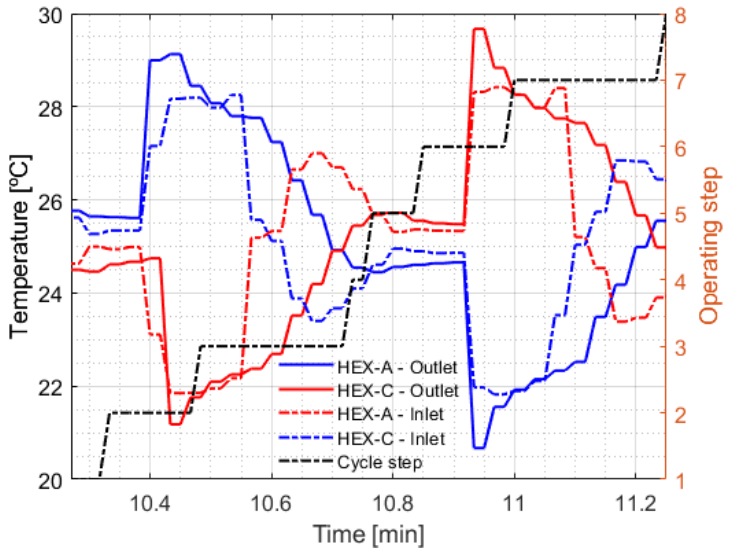

Figure 24: Time evolution of inlet and outlet temperature of two opposing Ni-Ti heat exchangers

At the beginning of cycle step 3, the temperature at the outlet of HEX-A is higher than the one at the outlet of HEX-C. As the water from the heat recovery water loop flows between HEX-A and HEX-C, the fluid temperature at the outlet of HEX-A decreases and at the outlet of HEX-C increases. Towards the end step 3, the outlet fluid temperatures cross each other and now the temperature at the outlet of HEX-A is lower than the one at the outlet of HEX-C.

Figure 25 shows the efficiency of the heat recovery process. Equation 13 and Equation 14 show the expressions to calculate the precooling and preheating efficiencies respectively. The superscripts “ini” and “end” refer to the initial and last instants in the heat recovery

process. The precooling efficiency is 1 if $T_{HEX\text{-}A}$ at the end of the heat recovery step is equal to $T_{HEX\text{-}C}$ at the beginning of the heat recovery step. Analogously, the preheating efficiency is 1 if $T_{HEX\text{-}C}$ at the end of the heat recovery process is equal to $T_{HEX\text{-}A}$ at the beginning of the heat recovery step. The temperatures are measured at the outlet of each HEX.

$$e_{HR,pre-cooling} = \frac{T_{HEX-A}^{ini} - T_{HEX-C}^{end}}{T_{HEX-A}^{ini} - T_{HEX-C}^{ini}} \qquad \text{Equation 13}$$

$$e_{HR,pre-heating} = \frac{T_{HEX-A}^{end} - T_{HEX-C}^{ini}}{T_{HEX-A}^{ini} - T_{HEX-C}^{ini}} \qquad \text{Equation 14}$$

Details of this heat recovery strategy and why, just like in a counter-flow heat exchanger, an efficiency of 1 is theoretically possible can be found elsewhere (Qian et al., 2015). An efficiency of 0.5 is what one can expect from parallel-flow heat exchanger. In practice, the efficiency is somewhere in between, close to 60%.

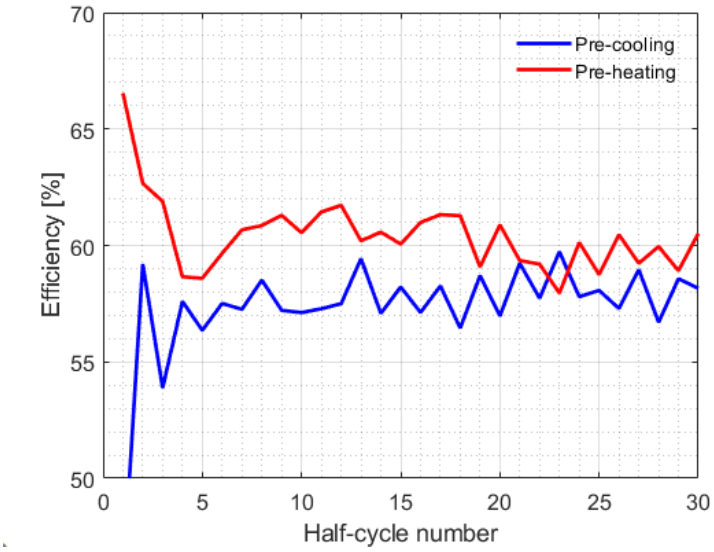

Figure 25: Heat recovery efficiency for each half-cycle

Figure 26 shows the load as a function of the displacement experienced by the Ni-Ti heat exchangers. Heat exchangers A and B are opposed to C and D. When A and B are completely loaded, C and D are completely unloaded and vice versa. Specifically, in this case, at a strain of 3.5%, the loading work during one cycle is equal to 492 J and the unloading work is 311 J which is recovered by reducing the amount of energy that the hydraulic actuator needs to supply.

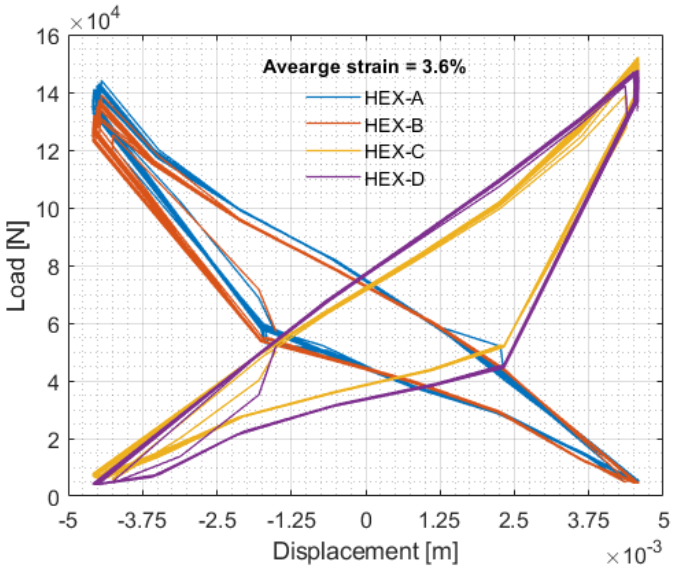

Figure 26: Mechanical reponse of all four tube holders during a test with an average strain of 3.6%

The cooling capacity was tested in a semi-open loop configuration, with the system operating as a water chiller. Figure 27 shows a schematic of the experimental set up and. The hot-water loop was made an open-loop by removing the compact heat exchanger acting as a heat sink in the second-generation system. Once the compact heat exchanger is removed, the hot-water loop is left with two open ports: and outlet (which before would feed the inlet of the heat exchanger) and an inlet (which before was fed by the outlet of the

heat exchanger). The hot water coming out of the Ni-Ti heat exchangers is now rejected out of the system, and the inlet is fed from a water reservoir at room temperature. This was a more effective way to achieve the effect of an infinite heat sink. The cold-water loop remained closed, but the compact heat exchanger was replaced with an electric heater connected to a variable voltage source was used to precisely simulate various cooling loads.

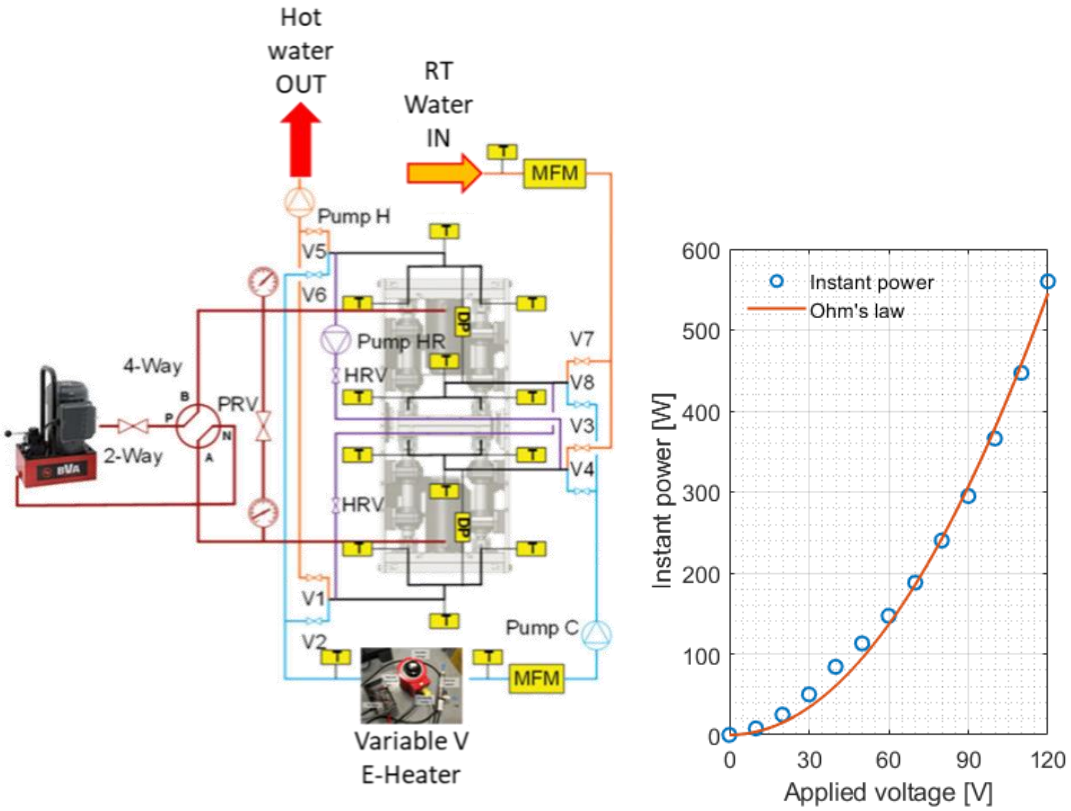

Figure 27: Experimental setup for cooling capacity testing

Figure 28 shows the difference between the temperature of the water at the outlet of the electric heater and the temperature of the inlet water (fed from the reservoir at constant temperature) as a function of time, for four different heater loads. This temperature difference is a negative number because the system is supplying cooling, by convention its

absolute value is the ***"useful temperature lift"***, and it is a function of the heater load, referred to as the ***"cooling capacity"***. As the heater load increases, the useful temperature lift decreases. The heater load is averaged over the duration of the cycle. Since the electric heater delivers heat only during the heat absorption step, the instant cooling capacity is higher than the average.

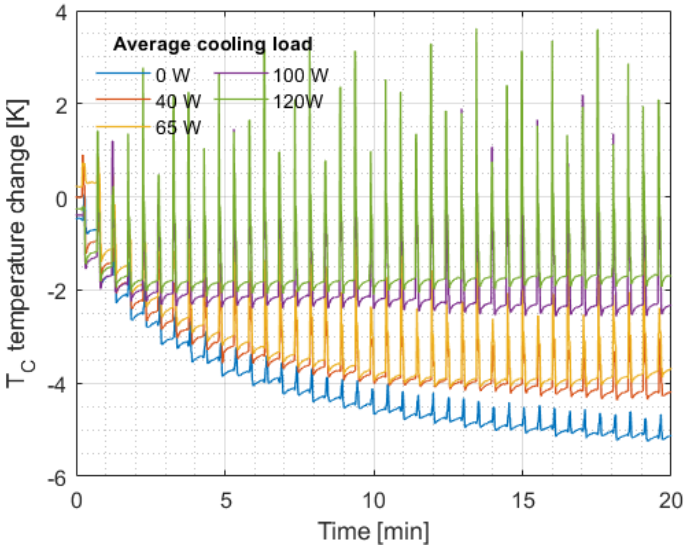

Figure 28: Time evolution of useful temperature lift for five cooling loads

Figure 29 shows the cooling performance of the 2-reciprocating beds system as measured by Qian (Qian, 2015) and the 4-reciprocating beds system as measured in this work. By increasing the number of Ni-Ti tubes and the strain it was possible to increase both the temperature lift and the cooling capacity. Figure 29 is the starting point for this work. It is important to go back and put these performance measurements in perspective with respect to magnetocaloric cooling systems.

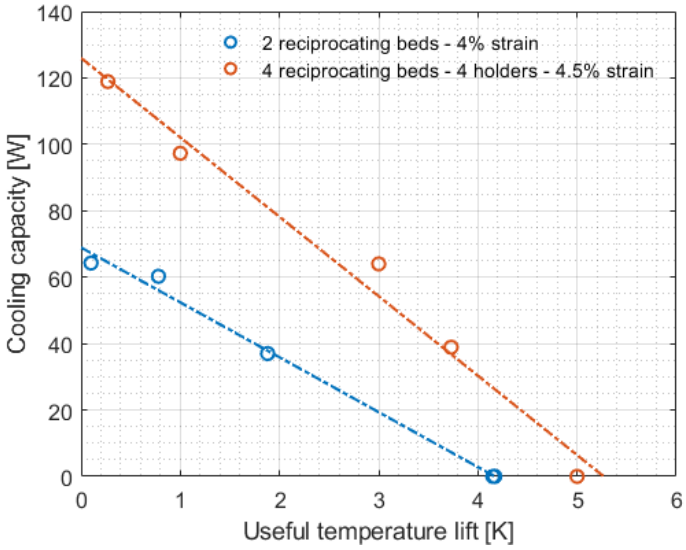

Figure 29: Cooling capacity as a function of temperature lift

Figure 30 shows where this system configuration stands in terms of maximum temperature lift. The second-generation system produced a maximum temperature lift of 4.2K, which is superior to only 20% of the magnetocaloric cooling systems. The third-generation system expanded that maximum temperature lift to 8K, being able to surpass an additional 20%, to reach almost 40%. It is clear that there is still a large climb ahead and this is the main priority: expand temperature lift. Increasing cooling capacity is easier to do by increasing the amount of Ni-Ti material, but to expand temperature lift it is required to have a very effective heat recovery strategy in place.

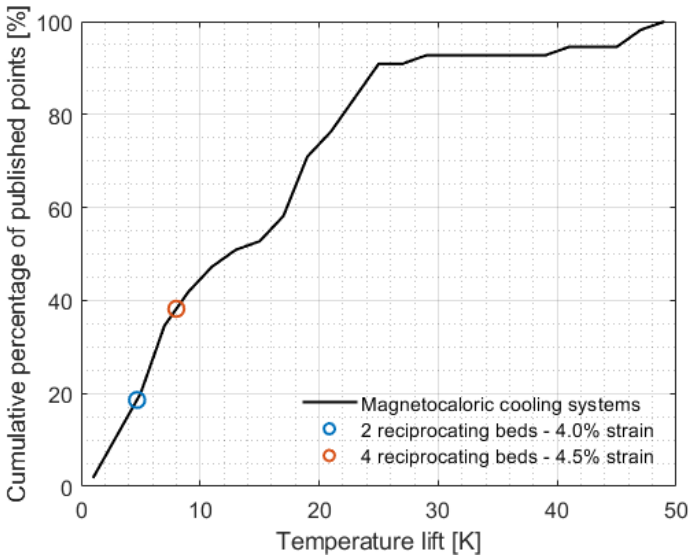

Figure 30: University of Maryland elastocaloric cooling devices compared against surveyed magnetocaloric cooling systems temperature lift

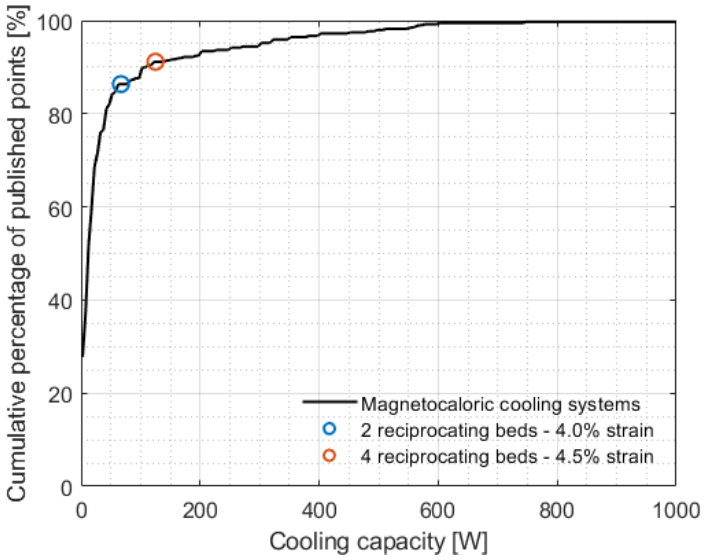

Figure 31: University of Maryland elastocaloric cooling devices compared against surveyed magnetocaloric cooly systems cooling capacity

Figure 31 shows the standings from the point of view of cooling capacity. Most of the cooling devices published in literature are small prototypes and they do not supply a large

cooling capacity. The maximum cooling capacity supplied by the second- and third-generation systems put them above 90% of the magnetocaloric cooling published data.

To have a complete picture, Figure 32 shows where the second- and third-generation systems stand with respect to the area under the cooling capacity vs. temperature lift curve. The second-generation system was above approximately 38% of all magnetocaloric cooling systems and the third-generation system was above approximately 58%. The improvement in standing was mostly due to the increase in cooling capacity, but despite this, both concepts are still below the inflexion point.

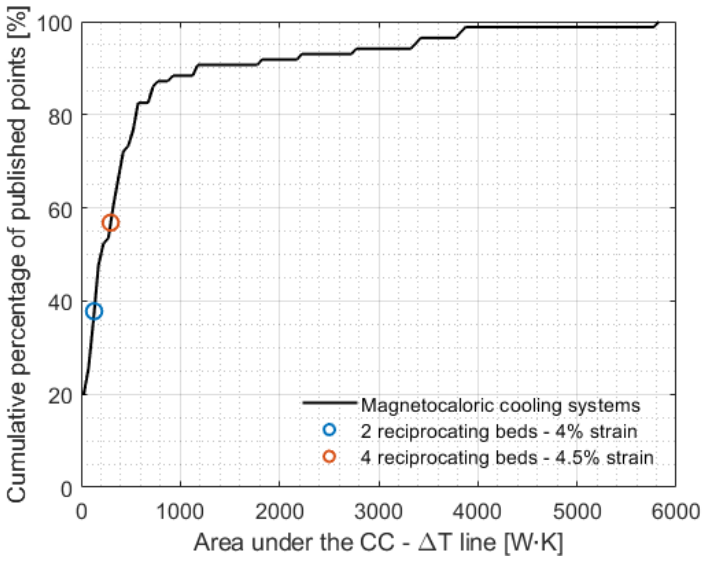

Figure 32: University of Maryland elastocaloric cooling devices compared against surveyed magnetocaloric cooly systems area under the cooling performance curve

The active regeneration cycle has proven to be successful in magnetocaloric systems and now is being implemented in elastocaloric systems. The first active elastocaloric regenerator heat pump was built with a stack of small and thin plates of Ni-Ti and a uniaxial

tensile stress was applied to induce the transformation. The active regeneration cycle using water as a heat transfer fluid exhibited a temperature span of 15.3 K (Tušek et al., 2016). Further development showed a maximum temperature lift of 17.6 K and 19.9 K (Kurt Engelbrecht et al., 2017). The maximum cooling capacity was not reported, however, considering the mass of Ni-Ti was 5.8 g and 12.3 g in two different configurations, it must have been in the order of the single digit W or lower.

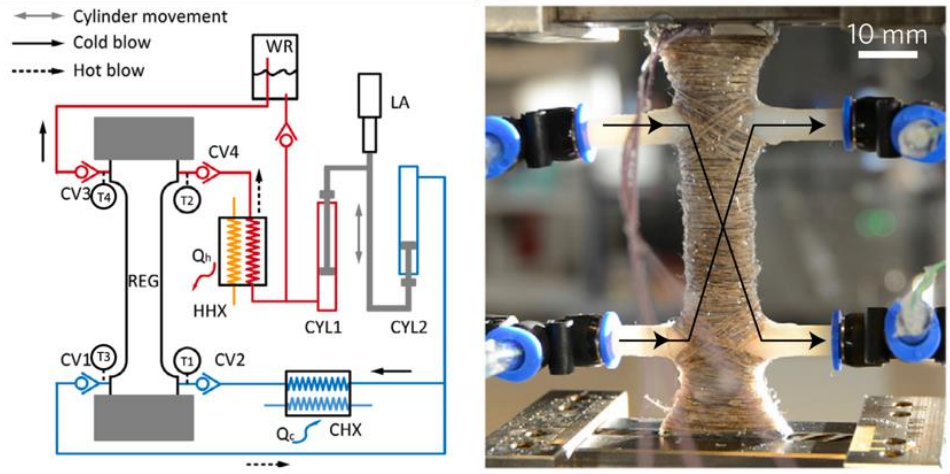

Figure 33: A miniature active elastocaloric regenerator (Kurt Engelbrecht et al., 2017; Tušek et al., 2016)

Another miniature-scale system that uses Ni-Ti thin film and foils was published in literature and with a thorough analysis of design alternatives (Ossmer et al., 2016). This concept does not use a heat transfer fluid to exchange heat with the elastocaloric material: the heat sink and reservoir are solid copper pieces and the elastocaloric thin-foil exchanges heat with them by physical solid-solid contact. Figure 34 shows one of those configurations in which the mechanical loading is realized through deflection of the bridge center in out-of-plane direction. This configuration allows for work recovery (Bruederlin et al., 2017).

The maximum cooling capacity reported was 0.051 W, and the maximum temperature lift was 5 K.

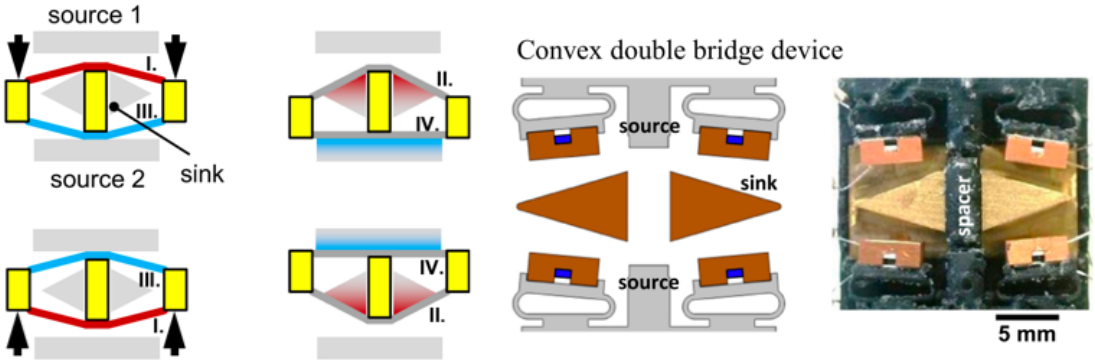

Figure 34: Microcooling device (Ossmer et al., 2016)

The results of a design study of a system concept utilizing wires between two rotating discs has been published, but no system experimental results yet (Kirsch et al., 2018).

Chapter 2: Active Elastocaloric Regenerator

2.1 Active elastocaloric regenerator system and testing facility

Figure 35 shows the main components of the system: the frame, the hydraulic actuator, the heat transfer loop, heat sink and heat reservoir, the regenerator and the instrumentation with data acquisition/control/electric box. The frame and the hydraulic actuators are part of the previous system configuration. The DAQ-control-electric box was completely rebuilt and upgraded with additional electric instrumentation, all of which is described in this section.

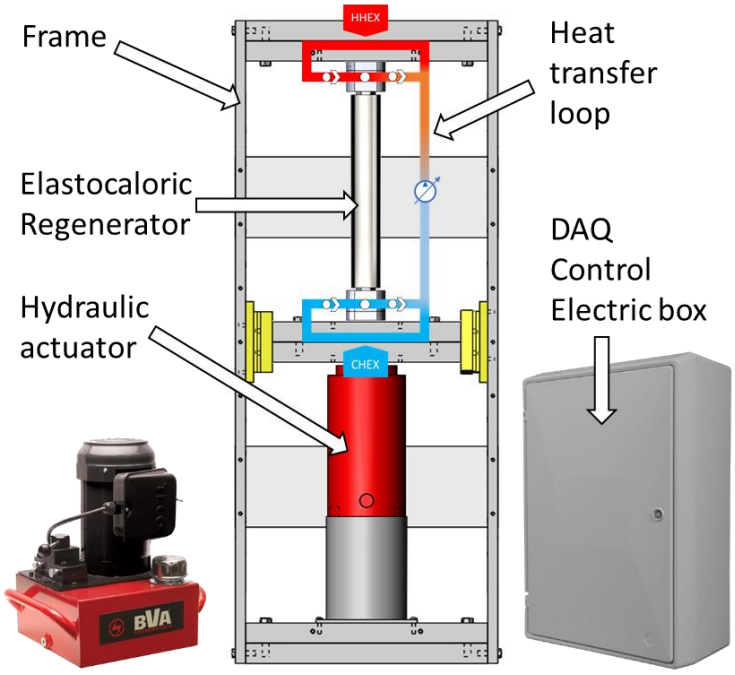

Figure 35: Main components of the one stage active elastocaloric regenerator system

2.1.1 Frame

The frame is a robust low-carbon steel structure composed of two main load-bearing vertical beams (one on the left and the other on the right), and four horizontal beams (two on top, and two on the bottom) that transfer the load applied by the actuators through 64 dowel pins. Based on the cross-section of these vertical beams (0.15m x 0.04m) the estimated compliance is 4.4 e^{-10} m/N. For a load of 200,000 N (which is around the maximum Ni-Ti has been subjected to during this work, it is expected a frame compliance of 0.1 mm, which is within 1.5% of the total displacement that Ni-Ti would experience with that load (9 mm).

2.1.2 Hydraulic actuators

In the system configuration shown in Figure 35 only one actuator is used, but the hydraulic system used in this work has two BVA H7506 single-acting actuators with a maximum travel of 12.7 mm, each of which can apply a maximum force of 735,500 N (168,000 lbf). For system configurations with two or more regenerators operating in reciprocating mode both actuators are used. The two hydraulic cylinders are connected with the hydraulic pump through valves, the schematics of which are shown Figure 36. The valve arrangement of the left operates as a 4-way valve. When the solenoid valve A is energized and opens up it allows pressurized oil to enter cylinder A while oil from cylinder B goes back to tank. When solenoid valve B is energized and opens up it allows pressurized oil to enter the cylinder B while oil from cylinder A goes back to tank. The valve shown on the right-hand side of Figure 36 has the function of balancing the pressure between cylinders. This valve is opened to utilize the elastic energy stored in the loaded regenerator to push the oil out of

the cylinder and into the unloaded cylinder, to preload it and reduce the work the pump needs to do to complete the loading process. The valve is wired in the “normally closed” option.

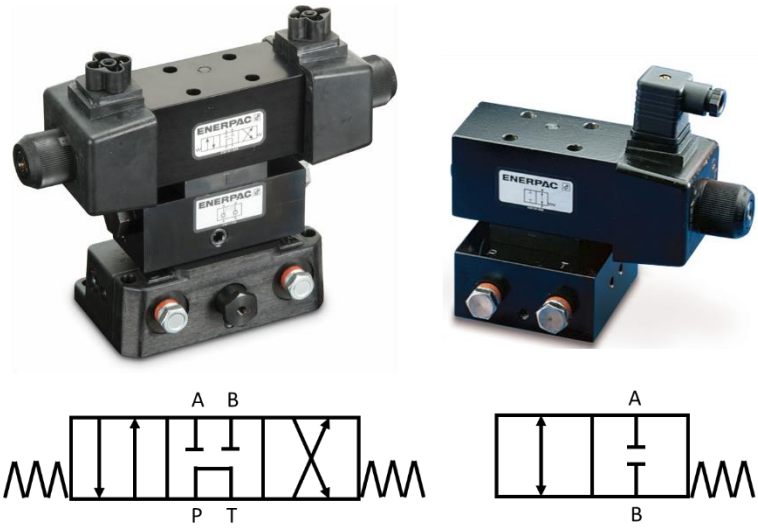

Figure 36: Hydraulic valves used in the system

2.1.3 Heat transfer loop, heat sink and heat reservoir

The main function of the heat transfer loop is to direct the movement of heat transfer fluid from and into the regenerator during the system operation. There are three specific heat transfer loop configurations in this study, and for clarity they are described in independently in each appropriate section.

The function of the heat sink is achieved by using a semi open-loop approach as explained in Chapter 1. The heat reservoir is a necessary element to simulate different cooling loads. For this task a low-flow air process and liquid circulation heaters from Omega model

AHPF-061 was used. The heater consists of a heating element which is connected to a variable voltage source that can be adjusted to supplies a heat input. After upgrading the electric box, he electrical power dissipated by the heater is measured with a power transducer.

2.1.4 Regenerator

Figure 37 shows the three main components of the active elastocaloric regenerator: the elastocaloric material, the tube holder and the loading heads.

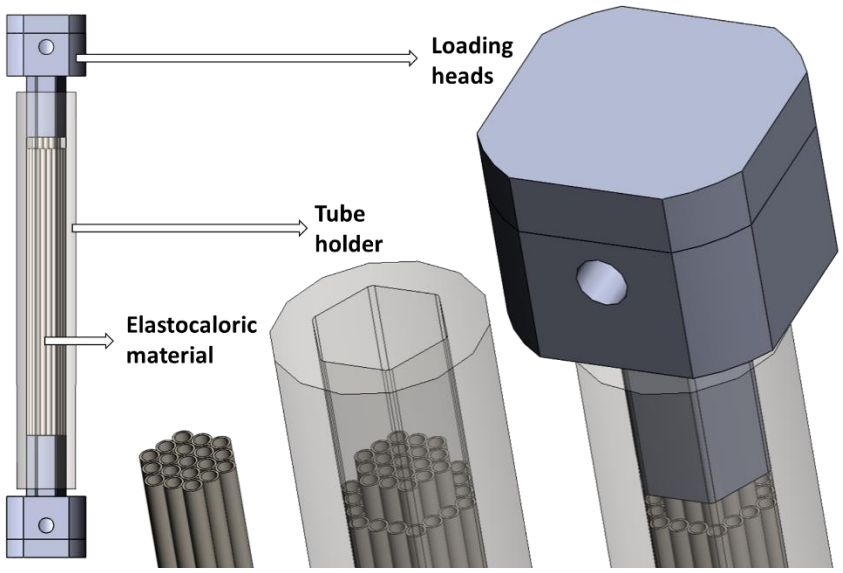

Figure 37: Schematic of main components of elastocaloric regenerator

The elastocaloric material is a superelastic Ni-Ti alloy procured from Confluent medical as tubes of 4.718 mm OD, 3.759 mm ID. The tubes were originally cut in segments of 254 mm length. In the current configuration a single regenerator has 19 Ni-Ti tubes arranged in a hexagonal pattern and to induce the martensitic transformation the tubes are

compressed using the hydraulic actuator and the frame. An important step in preparing the tubes for use is called training. Training consists on applying compression cycles until the materials microstructure sets in. During this process, that can take in the order of hundreds of cycles, the materials decreases its length. This needs to be taken into consideration because the frame is of fixed length, so it the tubes are shorter, they will need to be shimmed to fit the frame properly. The decrease in length was approximately 1% of the total length after training at 4% strain.

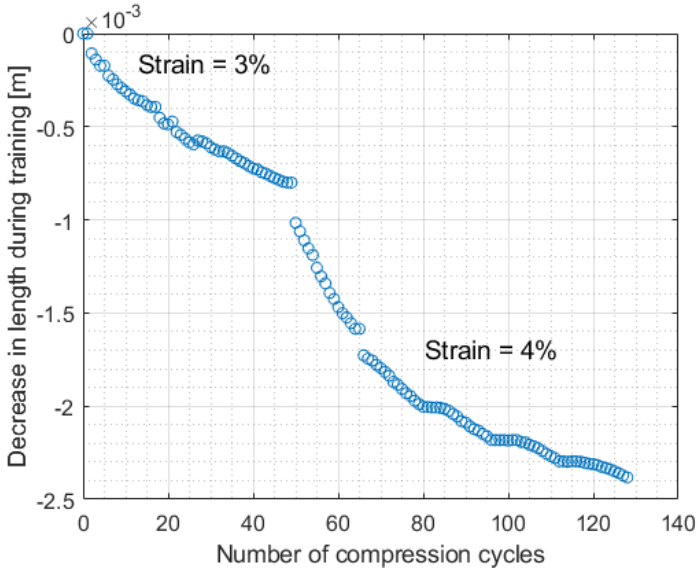

Figure 38: Decrease in tubes length during training

The main function of the tube holder is to laterally constrain the tubes to prevent buckling. It was designed to contain 37 Ni-Ti tubes, however during a compression test run performed by Qian in 2015 all 37 tubes failed catastrophically at a low strain level of approximately 3%, which was below the normal operating level the tubes were previously subjected to.

Figure 39: Photo of Ni-Ti tubes catastrophic failure (internal report by Qian)

After that, it was found by Qian that it was experimentally more successful to remove the outer layer 18 Ni-Ti tubes and replace it with 18 stainless steel tubes. A possible answer to the question of why using a layer of stainless-steel tubes between the holder and the Ni-Ti tubes helps prevent the catastrophic failure of all tubes simultaneously can be related to the fact that the fracture of Ni-Ti tube is fragile. When a Ni-Ti tube fractures, its ability to supply lateral constraint is compromised and under load, this could trigger failure for all the other tubes at that specific weak spot. Stainless steel tubes will plastically deform instead of going through a fragile fracture, and even after that they will still be able to provide some support.

Because the stainless-steel tubes do not show superelastic behavior, they have to be shorter not to interfere with the Ni-Ti tubes during the compression process. As a result, the outer layer of Ni-Ti tubes remain partially unconstrained during the compression process. Figure 40 shows that this unconstrained distance is approximately 13 mm.

Figure 40: Distance between end of Ni-Ti tubes and support stainless steel tubes (ruler units: mm).

For a 3.5% strain, the total displacement is approximately 9 mm so 4 mm of the tube would be unconstrained at maximum load. As the image show, the Ni-Ti tube shows some barreling at the end and that could be a premature stage before failure as shown in Figure 41. The stainless steel tube has a tapered end, that is to facilitate the introduction of the tube holder by pressing in a manual hydraulic press.

Figure 41 shows a failed tube in the upper left corner of the image in the left before disassembling the heat exchanger for repair. It corresponds to the hot end of the regenerator and it is the end that had the largest distance between the end of the stainless-steel tubes and the Ni-Ti. The image on the middle shows the cold end of the regenerator. It is clearly shown how much the stainless-steel tubes deform, particularly the tubes located in the vertices of the hexagon. The image in the left shows the broken tube after the heat exchanger was disassembled. Failure was fragile. The Ni-Ti tubes in the corners of the internal hexagonal core are more susceptible than the ones in between the corners because

those lose three contact lines with the surrounding tubes, while the ones between the corners only lose two.

Figure 41: Broken Ni-Ti tube and deformation in stainless steel tubes

Another way these tubes experience failure has to do with the development of longitudinal cracks that will allow fluid to leak out of the tube. Figure 42 shows an example of such a failure mode. This does not seem to immediately compromise the structural integrity of the assembly, but the thermal performance decreases due to the loss of fluid.

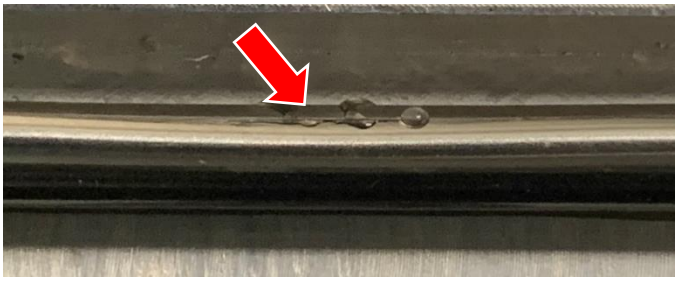

Figure 42: Longitudinal crack that leads to heat transfer fluid leakage

Each regenerator has two loading heads. The main functions of the loading heads are to transfer the load from the actuator to the Ni-Ti tubes to induce the martensitic transformation, and to allow the entry and exit of heat transfer fluid to allow the Ni-Ti tubes

to reject heat after loading, and to absorb heat after unloading. The loading heads have a narrow section that goes inside the tube holder to ensure proper alignment while being in contact with the Ni-Ti tubes, and a wider section that serves as the base. One of the loading heads is in contact with the top of the frame and the other with a moving platform in contact with the actuator. To allow the flow of heat transfer fluid, the narrow section has one circular channel per tube that merge into a cavity inside the wider section and into a single inlet/outlet.

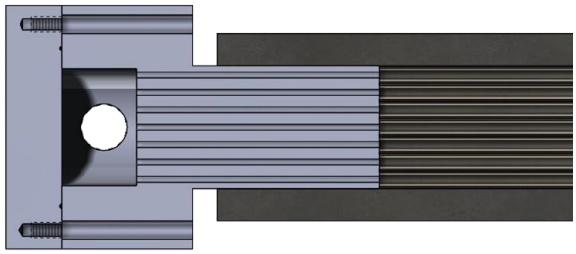

Figure 43: Channels inside loading heads

There are a few additional design elements that improve the heat transfer performance. Figure 44 shows that inside each Ni-Ti tube there is a triangular insert made out of PTFE. This approach was suggested by Qian in his dissertation and a heat transfer analysis of the effect of this can be found there (Qian, 2015). By solving the differential equations of the simplified solid-fluid heat transfer problem of water flowing through a tube, the temperature evolution of the tube and the water coming out of the tube is shown in Figure 44. The tube's starting temperature is 300 K while the water enters at 290 K and exchanges heat with the tube as it flows through. In this process the tube cools down and the water heats up, until eventually the temperature of the tube matches the temperature of the water

and there is no more heat to exchange. If there is no insert, the solid lines show the solid (SMA) and the fluid outlet temperature evolution. The dotted lines represent the results when a triangular insert is used to block the cross section of the tube. The insert blocks about 41.2% of the cross section of the tube and creates three flow channels between the Ni-Ti tube internal surface and the external surface of the insert. The mass flow rate is the same in both situations.

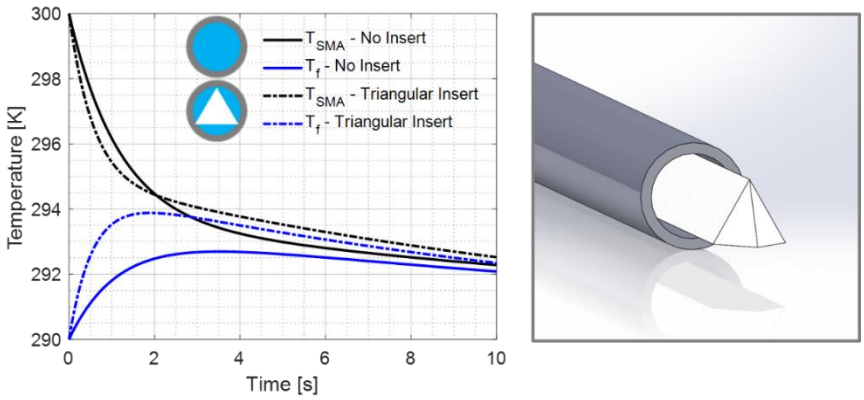

Figure 44: Effect of cross-section blockage in heat transfer performance

One observation is that the peak fluid outlet temperature is higher for the configuration with the insert. Another observation is related to how long it takes for the fluid to converge to the solid temperature. When there is no insert, this time is longer than when there is. The reasons for this improvement from a non-dimensional analysis point of view will be discussed in section 6.1.

A PEEK braided tube is used to line the wall of the circular channels in the narrow section of the loading head to decrease the effective heat transfer from the fluid into the loading

head. The tube is glued to a Delrin® insert. The Delrin® insert with the PEEK tube is introduced in the Ni-Ti tubes. Fluid leaks are prevented with two O-rings that seal the gap between the insert and the Ni-Ti tubes and glued to prevent displacement during compression of the tubes.

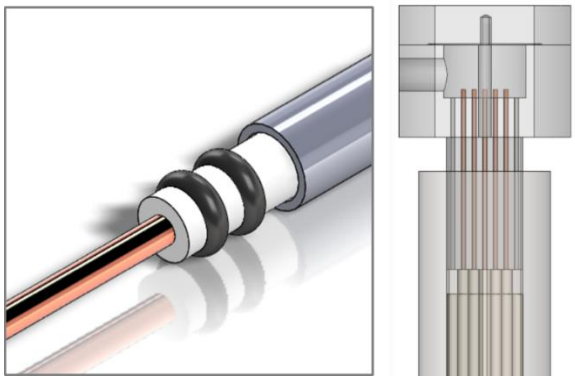

Figure 45: Insert and liner to prevent heat transfer to loading head

An insert is used inside the cavity to decrease the amount of water that can be held inside. The heat transfer fluid that is contained inside the capillaries and the cavity inside the loading head needs to be displaced before the fluid that is inside the regenerator can reach beyond the check-valve and move to tube segment T1 (in heat rejection step) or T4 (in heat absorption step). Ideally this volume should be zero, in practice we can only try to minimize it.

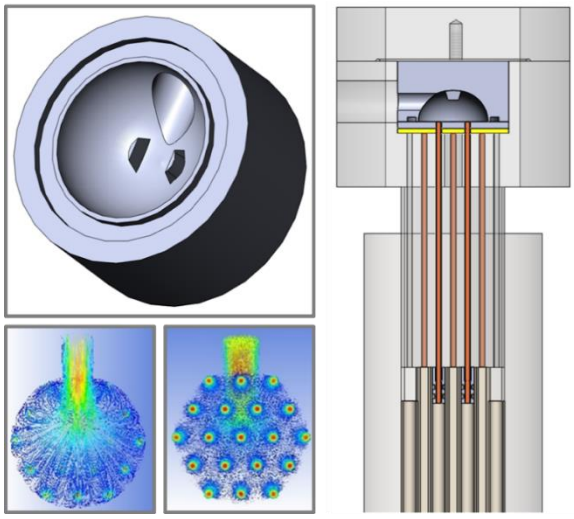

Figure 46: Schematic of loading head insert

2.1.5 Instrumentation and data acquisition/control/electric box

Data acquisition can be done at a sampling rate of 0.1 Hz when necessary but is normally done at 1 Hz through a National Instruments LabView general purpose routine coded at the Center for Environmental Energy Engineering laboratory, modified for the particular characteristics of this application. The routine relies on a selection of hardware modules that can acquire data signals and relay the control signals.

Figure 47: Data acquisition and control modules used in the system

The first module is a NI-9214, a C series temperature input module. Connected to it are 12 T-type thermocouples, however not all of them were used in every experiment.

The second module is a NI-9207, a C series voltage and current input module. Connected to it are two voltage signals coming from two displacement transducers LD620-15 from Omega, a voltage signal coming from the power meter connected to the heat reservoir electric heater and a current signal coming from the power meter connected to the hydraulic pump.

The third module is a NI-9265, a C series current output module and is used to supply the control signal from 0-5V (a 250 Ω resistor is connected between the terminals to achieve this since the current output is 0-20 mA) to set the speed of the heat transfer fluid pump.
The fourth module is a NI-9219, a C series universal analog input module. Connected to it are the 4 voltage input signals from 4 miniature compression load cells LC307-100K from Omega, with a capacity of 445,000 N (100,000 lbf).

The last module is a NI-9476, a C series digital module. It is used to apply the control signals that will open the electrical relays in the electric box and allow the system to operate.

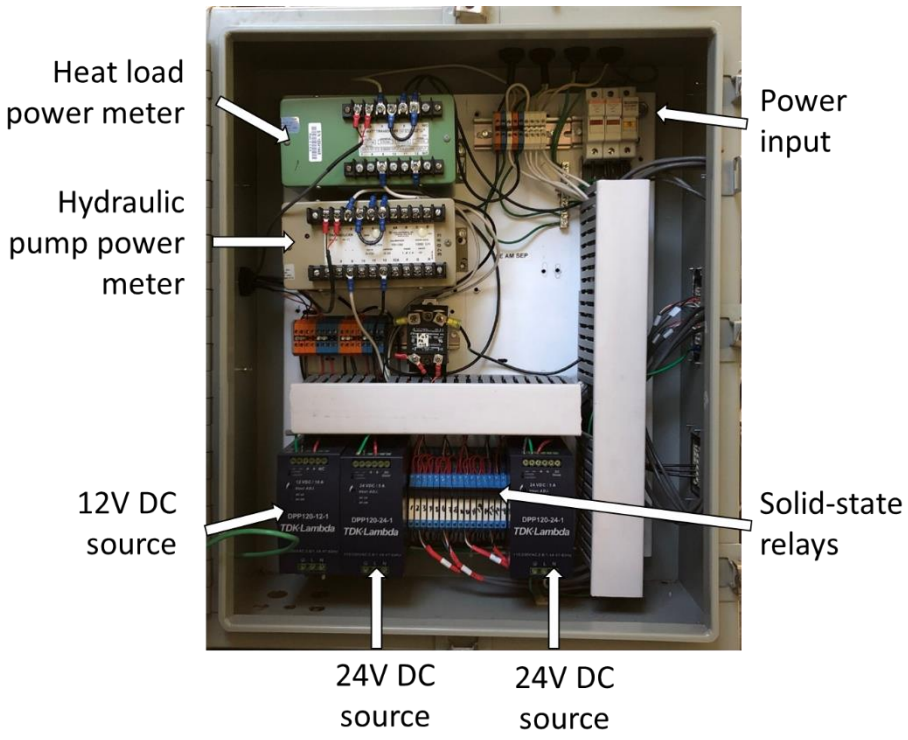

Figure 48: Main components inside the electric box

Figure 48 shows the main components inside the electric box. There are different DC power sources that power the modules that require an energy input, the solenoid valves, the heat transfer fluid pump, the load cells and displacement transducers. There are two AC power input lines that power the hydraulic pump and the electric heater. There are two power meters, one for the heat load and another one for the hydraulic pump. Everything that needs to be turned on and off is done through an array of solid-state relays that are opened and closed through the signals coming out of the NI-9476.

2.2 Experimental set-up and main results

2.2.1 One stage configuration

The active regeneration cycle applied in this experiment has four steps instead of eight, because the heat transfer and heat recovery take place simultaneously and there is no pressure balance step (there is only one regenerator). These four steps are:

1. Adiabatic loading: the hydraulic actuator compresses the Ni-Ti heat exchanger and induces the martensitic transformation. To maintain the adiabatic nature of the process and maximize the temperature increase of the Ni-Ti tubes there is no water flow during this step.
2. Heat rejection: water flows from the cold end to the hot end of the regenerator. The temperature of water increases during this process and the temperature of the regenerator decreases. This is analogous to the cold blow period in a passive regenerator.
3. Adiabatic unloading: the Ni-Ti heat exchanger is allowed to push the oil out of the hydraulic actuator and relieve the stress, reversing the martensitic transformation. To maintain the adiabatic nature of the process and maximize the temperature decrease of the Ni-Ti tubes there is no water flow during this step.
4. Heat absorption: water flows from the hot end to the cold end of the regenerator. The temperature of water decreases during this process and the temperature of the regenerator increases. This is analogous to the hot blow period in a passive regenerator.

Figure 49 shows a schematic of the Ni-Ti heat exchanger and the water loop set up to operate as a one stage active regenerator for a maximum temperature lift test. It is

composed of six flow sections labeled REG (short for “regenerator”) and T1 to T5 (T is short for “tube”).

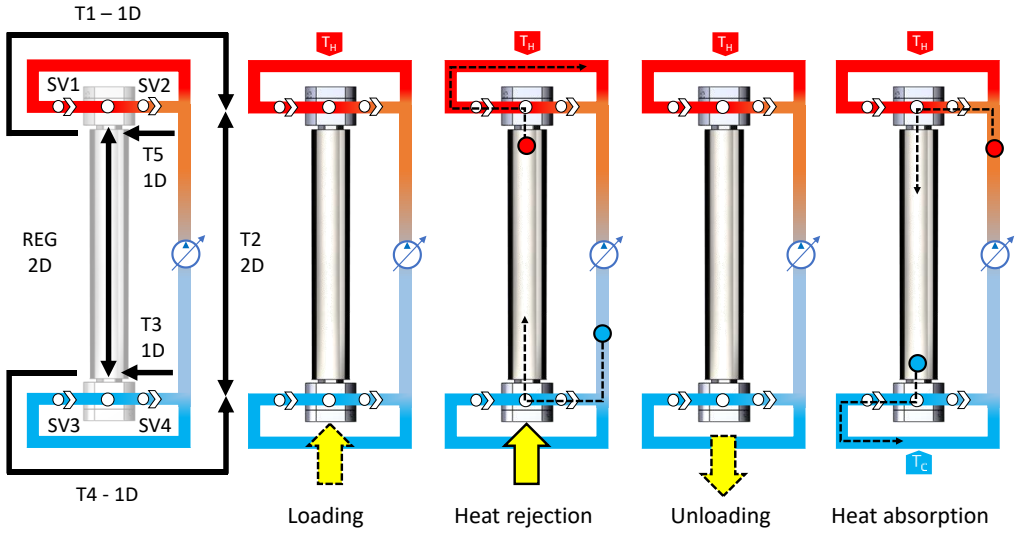

Figure 49: Schematic of maximum temperature lift test configuration

The flow direction of the heat transfer fluid inside the water loop is controlled by the direction of the pump and four solenoid valves, SV1 to SV4. T1, T5, T3 and T5 only experience flow in one direction, or no flow. T2 and REG can experience flow in both directions or no flow. During heat rejection, the water is directed from the hot side of the regenerator to T1 by opening the solenoid valve SV1. At the end of T1 there is a bifurcation. Solenoid valve SV2 is closed, and water proceeds to T2. At the end of T2 there is another bifurcation, because SV4 is open and SV3 is closed, water can proceed through the cold side of the regenerator and that completes the loop. During heat absorption the flow direction is reversed. Water is directed from the cold side of the regenerator to T4 by opening SV3. At the end of T4 there is a bifurcation. Solenoid valve SV4 is closed, and water proceeds to T2. At the end of T2 there is another bifurcation and because SV2 is

open and SV1 is closed, water can proceed through the hot side of the regenerator and that completes the loop.

During operation the temperature difference between T_H and T_C grows. This is defined as the temperature lift of the system. Because there is no heat rejection, both T_H and T_C will continue to increase, so the system will not deliver cooling, but the temperature lift will reach a steady value after the initial transient. Several parameters, geometrical (i.e. length of the regenerator, tube dimensions) and operational (i.e. cycle time, flow rate) affect how large or small the temperature gradient can be. The objective is to make it as large as possible. From the operational parameters, the loading time is determined by the capabilities of the hydraulic system and unloading time by the oil evacuation flow rate which depends on the release of elastic energy stored in the Ni-Ti tubes during unloading. Both steps are done as fast as possible and they are fixed. The two operational parameters that can be varied are the heat absorption and rejection times, and the heat transfer fluid flow rate. The performance of the regenerator is a function of a non-dimensional parameter, the utilization factor that relates these two parameters. It is defined by Equation 15 and it represents the volume fraction of heat transfer fluid that is displaced from the regenerator during each heat exchange step, with respect to the total volume inside the regenerator.

$$V^* = \frac{\dot{m}_f c_{p,f} t_{HT}}{\rho_f c_{p,f} V_{reg}} \qquad \text{Equation 15}$$

Table 2 shows the operating parameters used for two relevant experiments.

Table 2: Experimental parameters for tests TL-1, TL-2, CC-1, CC-2 and CC-3

Parameter [unit]	TL-1	TL-2	CC-1	CC-2	CC-3
Loading time [s]	5	6	4	4	4
Heat rejection time [s]	4.9	6	4.9	4.9	4.9
Unloading time [s]	2	1	2	2	2
Heat absorption time [s]	4.9	6	4.9	4.9	4.9
Strain [%]	3.5	4.7	3.5	3.5	3.5
Utilization factor [-]	0.63	~0.7	0.63	0.63	0.63
Cooling capacity [W]	-	-	0	8.9	13.2

Figure 50 shows the time evolution of T_H and T_C during the first 30 minutes of tests TL-1 and TL-2. Figure 51 shows the time evolution of the temperature lift, T_H - T_C.

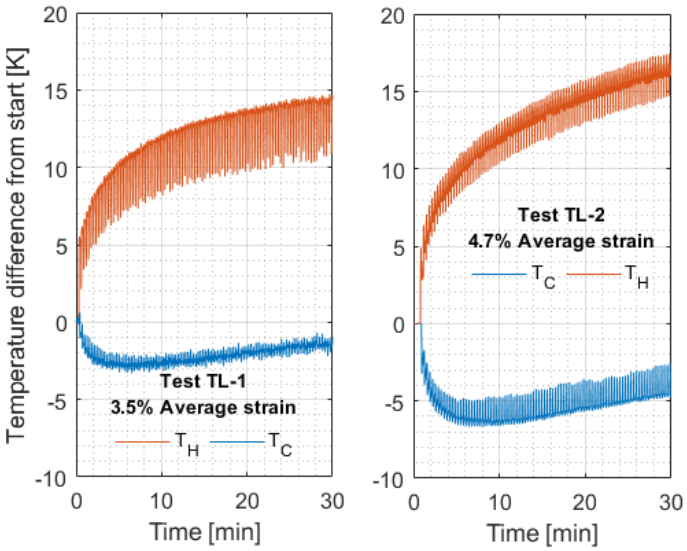

Figure 50: Time evolution of T_H and T_C for an active regeneration cycle with an average strain of 3.5% and 4.7%

The temperature lift in test TL-1 is larger than the one in test TL-2. T_H increases continuously since the beginning of the test, and T_C initially decreases until the first ten minutes after which the trend is reversed. Increasing the strain is an effective way to increase the temperature lift of the system. The average temperature lift after 30 minutes

was 16.7 K for an average strain of 3.5%, and 21.2 K for an average strain of 4.7% after 45 minutes.

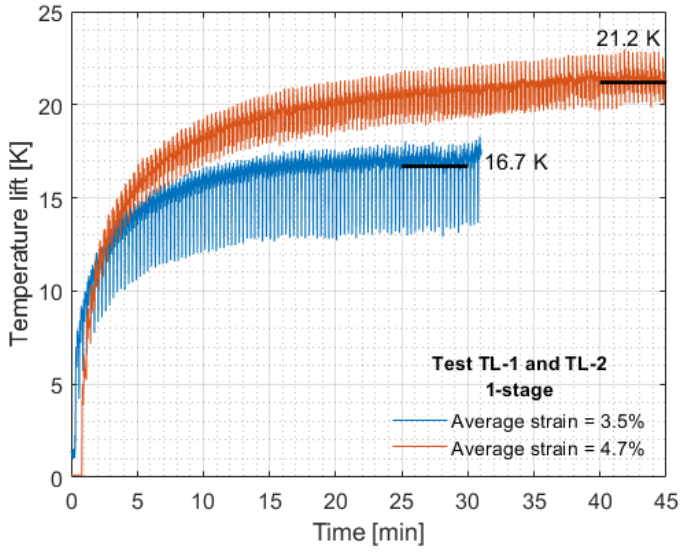

Figure 51: Experimental measurement of temperature lift for 3.5% and 4.7% strain

As the average strain increases, the load increases and the likelihood of failure of the regenerator increases. Failure of a regenerator doesn't involve the catastrophic failure of all the tubes simultaneously, it can be caused by the failure of a single one or a few (see Figure 41 and Figure 42). When a tube fails, the water flow is disrupted by leakage affecting the regenerator performance. Figure 51 also shows that despite the fact that the temperature lift was larger than had been previously achieved (8 K) and larger than any reported temperature lift value at the time of 19.9 K (Kurt Engelbrecht et al., 2017; Tušek et al., 2016), is still not large enough for a practical application.

Figure 52 shows a schematic of the set up for the cooling capacity measurement. The operating steps are the same four steps, but there are two main differences in the heat rejection and heat absorption steps. To allow the temperature of the water flowing through T4 to decrease, it is necessary to reject heat at T1 during the heat rejection step. This was done by removing T1, and discarding the water coming out of the hot end of the regenerator. That water, that would have fed T2, is replaced by water at room temperature coming out of a reservoir. This reproduces the approach used during testing of the previous generation system.

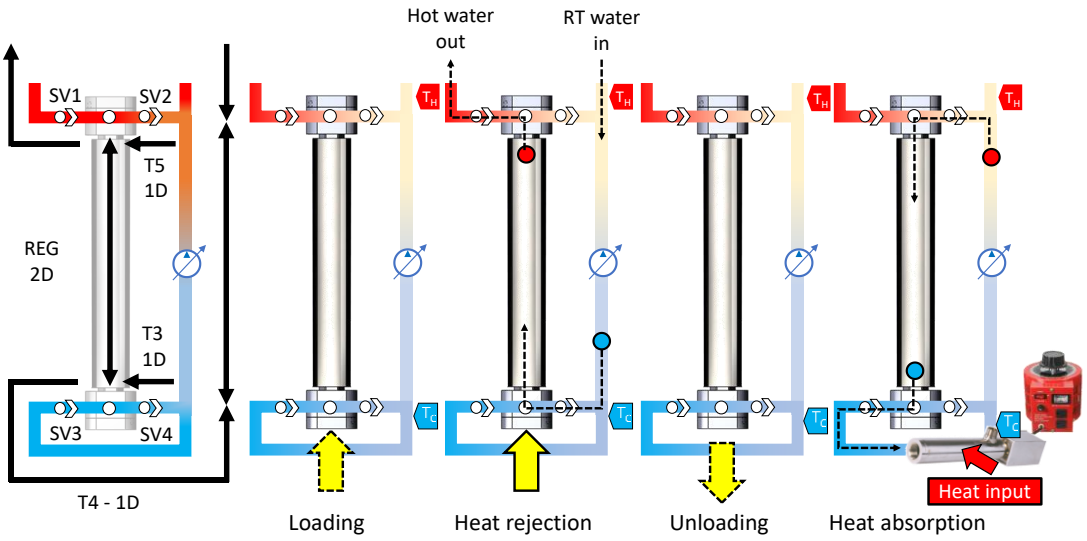

Figure 52: Schematic of cooling capacity test configuration

Figure 53 shows the time evolution of the useful temperature lift for various cooling loads and Figure 54 shows the results of the cooling capacity as a function of the useful temperature lift measurements.

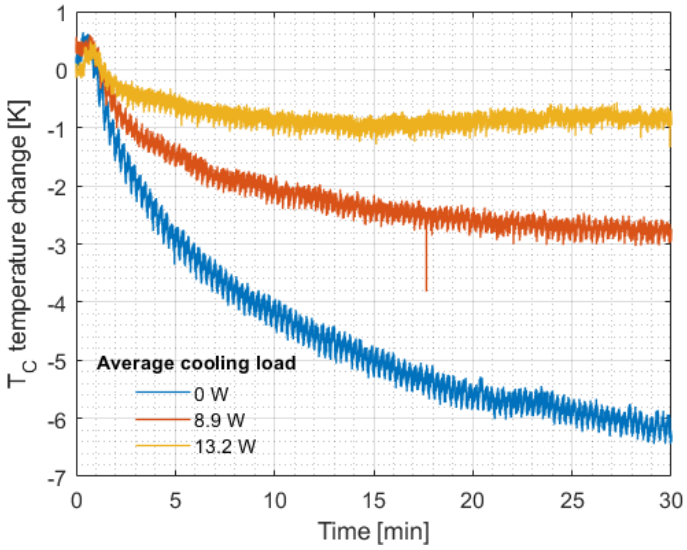

Figure 53: Time evolution of T_C - T_{amb} in tests CC-1, CC-2 and CC-3

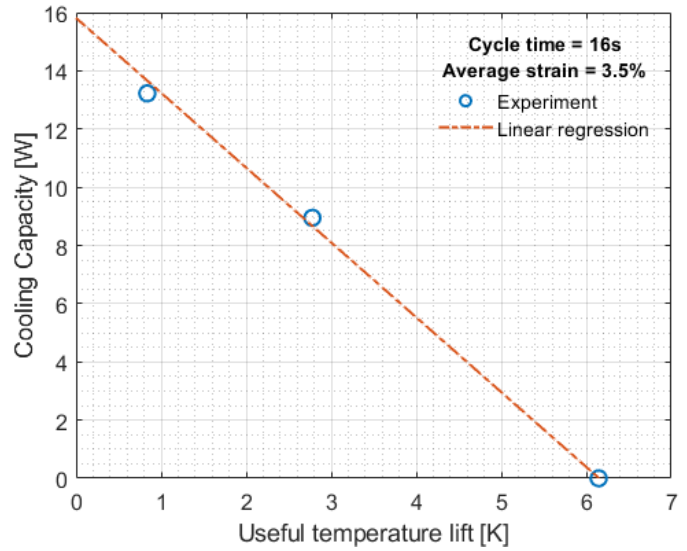

Figure 54: Cooling capacity-temperature lift performance of the one stage configuration.

The maximum cooling capacity can be obtained by extrapolating the linear trend to 0 K and it is approximately 16 W, while the maximum useful temperature lift measured is 6.2 K. The cooling capacity of the system operated in this configuration is low due to various

factors: the average strain level is only 3.5%, the number of regenerators being used is 1 and the mass flow rate was determined such that the temperature lift is maximized. Larger cooling capacities could be achieved if the mass flow rate increased, but the maximum temperature lift would decrease. Despite that, the temperature lift is higher than the one measured with in the third-generation system (5 K) with a smaller strain (3.5% instead of 4.5%). From that point of view, the system can be considered a superior alternative. Low cooling capacity can be addressed by scaling up the system, for example, increasing the mass of Ni-Ti material. To increase the temperature lift, other strategies need to be pursued.

2.2.2 Two-stage configuration

Staging allows a cooling system to increase its operating temperature lift by connecting two regenerators in series such the total temperature lift is composed by the addition of the temperature span along each individual regenerator.

Figure 55 shows a schematic of the two-stage system configuration. The heat transfer fluid loop is the same as in the one stage system configuration, with the only precaution of making the tube segment T2 long enough to prevent the passage of fluid from the hot side to the cold side. As with the one stage system configuration, the first step is to determine the maximum temperature lift that can be obtain without heat rejection and absorption. Table 3 shows the operating parameters used for two relevant experiments.

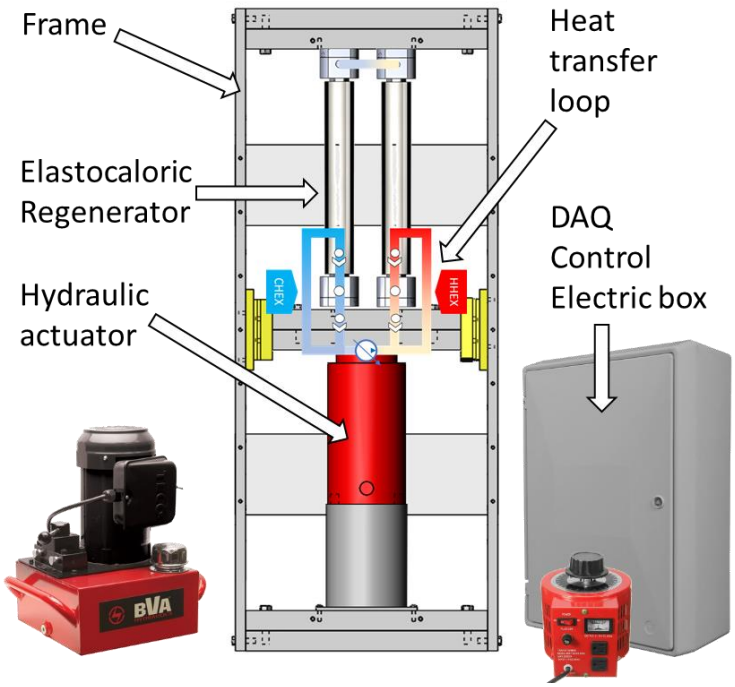

Figure 55: Schematic of two-stage system configuration

Table 3: Experimental parameters for tests TL-3, CC-4 and CC-5

Parameter [unit]	TL-3	CC-4	CC-5
Loading time [s]	6	5	5
Heat rejection time [s]	4.9	4.4	4.4
Unloading time [s]	2	2	2
Heat absorption time [s]	4.9	4.4	4.4
Strain [%]	3.5%	3.5%	3.5%
Utilization factor [-]	0.31	0.77	0.77
Cooling capacity [W]	-	12.5	19.5

Figure 56 shows the time evolution of T_H and T_C during the first 30 minutes of the test for both one stage and two-stage configurations with the same average strain of 3.5%, such that the effect of staging is clearly visualized. The temperature lift is improved by staging.

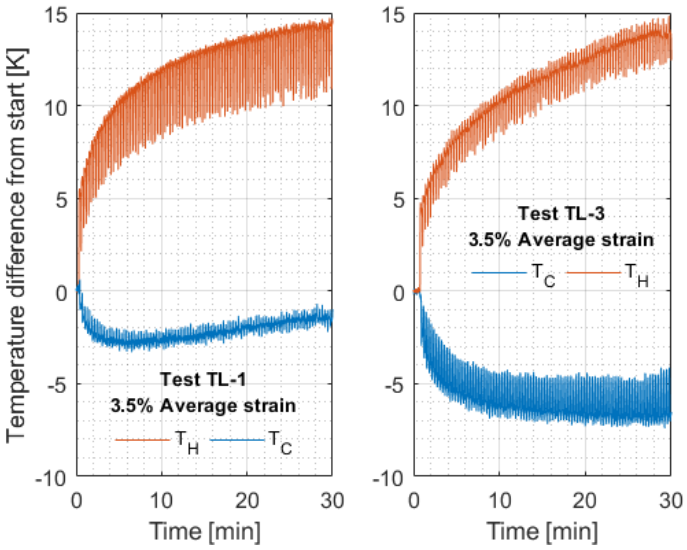

Figure 56: Time evolution of T_H and T_C for a one- and a two-stage system configuration

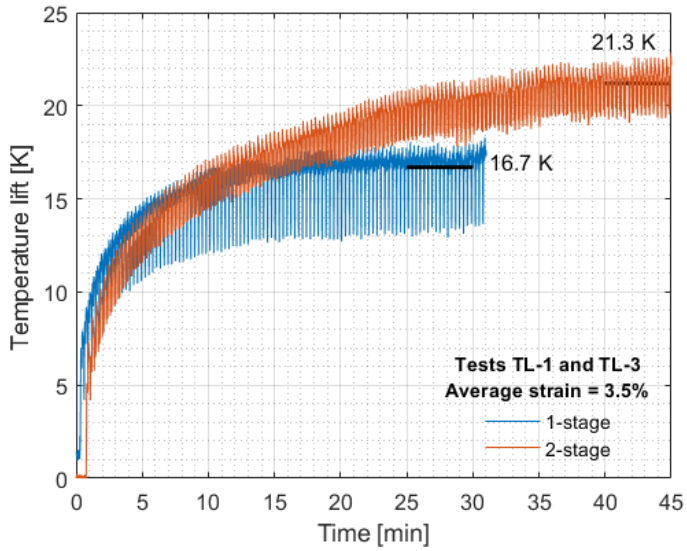

Figure 57: Experimental measurement of temperature lift for one stage and two-stage configurations at 3.5% strain

Figure 57 shows that after 45 minutes, the temperature lift measured with a two-stage configuration is 21.3 K, which is larger to the 16.7 K that was obtained with the one stage configuration at 3.5% strain and 21.2 K at 4.7% strain. From the point of view of

robustness, it is safer to operate the system compressing the Ni-Ti tubes to just 3.5% rather than 4.7%.

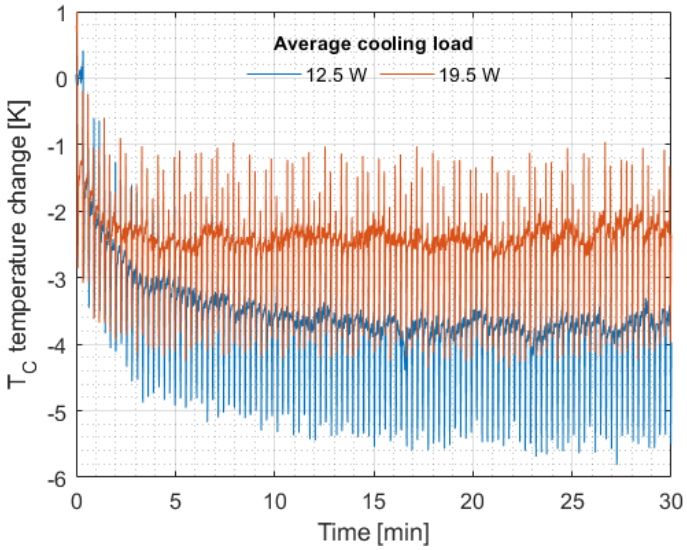

Figure 58: Time evolution of T_C - T_{amb} in tests CC-4 and CC-5

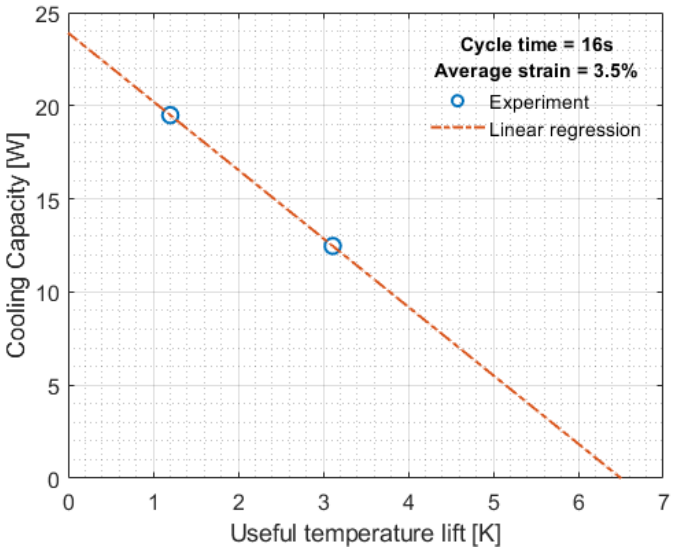

Figure 59: Two-stage system cooling capacity and temperature lift for V* = 0.8

Figure 58 shows the useful temperature lift measured for two cooling loads and Figure 59 shows the cooling capacity and useful temperature lift plot. Only two measurements were made due to experimental limitations. Based on these two measurements, the maximum temperature lift can be estimated by extrapolation to be 6.5 K, while the maximum cooling capacity is estimated to be 24 W.

Figure 60 shows the results for both, the one stage and the two-stage configurations in the same plot.

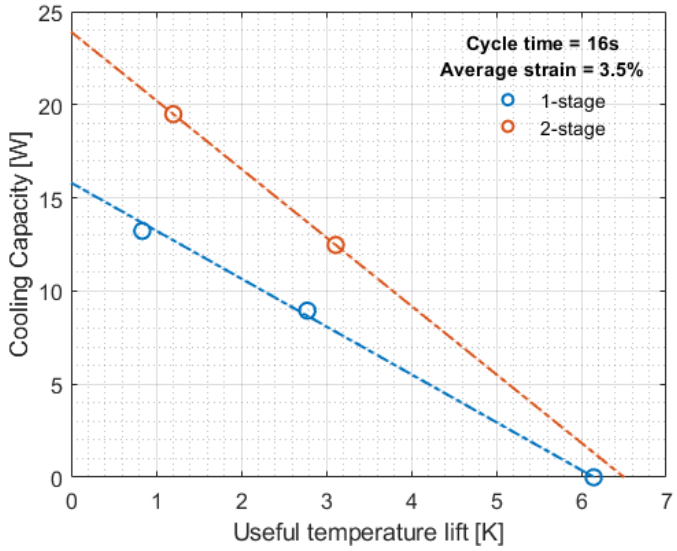

Figure 60: Comparison of cooling capacity experiments for one- and two-stage configurations

2.3 Results analysis and discussion

All physical configurations tested in this work were modeled on Matlab®/Simulink® environment. There were three developmental stages:

1. The experimental data was used to assist the model complexity.
2. Upgraded versions of the model allowed the discovery of operating conditions of superior performance.
3. A reconfiguration of the system was done computationally to be later studied experimentally.

2.3.1 General modeling approach

The most complex part to simulate is the regenerator. To solve the time-dependent governing equation, the regenerator control volume was discretized in the longitudinal direction and the energy balance was established for each discrete element. The following assumptions were applied:

1. The governing equation is simplified to a 1-D problem due to the radial symmetry of the problem. This assumes that the thermal behavior of the fluid and the regenerator of each one of the 19 tubes is uniform in any cross-section.
2. Because the cross section of the tube is small compared to the heat transfer area, the heat loss between the Ni-Ti and the loading head through conduction is assumed to be negligible, thus applying an adiabatic boundary condition at the ends of the regenerator.
3. A single-crystalline SMA model is applied to describe Ni-Ti behavior.

The solid, fluid and insert governing temperature evolution equations can be seen in Equation 16, Equation 17 and Equation 18 respectively.

$$\underbrace{\frac{dT_s}{dt}}_{\substack{Temperature\\ change\ rate}} = \underbrace{\frac{k_s}{(\rho c)_s}\frac{d^2T_s}{dx^2}}_{Conduction} - \underbrace{\frac{h}{(\rho c)_s}\delta_s(T_s - T_f)}_{\substack{Convection\\ Fluid-Ni-Ti}} + \underbrace{\frac{\rho_s \Delta s}{(\rho c)_s}\frac{dx_M}{dt}T_s}_{\substack{Elastocaloric\\ effect}} + \underbrace{\frac{\sigma}{(\rho c)_s}\frac{d\varepsilon}{dt}}_{\substack{Mechanical\\ work}} \quad \text{Equation 16}$$

$$\underbrace{\frac{dT_f}{dt}}_{\substack{Temperature\\ change\ rate}} = \underbrace{\frac{k_f}{(\rho c)_f}\frac{d^2T_f}{dx^2}}_{Conduction} - \underbrace{\frac{h}{(\rho c)_f}\delta_f(T_f - T_s)}_{\substack{Convection\\ Fluid-Ni-Ti}} - \underbrace{\frac{h}{(\rho c)_f}\delta_f(T_f - T_i)}_{\substack{Convection\\ Fluid-Insert}} - \underbrace{\frac{\dot{m}}{\rho_f A}\frac{dT_f}{dx}}_{Advection} \quad \text{Equation 17}$$

$$\underbrace{\frac{dT_i}{dt}}_{\substack{Temperature\\ change\ rate}} = \underbrace{\frac{k_i}{(\rho c)_i}\frac{d^2T_i}{dx^2}}_{Conduction} - \underbrace{\frac{h}{(\rho c)_i}\delta_i(T_i - T_f)}_{\substack{Convection\\ Fluid-Insert}} \quad \text{Equation 18}$$

Table 4 shows the physical properties for Ni-Ti, water and PTFE.

Table 4: Physical properties of Ni-Ti, insert material and heat transfer fluid

Material	Ni-Ti	PTFE	Water
k [W $K^{-1}m^{-1}$]	18	0.25	0.6065
ρ [kg m^{-3}]	6,500	2,200	1,000
c_p [J $kg^{-1}m^3$]	500	960	4,184
ν_f [m2 s^{-1}]	-	-	9.6E-7

Table 5 shows the geometrical information of a Ni-Ti heat exchanger.

Table 5: Geometrical information of the Ni-Ti tubes

Ni-Ti tubes	19
OD [m]	3.759E-3
ID [m]	4.718E-3
L [m]	0.254

In the solid equation, Equation 16, to solve the elastocaloric effect and the mechanical work terms it is necessary to use a constitutive model Ni-Ti which takes into account temperature and stress. The Müller-Achenbach-Seelecke thermodynamic kinetic model (Seelecke and Müller, 2004) has been successfully applied (Qian et al., 2017) and is able to establish the relationship between the applied stress, the temperature and the phase change rate.

The martensitic phase transformation rate can be evaluated with Equation 19. On the right-hand side of this equation we can see p^{MA} and p^{AM}, which represent the thermodynamic probability that one domain transforms from Martensite into Austenite and from Austenite into Martensite respectively. These probabilities are a function of the temperature and the stress, and the interplay between stress and temperature will determine which one will dominate and in which direction the transformation will proceed.

$$\dot{x}_M = x_A p^{AM}(T_s, \sigma) - x_M p^{MA}(T_s, \sigma) \qquad \text{Equation 19}$$

The Austenite and Martensite phase fractions are constrained by the condition shown in Equation 20 at any given time.

$$x_M + x_A = 1 \qquad \text{Equation 20}$$

The values of p^{MA} and p^{AM} can be evaluated using Equation 21 and Equation 22.

$$p^{MA}(T_s,\sigma) = \frac{1}{\tau}\cdot\frac{exp\left(-b\left(\frac{(\sigma_M(T_s)-\sigma)}{E_M}\right)^2\right)}{erfc\left(\sqrt{b}\left(\frac{(\sigma_M(T_s)-\sigma)}{E_M}\right)\right)} \quad \text{Equation 21}$$

$$p^{AM}(T_s,\sigma)$$

$$= \frac{1}{\tau}\cdot\frac{exp\left(-a\left(\frac{(\sigma_A(T_s)-\sigma)}{E_A}\right)^2\right)}{erf\left(\sqrt{a}\left(\frac{(\sigma_A(T_s)-\sigma)}{E_A}\right)\right)+erf\left(\sqrt{a}\left(\frac{(\sigma_A(T_s)+\sigma)}{E_A}\right)\right)} \quad \text{Equation 22}$$

The coefficients a and b are defined by Equation 23 and Equation 24.

$$a = \frac{E_A V_L}{2k_B T_s} \quad \text{Equation 23}$$

$$b = \frac{E_M V_L}{2k_B T_s} \quad \text{Equation 24}$$

As previously mentioned the transformation stress is a function of the temperature, and specifically a linear correlation is adopted as show in Equation 25 and Equation 26.

$$\sigma_A(T_s) = C_A(T_s - T_{As}) \quad \text{Equation 25}$$

$$\sigma_M(T_s) = C_M(T_s - T_{Ms}) \quad \text{Equation 26}$$

And finally, the constitutive equation of the material that relates the phase transition to the strain, Equation 27.

$$e(\sigma, T_s, x_M) = x_A \frac{\sigma}{E_A} + x_M \left(e_T + \frac{\sigma}{E_M} \right) \quad \text{Equation 27}$$

The flow inside the regenerator is laminar, and the Kay's correlation was used considering the entrance effect.

$$Nu_D = 3.66 + \frac{0.0668\ Gz_D}{1 + 0.004 {Gz_D}^{2/3}} \quad \text{Equation 28}$$

$$h = \frac{Nu_D . k_f}{D_h} \left(\frac{1}{1 + \frac{Nu_D . k_f}{5 . k_s}} \right) \quad \text{Equation 29}$$

2.3.2 Model validation

The model results were compared against experimental measurements from a simple configuration that is shown in Figure 61. An open loop test has four main steps:

1. Loading: The Ni-Ti tubes are compressed adiabatically, they go through the stress-induced martensitic transformation and they increase their temperature.
2. Heat rejection: Water flows through the Ni-Ti tubes until all the heat is extracted and they reach room temperature. During this step the tubes remain compressed.
3. Unloading: The Ni-Ti tubes are relieved of the stress and they go through the reverse martensitic transformation. They decrease their temperature.

4. Heat absorption: Water flows through the tubes again until they absorb enough heat to increase their temperature back to room temperature.

The temperature of the water at the inlet and outlet were recorded continuously. This was repeated for multiple strain levels and the measured change in water temperature was compared to the change predicted by the model.

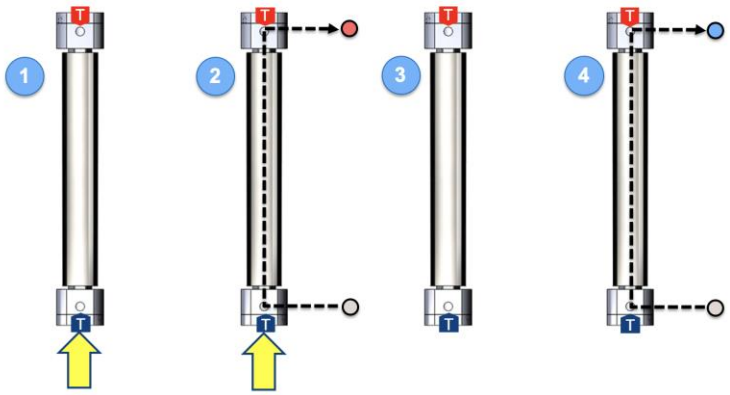

Figure 61: Schematic of open loop test procedure

Figure 62 shows the measured and predicted temperature change at 3.5% strain. The model predictions follow closely the experimental results. The temperature measurements tests were also used to calculate the total heat exchanged between the Ni-Ti tubes and the water, in the forward and reverse transformation for each strain. To estimate the total heat exchanged, the heat exchange rate was integrated over time according to Equation 30. Experimentally, the heat exchange rate was estimated from the difference between the water temperature at the inlet and the outlet of the regenerator, the mass flow rate and the heat capacity of water.

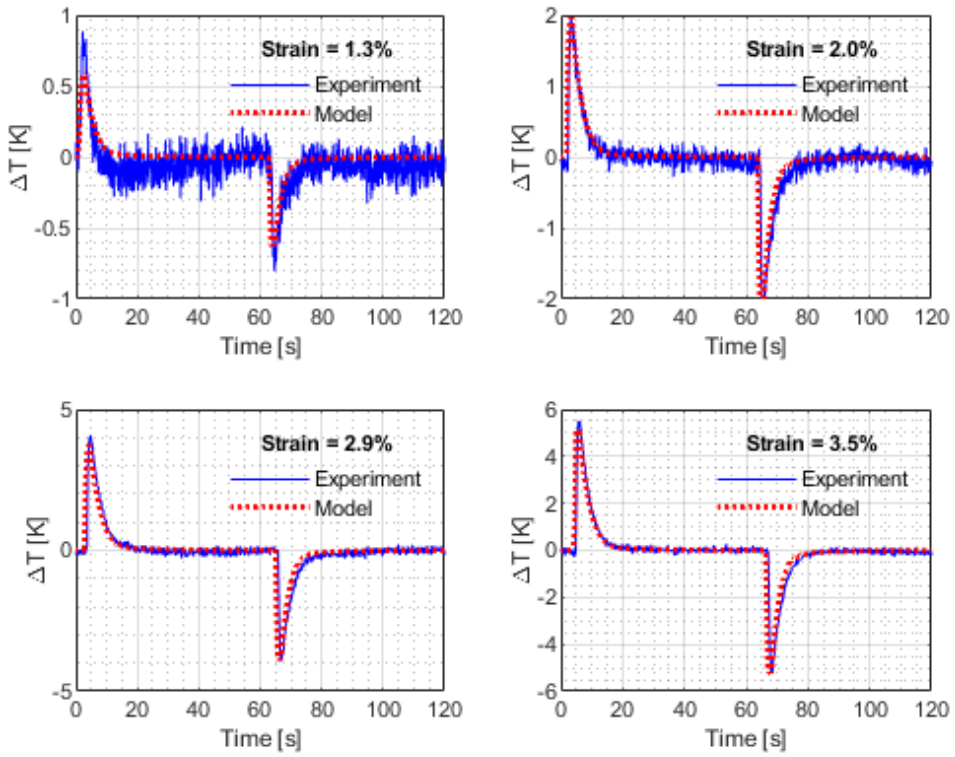

Figure 62: Temperature difference between inlet and outlet for different strain levels

$$\dot{Q}(t) = \dot{m}c_{p,f}\left(T_{out}(t) - T_{in}(t)\right) \rightarrow Q = \int_{t_1}^{t_2} \dot{Q}(t)\, dt \qquad \text{Equation 30}$$

Figure 63 shows the total heat rejected and absorbed as a function of the average strain applied to the regenerator. There is a good agreement between the results, the model predictions and previous results. The next step is to expand the model to include more complex configurations and flow patterns.

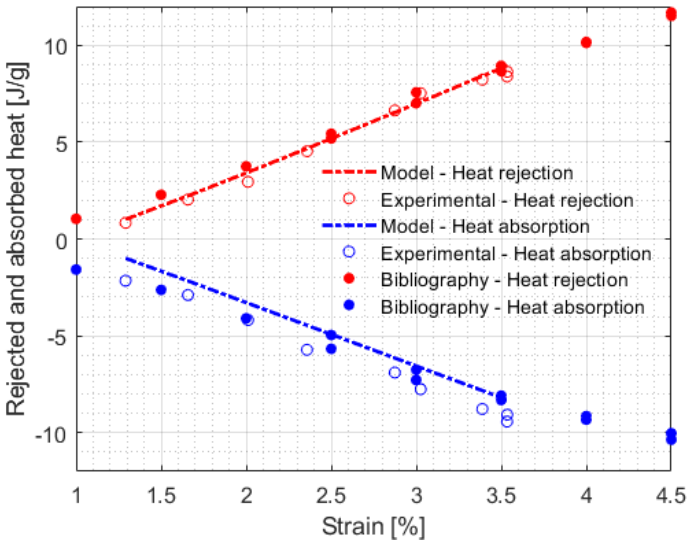

Figure 63: Total heat exchanged during heat absorption and heat rejection in open loop test

2.3.3 Modeling the response of the one stage and two-stage regenerators

Figure 64 shows the predicted temperature lift and five experimental measurements. The prediction shows that as the utilization factor increases, the temperature lift increases until a certain point beyond which performance degrades. There is a “hump” around the utilization factor of 0.4 for the one stage system and at 0.2 for the two-stage system. The utilization factor is calculated based on the total volume of the regenerator, which is twice as large for the two-stage regenerator. Since the heat transfer times are kept constant, these two utilization factor numbers represent an equivalent volume of fluid, which is equal to the volume inside the loading heads and connecting tubing between the loading heads and SV1 and SV3. This is the entire volume that needs to be displaced before the fluid from the regenerator can reach T1. As the utilization factor increases more of the water coming out of the regenerator can make it to T1 and T4 and the temperature lift continues to

increase until reaching a peak, which for the one stage occurs at V* = 0.775 and for the two-stage occurs at 0.45. Beyond those values the heat regeneration is not as effective and the temperature lift decreases.

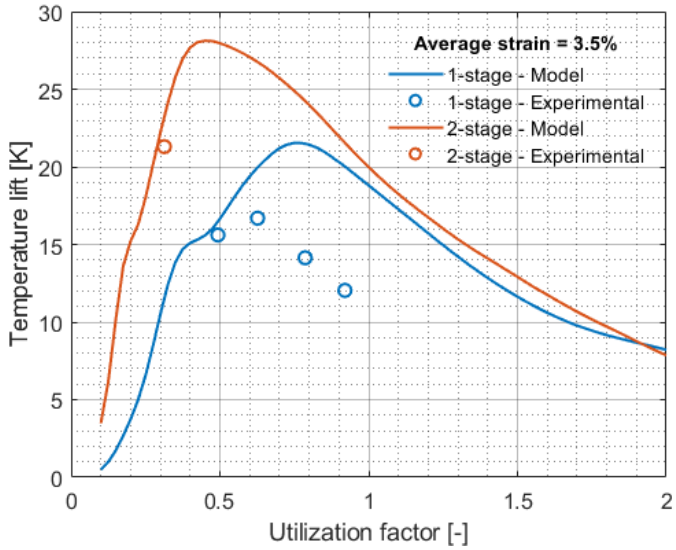

Figure 64: Model prediction and experimental measurements of temperature lift as a function of utilization factor.

The experimental results showed a maximum 16.7 K for a utilization factor equal to 0.625 for the one stage configuration and 21.3 K for a utilization factor equal to 0.275 for the two-stage configuration. The experimental values are approximately 22-24% below the prediction. Despite these differences, the model is able to capture the main physical behavior of the system and could assist in determining operating conditions.

Figure 65 shows the model prediction for the cooling capacity and useful temperature lift of the one stage and two-stage configurations. For each simulation the mass flow rate was set as in the experiments. The relative behavior between configurations similar to the one

measured and showed in Figure 60, however both the cooling capacity and temperature lift are overestimated by the model.

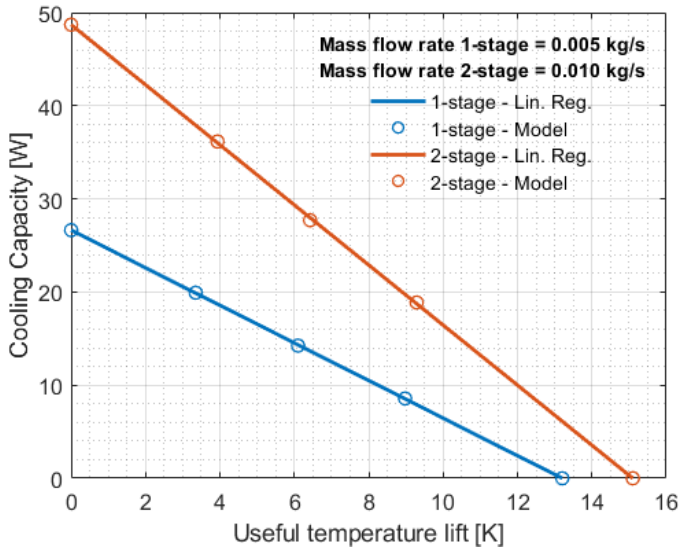

Figure 65: Cooling capacity prediction for one- and two-stage configurations.

The model is only an idealized representation of the physical system. No degrading mechanisms were included at this stage, such as thermal dispersion, and a 1-D simplification assuming the characteristics of the flow through each individual tube is the same. Figure 66 shows the prediction and experimental measurement for T_H and T_C. The differences between prediction and experiment are larger for T_C than T_H.

A more specific explanation is related to the energy balance, in particular to the mechanical work term in Equation 16.

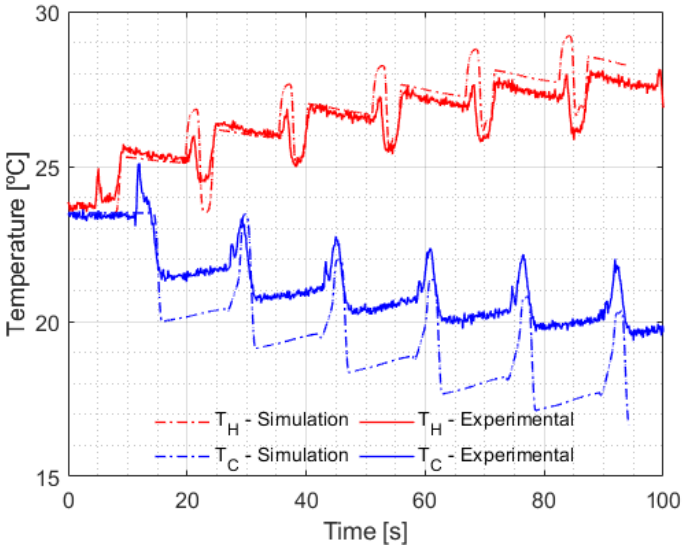

Figure 66: T_H and T_C measurement and model prediction

Figure 67 shows the difference between the measured and model-based Ni-Ti mechanical response. Differences in the predicted and observed energy dissipated due to the hysteresis of the phase transformation ultimately make their way into the energy balance of the system and affect the temperature predictions. Equation 6 and Equation 16 show that the elastic work done on the Ni-Ti tubes plays a role in the heat released during the forward transformation and the work done by the Ni-Ti tubes during unloading plays a role in the heat absorbed during the reverse transformation. Several factors contribute to these differences. The material model does not include any of the specific consideration of the particular state of stress the material is subjected to inside the tube holder. Another limitation is that it can only represent the behavior of a single-crystalline material, while the materials that are used to build the Ni-Ti heat exchangers are polycrystalline. The quantities in Figure 67 are force and displacement, which means that the integration of these curves is equal to the work done upon the material during loading, and done by the

material against the actuator upon unloading. The difference is the energy lost to hysteresis. The energy lost by hysteresis in one cycle is larger in the experiment than the one predicted by the model.

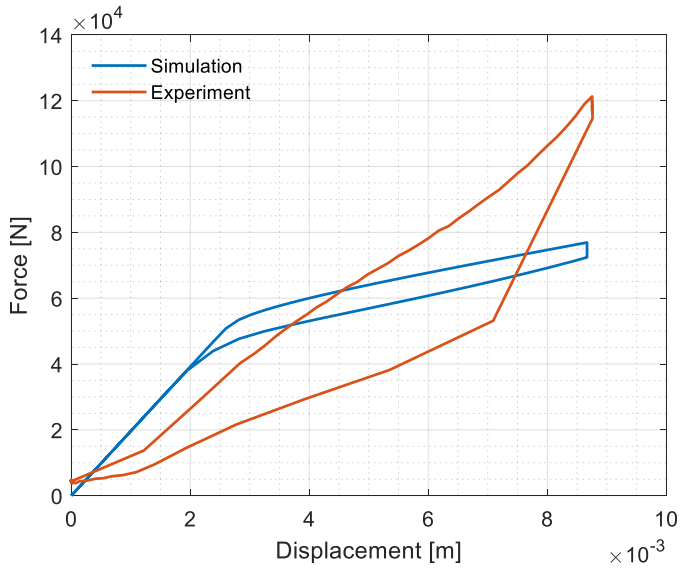

Figure 67: Experimental and model mechanical response

Table 6: Experimental and model-based mechanical work calculation

Mechanical work	Loading [J.g^{-1}]	Unloading [J.g^{-1}]
Simulation	2.33	2.13
Experiment	2.40	1.57

Table 6 shows the calculated values for the loading work and unloading work for both simulation and experiment. The loading work is very close in both cases, which is consistent with the observation that the T_H prediction matches very closely with experiment. The unloading work is approximately 0.5 J/g larger in the simulation than in the experiment. If the material does more work upon unloading at the expense of its internal energy, this will result in a larger decrease in temperature. Once again, this is consistent

with the differences between the experiment and prediction, being the predicted T_C lower than the measured one.

2.3.4 Modeling the response of two-stage, three-stage and four-stage regenerators

After analyzing the experimental results and the predictions for the one- and two- stage configurations, the numerical model was further expanded to three- and four-stage configurations. Figure 68 shows temperature lift prediction for each configuration as a function of utilization factor for a constant cycle time. As the number of stages increases, the temperature lift increases as well, but for each additional stage added, the additional temperature lift is only marginally larger. From one- to two-stage the increase is 5K, from two- to three-stage is 2K and from three- to four-stage is 1K. As the dotted lines show, kinetics can also play a role: it takes longer to reach the steady state, as the number of Ni-Ti heat exchangers increases.

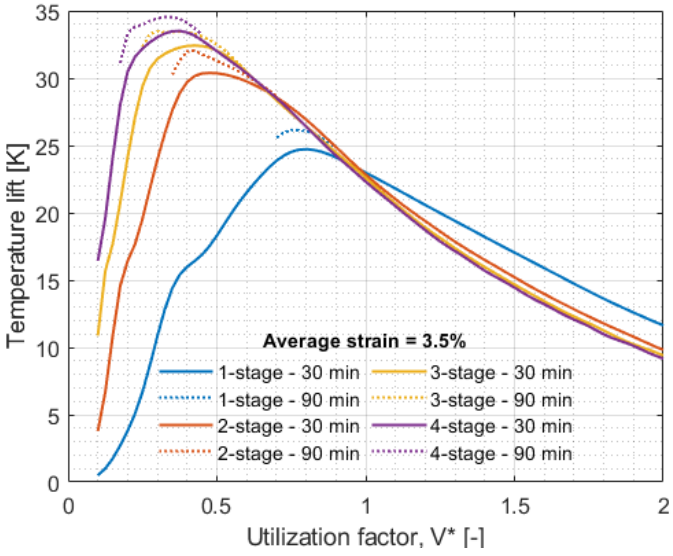

Figure 68: Temperature lift model prediction for one-, two-, three- and four-stage configurations

Figure 69 shows the cooling capacity performance of each configuration. The cycle time was kept constant, and the utilization factor was chosen to be the one at the peak of each curve. The total volume utilized in to calculate the utilization factor is equal to the sum of the volume of each individual Ni-Ti tube holder, so mass flow rate at V* = 0.8 for a one stage system represents the same mass flow rate at V* = 0.4 for a two-stage system, considering that the heat transfer time doesn't change (which is the case). Even if by adding stages, the amount of Ni-Ti material being cycled increases, the final cooling capacity does not increase, nor does the temperature lift.

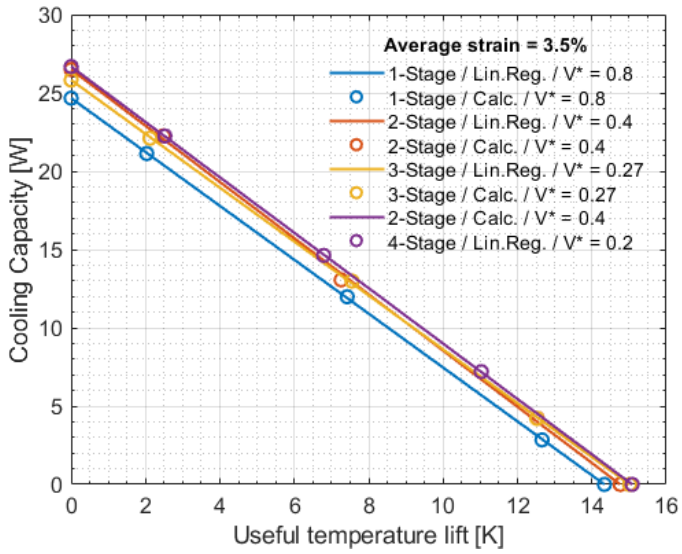

Figure 69: Cooling capacity prediction for one-, two-, three- and four-stage configurations

Chapter 3: Inhomogeneous strain distribution

3.1 One stage regenerator configuration

In the section "Thermodynamics of stress-induced martensitic transformation" it was presented through a thermodynamic analysis that the stress required to induce the martensitic transformation increases with temperature. This is something that is normally observed during the experiments. Figure 70 shows how the maximum force level increases, for the same average strain, when heat is not allowed to leave the system in the closed loop configuration with respect to the open loop configuration.

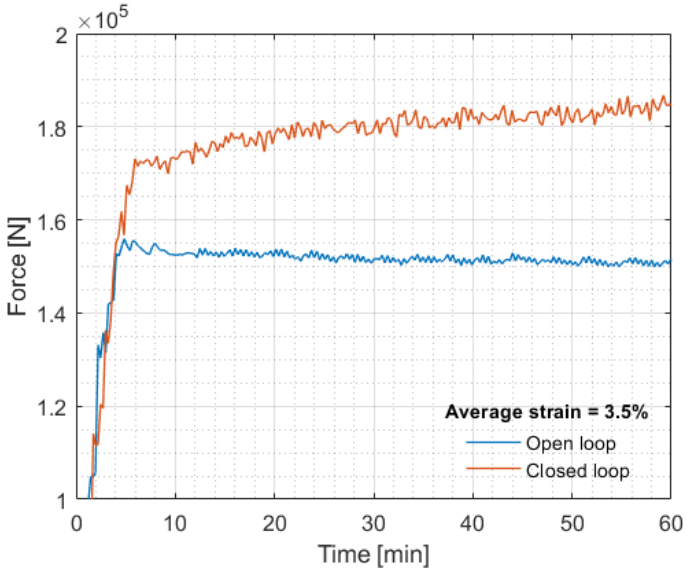

Figure 70: Maximum cycle force as a function of time for closed loop and open loop configurations

The numerical model previously presented allows for the estimation of the local strain along the regenerator. Up to this point only the average strain was referred to because it is

based on the only direct measurement accessible experimentally, the total displacement. Figure 71 shows the local stress-strain curves for 50 discrete position along the regenerator over one complete cycle after the temperature gradient is established and with an average strain of 3.5%. The blue line represents the cold end of the regenerator, the red line represents the hot end of the regenerator, the green lines represent intermediate locations, and the black dotted line represents the average stress-strain response, with the average strain calculated as the total displacement divided by the initial length of the regenerator.

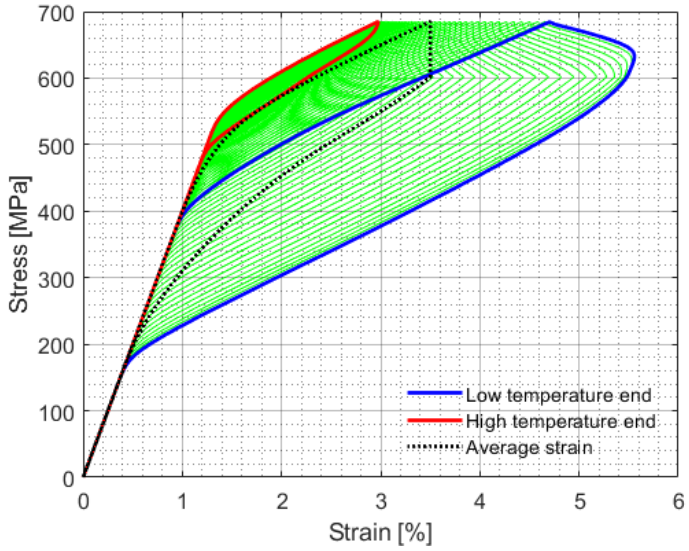

Figure 71: Model prediction for full-cycle steady-state stress-strain response along the regenerator. Green curves intermediate locations between the hot and cold ends.

Two conditions apply to the mechanics of the problem and they are the following:

1. The stress at every discrete position along the regenerator is the same, and
2. The sum of the local displacements, each calculated as the product between the local strain and the initial length of the discrete element, must be equal to the total displacement.

As the temperature of the material increases, the stress required to induce the transformation increases. Since the applied stress is the same along the regenerator, the local strain response is a function of the local temperature. High temperature regions will have a lower strain, while low temperature regions will have a higher strain, and according to the model predictions these differences can be significant.

Figure 72 shows another way to visualize this data, by looking at the local strain as a function of time.

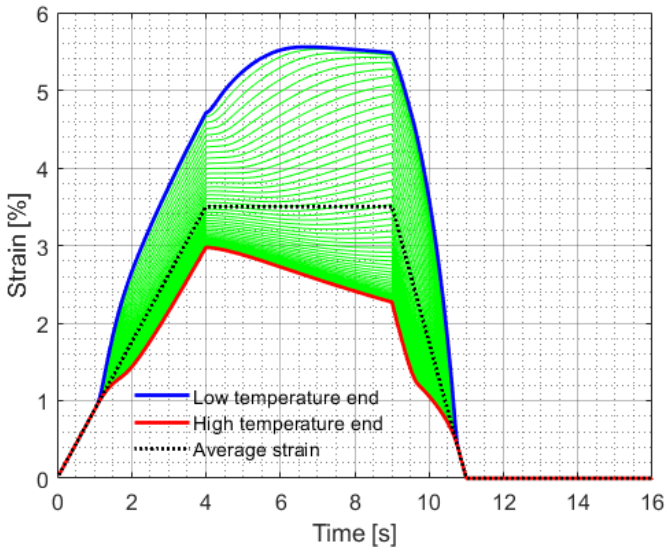

Figure 72: Model prediction for full-cycle steady-state strain response along the regenerator as a function of time. Green curves are intermediate locations between the hot and cold ends.

This shows more clearly what happens with the local strain during the different steps of the cycle. This uneven strain distribution develops during loading and worsens during the heat rejection step. The heat transfer fluid enters the regenerator through the cold end and absorbs heat from the regenerator. As the temperature of the regenerator decreases, the

total displacement is maintained constant (as shown in by the black dotted line), but the local displacements can vary without affecting their sum. As a result of the local temperature and stress evolution, the local strain is reallocated such that the lower temperature end of the regenerator deforms up to 5.6% while the high temperature end actually reverses the transformation prematurely to 2.3%. This shows a fundamental limitation of this type of system, because even if the system is operating at a low strain regime in average, sections with lower temperature will be at high strain regimes. During the unloading step all the strain is recovered and during the heat absorption step the strain remains equal to zero.

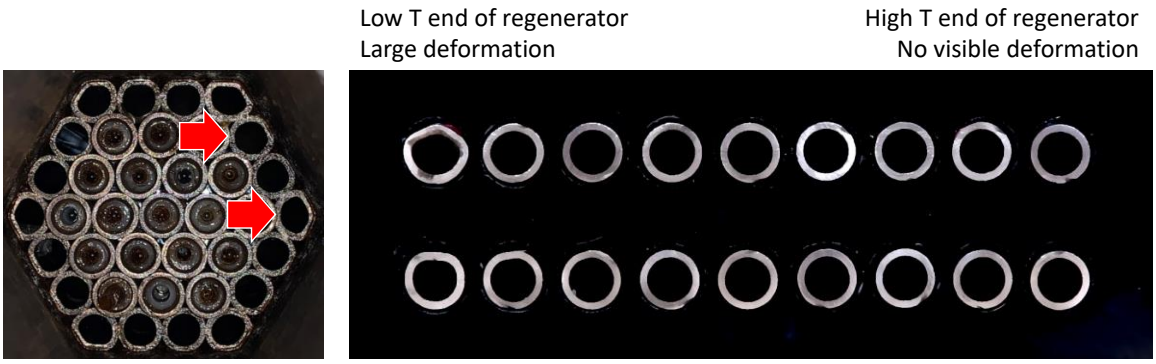

Figure 73: Various cross sections of two stainless steel tubes

Figure 73 shows the cross-section of two representative stainless steel tubes at different locations along its length. One comes from the corner of the hexagonal cut-out from the tube holder, the other comes from the flat side. The cross sections appear progressively less deformed as they are farther from the cold end of the regenerator. This is consistent with the uneven strain predicted by the model. Since the solid is incompressible, the tube must expand radially to allocate the longitudinal strain. This expansion is proportional to the compressive strain and it would result in the deformation of the stainless steel tubes.

Figure 74 shows what the strain differences along the regenerator mean in terms of martensitic phase fraction at the start and at the end of the heat rejection step (t = 4s and t = 9s). The martensitic phase fraction is directly related to the adiabatic temperature change upon unloading, so it is a good indicator of the potential thermal effect of these differences in strain along the regenerator.

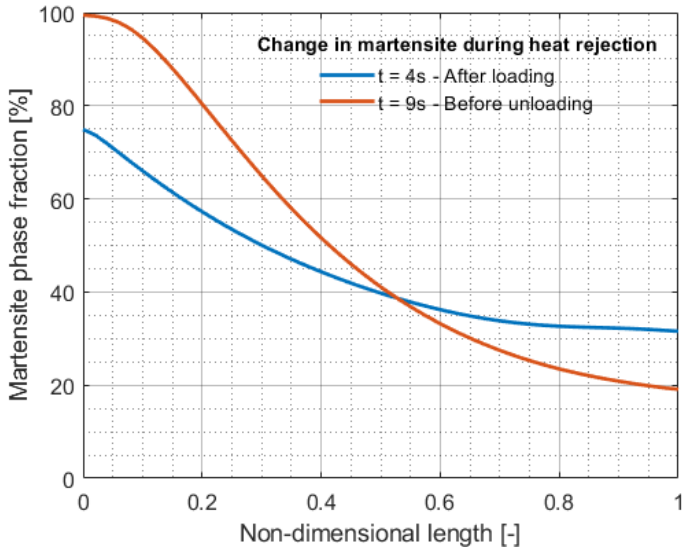

Figure 74: Model prediction for martensitic phase fraction along the regenerator after the loading process finished and after the heat rejection step is finished.

At t = 4s, the beginning of the heat transfer step, immediately after the loading process is finished, the martensite phase fraction at the cold end of the regenerator is 75%, while at the high temperature end of the regenerator is 30%. At t = 9s, the end of the heat transfer step, these differences get worse, with the low temperature end of the regenerator reaching almost 100% while the hot end of the regenerator decreases further to 20%. This is the result of the thermodynamic balance between the phase equilibrium phenomenon, the stress and the temperature.

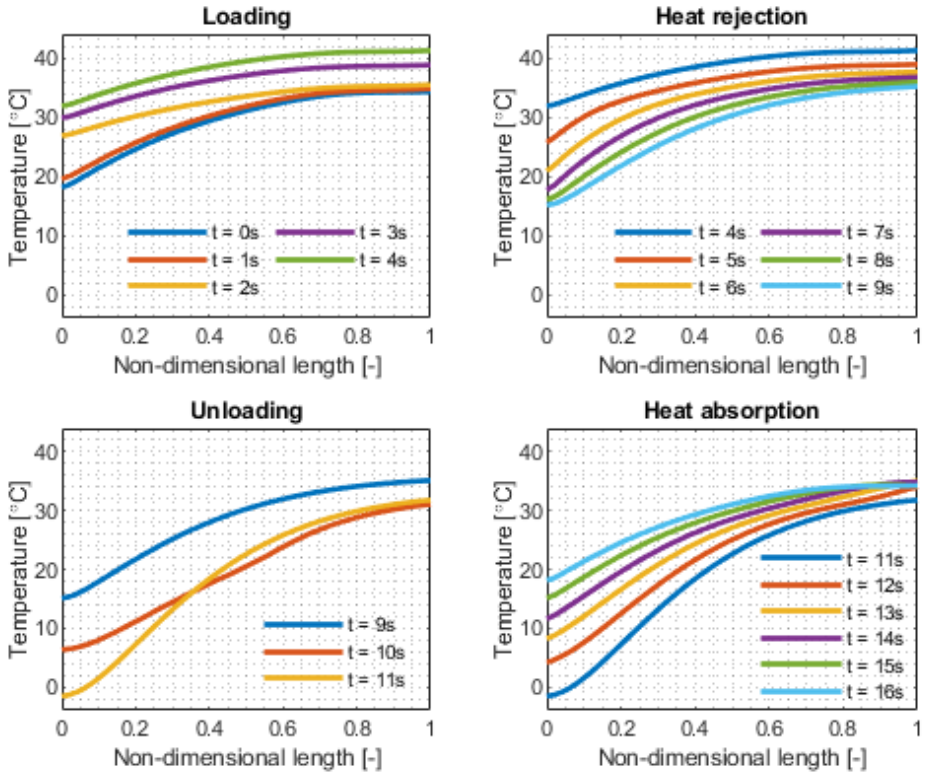

Figure 75: Temperature profile time evolution during a steady-state cycle for a one stage regenerator

Figure 75 shows the temperature profile along the regenerator every 1 second of a complete cycle after reaching the steady state and the temperature gradient has already been established. There is one subplot for each step in the process. A general observation that stems from the all the plots is the nonlinearity of the temperature profile. Some particular observations follow:

1. The “Loading” subplot shows that the adiabatic temperature increase happens first in the cold end of the regenerator, which is consistent with the fact that it deforms at lower stress than the hot end. It also shows that the total temperature increase of the cold side

is approximately 14 K, while the temperature increase in the hot side is approximately 7 K. This is due to the larger strain experienced by the cold side.

2. The "Unloading" subplot shows that the temperature decrease of the cold side is approximately 16 K, and the temperature decrease of the hot side is approximately 4 K. The reason for the difference with respect to the temperature increase is that during the heat transfer step the martensite percentage increases in the cold side and decreases in the hot side with respect to what it was at the end of the loading step. Starting from a larger martensite percentage represents a larger entropy change upon unloading and a larger adiabatic temperature change. Same concept but of different sign can be done for the hot side of the regenerator.
3. Considering the complete cycle, the low temperature end temperature's swing is +14 K / -16 K, while the high temperature end temperature swing is +7 K / -4 K. This shows that the cold end of the regenerator operates close to the material's full potential, while the hot end of the regenerator is far from it. The aggregated performance is close to the one to be expected from the average strain. This is a fundamental problem, because pushing the performance by increasing the average strain is impossible without the cold end of the regenerator reaching its limit prematurely.

3.2 Two-stage regenerator configuration

The strain maldistribution is also present when two, or more regenerators are connected in series. Figure 76 shows the martensite phase fraction along each stage of a two-stage configuration. The mechanical boundary condition is that during the loading stage both

regenerators are loaded simultaneously such that the same total displacement – average strain – is applied to each of them by the hydraulic actuator, and the stress response of each stage is mechanically independent from the other. Each regenerator will experience a stress that is a function of the temperature distribution and the condition that the sum of all the local displacements caused by the local strains add up to the total displacement. The same phenomenon is predicted: the cold side deforms more than the hot side.

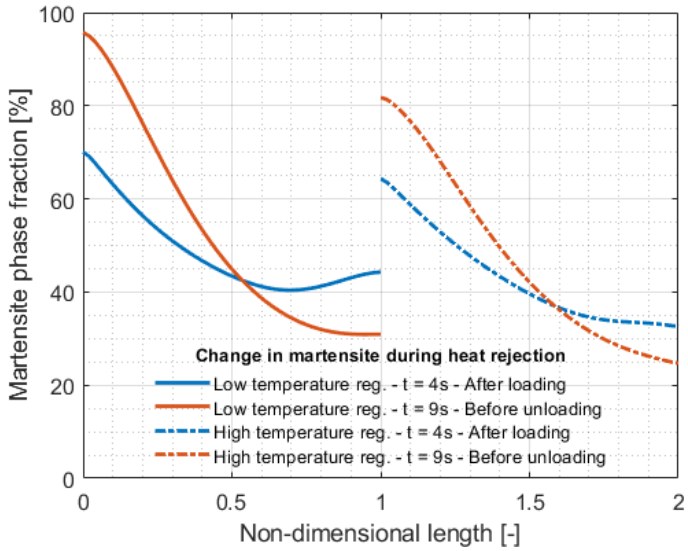

Figure 76: Martensite phase fraction for each stage in a two-stage system configuration after loading and before unloading

The heat transfer fluid thermally connects both stages through convection and advection: during heat rejection water flows from the cold end of the cold regenerator to the hot end of the hot regenerator, and during heat absorption in the opposite direction. The convective and advective heat transfer results in a smooth temperature profile across both regenerators after both heat transfer steps (see t = 0s and t = 9s in Figure 77), but the discontinuity in martensite phase fraction implies a discontinuity in entropy change upon unloading

between the cold end of the hot regenerator and the hot end of the cold regenerator which translates into temperature discontinuities after the unloading step. This is more clearly shown in Figure 77 at t = 9 s and t = 11 s.

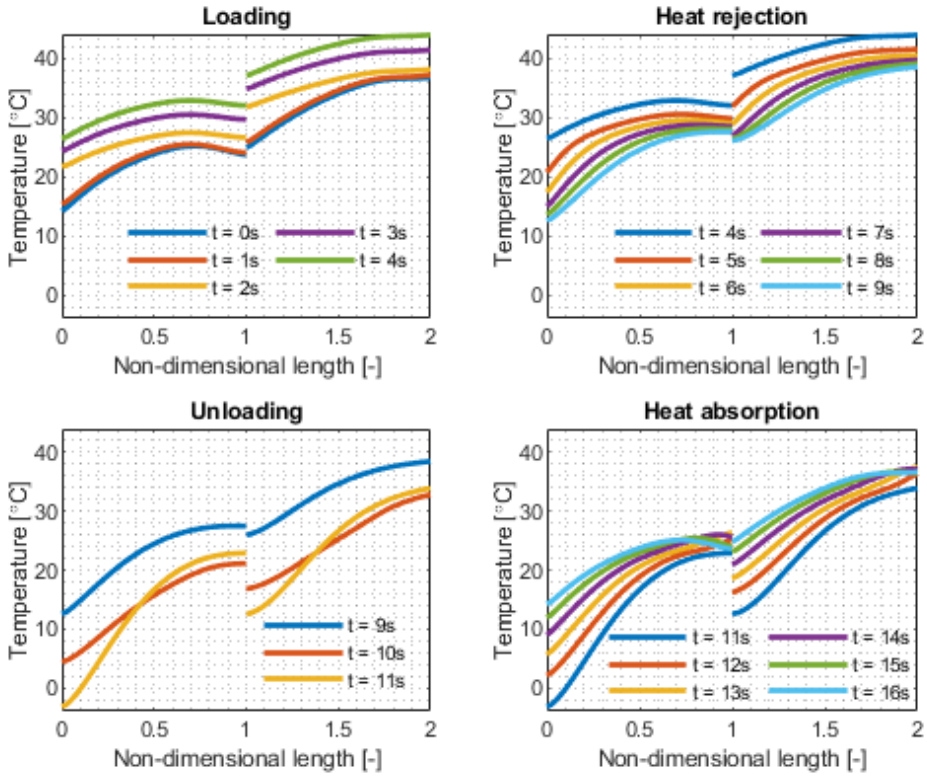

Figure 77: Temperature profile time evolution during a steady-state cycle for a two-stage regenerator

Figure 77 shows the temperature profile along each regenerator every 1 second of a complete cycle after reaching the steady state and the temperature gradient has already been established. There is one subplot for each step in the process. The general observations that applied for the one stage configuration still apply here, but there are a few additional ones:

1. At the end of the loading step there is a small temperature gap between the hot side of the cold regenerator and the cold side of the hot regenerator in the same direction of the temperature gradient. This is due to the fact that their starting temperature is similar, but the cold side of the hot regenerator deforms more than the hot side of the cold regenerator because the stress on the hot regenerator is higher.
2. At the end of the unloading step there is a large temperature gap between the hot side of the cold stage and the cold side of the hot stage in the opposite direction of the gradient. This disrupts the fluid heat rejection process to the solid, because as the fluid moves from one regenerator to the next it encounters a higher temperature and instead of rejecting heat, starts to absorb, reversing the trend.

Chapter 4: Reciprocating configuration

4.1 Reciprocating configuration

Another alternative to connecting two regenerators in series is to connect them in parallel, but in a reciprocating configuration, alternatively rejecting heat to the sink or absorbing heat from the reservoir. This configuration allows for work recovery and the general expectation is to double the cooling capacity, not necessarily improving the temperature lift. The general approach for this set of experiments was different than the previous: the model was used to predict the performance of this new arrangement, later it was determined how it could be realized experimentally with our current tooling and finally test the predictions experimentally.

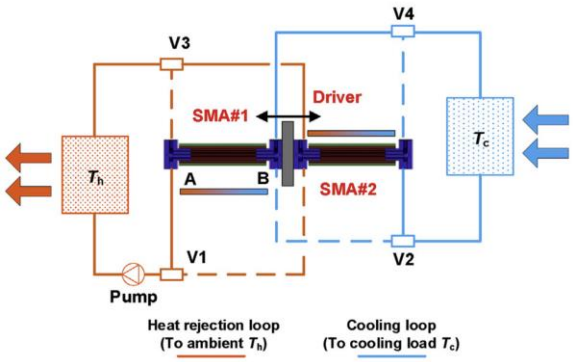

Figure 78: Schematic of reciprocating configuration (Qian et al., 2017)

Figure 78 shows a schematic of the operating steps of a full cycle of two regenerators operating in reciprocation. This is an application of the concept presented by Qian (Qian

et al., 2017) and a configuration called AM2R used in magnetocaloric systems as well (Kitanovski et al., 2015).

The hot side of each regenerator is directly connected to the heat sink through two tube segments, one that feeds heat transfer fluid to the sink while that regenerator is in heat rejection, and another one that receives heat transfer fluid from the sink during heat absorption. Analogously, the cold side of each regenerator is directly connected to the heat reservoir through two tube segments, one that feeds heat transfer fluid to the reservoir while that regenerator is in heat absorption and another one that receives heat transfer fluid from the reservoir while that regenerator is in heat rejection. The flow of heat transfer fluid through the loop is controlled by solenoid valves that turn on and off accordingly.

4.2 Numerical simulation predictions

Figure 79 shows the temperature lift prediction as a function of utilization factor for the reciprocating configuration and compared to the previously studied one stage and two-stage configurations. The model results show that the reciprocating configuration is superior to the one stage configuration and matches the maximum temperature lift of the two-stage configuration. First lets analyze the performance improvement with respect to the one stage configuration. Figure 49 shows the heat transfer loop schematic for the one stage configuration. During operation, tube segment T2 receives hot fluid from the sink during heat rejection, and cold fluid from the reservoir during heat absorption. If designed as a heat exchanger it could serve the function of a passive regenerator with its own hot

blow period during the cold blow period in the Ni-Ti regenerator, and vice versa. In this reciprocating configuration, the role of T2 is actually served by another Ni-Ti regenerator, an active regenerator.

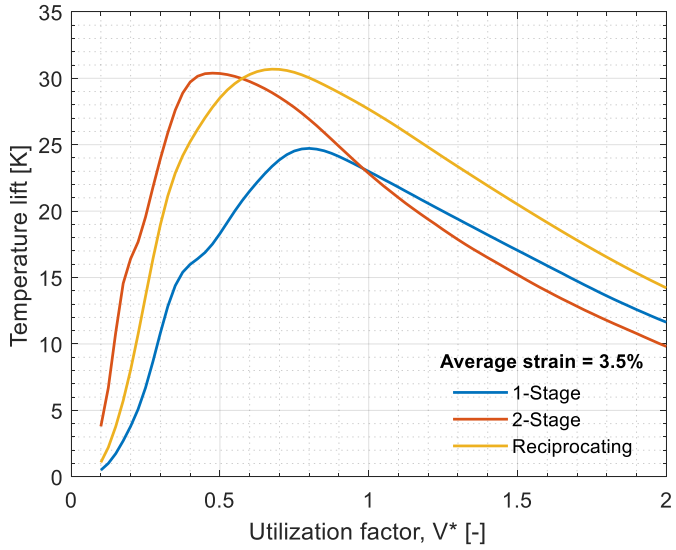

Figure 79: Temperature lift as a function of utilization factor for three system configurations

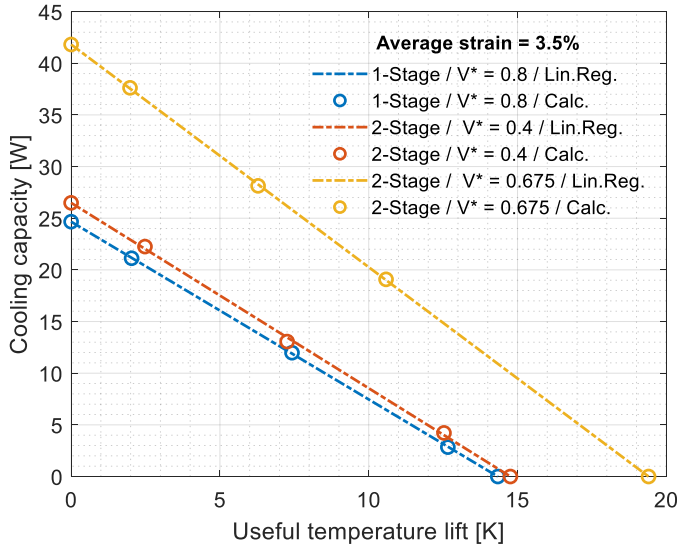

Figure 80: Cooling capacity and useful temperature lift for three system configurations

Figure 80 shows the cooling capacity and useful temperature lift for all three configurations. The reciprocating configuration offers a superior performance to both the one stage and two-stage configurations.

4.3 Experimental set-up and main results

Figure 81 shows a schematic how this configuration was realized with the use of our available tooling and materials.

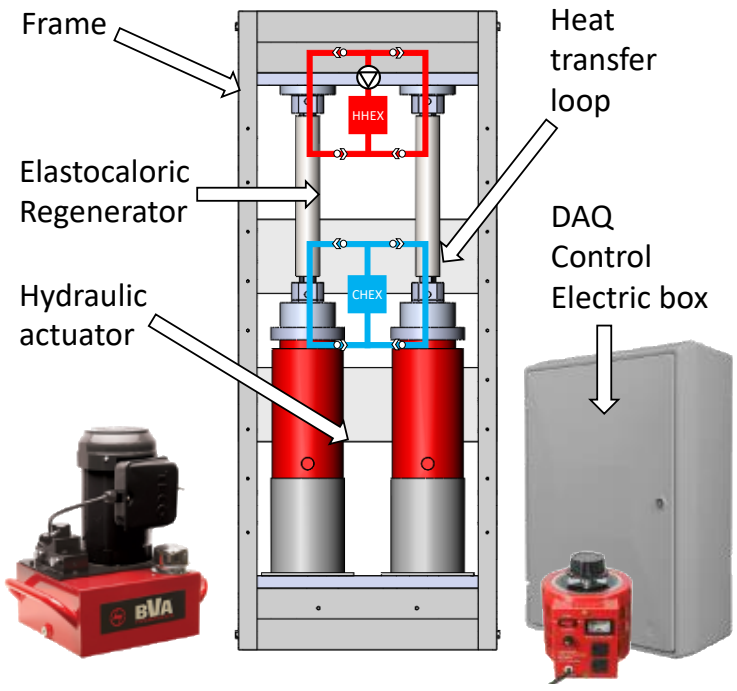

Figure 81: Experimental set up for a reciprocating arrangement of two Ni-Ti regenerators

The Ni-Ti heat exchangers were set up next to each other to minimize the length of connecting tubing. A second hydraulic actuator was added next to the first one, auxiliary

parts machined to ensure precise fit and alignment, and the heat transfer loop was modified accordingly. The hydraulic valves configuration did not have to be modified to allow the system's reciprocating operation.

Figure 82 shows the water loop connections for the maximum temperature lift test, without the heat sink and the heat reservoir. All of the connecting tube sections experience flow in a single direction, except the regenerators. The flow is directed by opening and closing the appropriate solenoid valves, and in this case the heat transfer fluid pump only needs to operate in one direction. The cycle steps are the same, but each regenerator is out of phase with the other by half a cycle. First, the regenerator #1 is loaded, while regenerator #2 is unloaded. These two actions take place adiabatically. Second, heat transfer fluid moves from the hot end of regenerator #1 to the hot end of regenerator #2 by opening SV1 and SV2 and from the cold end of the regenerator #2 to the cold end of regenerator #1 by opening SV3 and SV4. Third, regenerator #1 is unloaded while regenerator #2 is loaded. These two actions take place adiabatically. Fourth, heat transfer fluid goes from the hot end of regenerator #2 to the hot end of regenerator #1 by opening SV5 and SV6, and from the cold end of regenerator #1 to the cold end of regenerator #2 by opening SV7 and SV8.

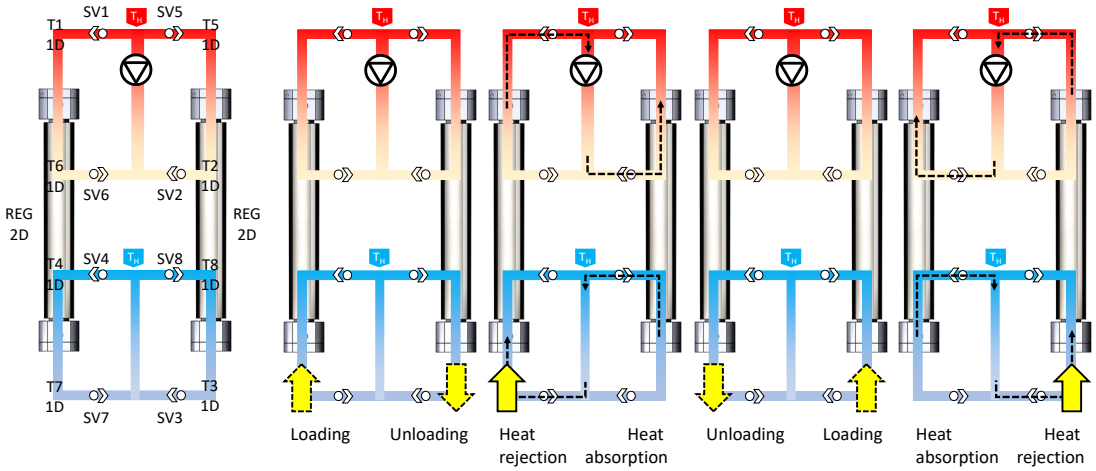

Figure 82: Experimental configuration and test procedure schematic for two regenerators in reciprocating arrangement

Table 7 shows the parameters used for the relevant tests done with this configuration

Table 7: Operating parameters for tests TL-4, TL-5, TL-6, CC-6, CC-7 and CC-8

Parameter [unit]	TL-4	TL-5	TL-6	CC-6	CC-7	CC-8
Load. /Unload. time [s]	2	3.5	4.1	2	3	4
Heat rej./abs. time [s]	4	4	4	4	4	4
Unload. / load. time [s]	2	3.5	4.1	2	3	4
Heat abs. / rej. time [s]	4	4	4	4	4	4
Strain [%]	2	3	3.5	2	3	3.5
Utilization factor [-]	0.57	0.57	0.57	0.57	0.65	0.65
Cooling capacity [W]	-	-	-	Various	Various	Various

Figure 83 shows the time evolution of T_H and T_C during the first 40 minutes of the tests TL-4, TL-5 and TL-6.

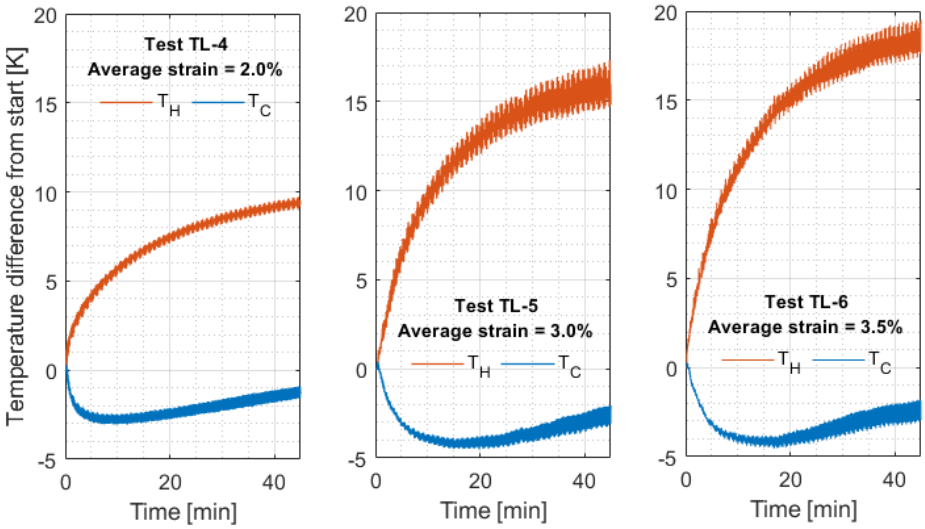

Figure 83: T_H and T_C time evolution for an average strain of 2% and 3%

During the first 10 to 15 minutes of the test T_H increases and T_C decreases as the temperature difference between them increases. Beyond the first 10 to 15 minutes, both temperatures start to increase and the temperature lift between them as well. This behavior is the same for both tests. The temperature lift measured for an average strain of 3.5% is larger than the one measured for 3.0% strain, and larger to the one measured for 2.0% strain.

Figure 84 shows the time evolution of the temperature lift. For an average strain of 2% the maximum temperature lift after 45 minutes was 10.8 K, while for an average strain of 3% the maximum temperature lift after 60 minutes was of 18.5 K and for an average strain of 3.5% was 20.1 K.

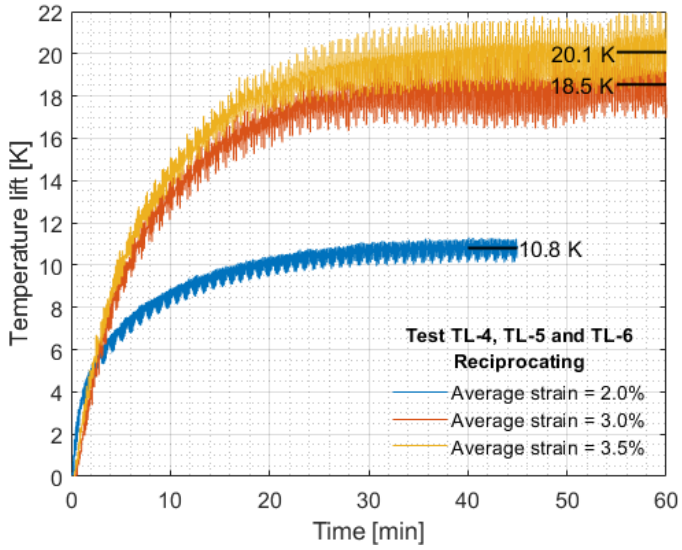

Figure 84: Temperature lift in closed-loop regeneration for 2%, 3% and 3.5% strain in reciprocating configuration

Figure 85 shows the model prediction for the different strain levels, and the measurements that were obtained. The difference between the model prediction and the experimental measurement increased with strain, while for an average strain of 2% the difference between the predicted maximum temperature lift and the measured was approximately 10%, for 3.0% was closer to 25% and for 3.5% it was approximately 33%. Despite these differences, the value of 20.1K is larger than that measured for the one stage configuration for the same strain, which shows that the reciprocating configuration is effectively superior. It has not been concluded whether the difference is performance degradation during experiment, overprediction by the model or a combination of both. More efforts will be required to answer this conclusively.

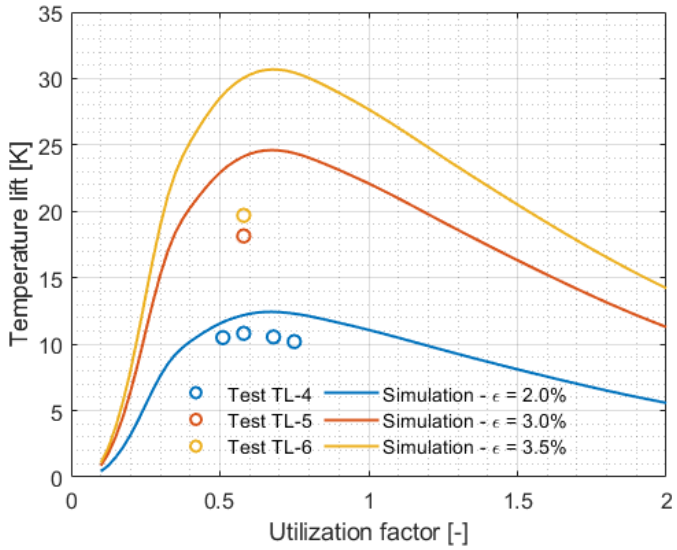

Figure 85: Predicted temperature lift and experimental results as a function of utilization factor

Figure 86 shows the experimental set up for the cooling capacity measurement. Analogously to what was done for the previous configurations, the tube segments T1 and T3 were disconnected to reject the hot water coming out of the regenerators, and the tube segments T6 and T2 were fed water at room temperature from a reservoir. To simulate the different cooling loads, a variable voltage source connected to an electric resistance was operated at different voltages and the useful temperature lift after 45 – 60 minutes was recorded for each cooling load.

Figure 87 shows the time evolution of the useful temperature lift as different cooling loads are used during operation. This is a slightly different test procedure that allowed to obtain the data in a single test run, instead multiple different individual tests.

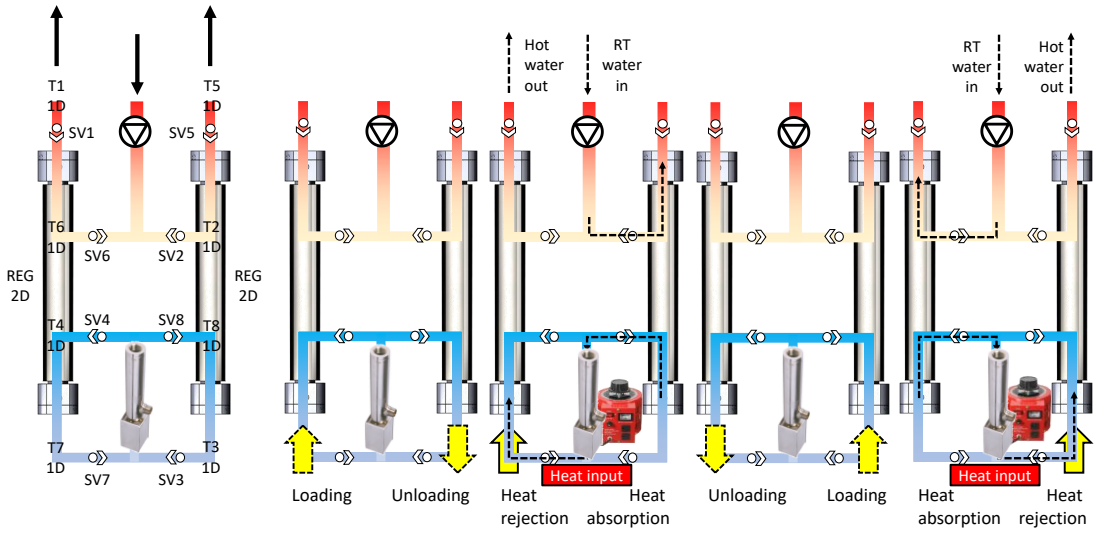

Figure 86: Cooling capacity test set up and sequence schematic for a reciprocating

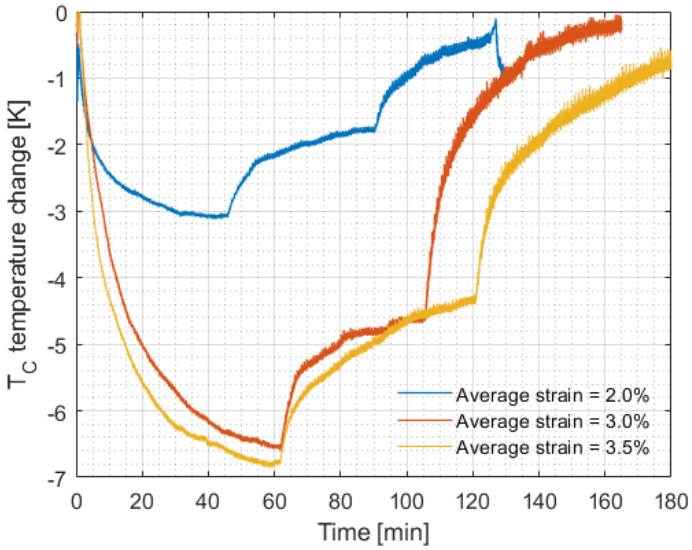

Figure 87: Time evolution of useful temperature lift for three average strains

Figure 88 shows the cooling capacity measurements as a function of the useful temperature lift. The cooling performance of the reciprocating system at an average of 3% strain is slightly superior to the one stage configuration at 3.5% strain which is an indication that it

is a better arrangement. The maximum cooling capacity extrapolated from the data measured in the two-stage configuration is higher to what was measured in this test, however it is worth mentioning that the flow rate in that test was higher and promoted a higher cooling capacity.

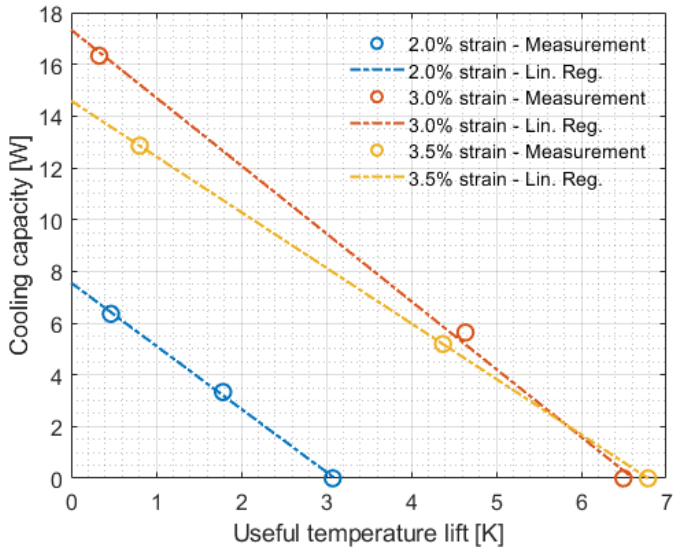

Figure 88: Cooling capacity measurements for the reciprocating configuration for average strain of 2%, 3% and 3.5%.

Figure 89 shows infrared photographs of the tubing connected to the hot side of the regenerators and the one connected to the cold side of the regenerators after operating for 60 minutes during the maximum temperature lift test.

The images show that the temperature of the tubing connected to the hot side of the regenerators is significantly higher than room temperature which indicates that there is the potential for heat loss by natural convection. The temperature of the tubing connected to the cold side of the regenerators is lower than surroundings, but the difference is not as

large as in the hot side, so the potential for heat loss is not as large, particularly in the maximum temperature lift test. This situation could be reversed for cooling capacity test, where the temperature of the cold side is purposely decreased with respect to room temperature.

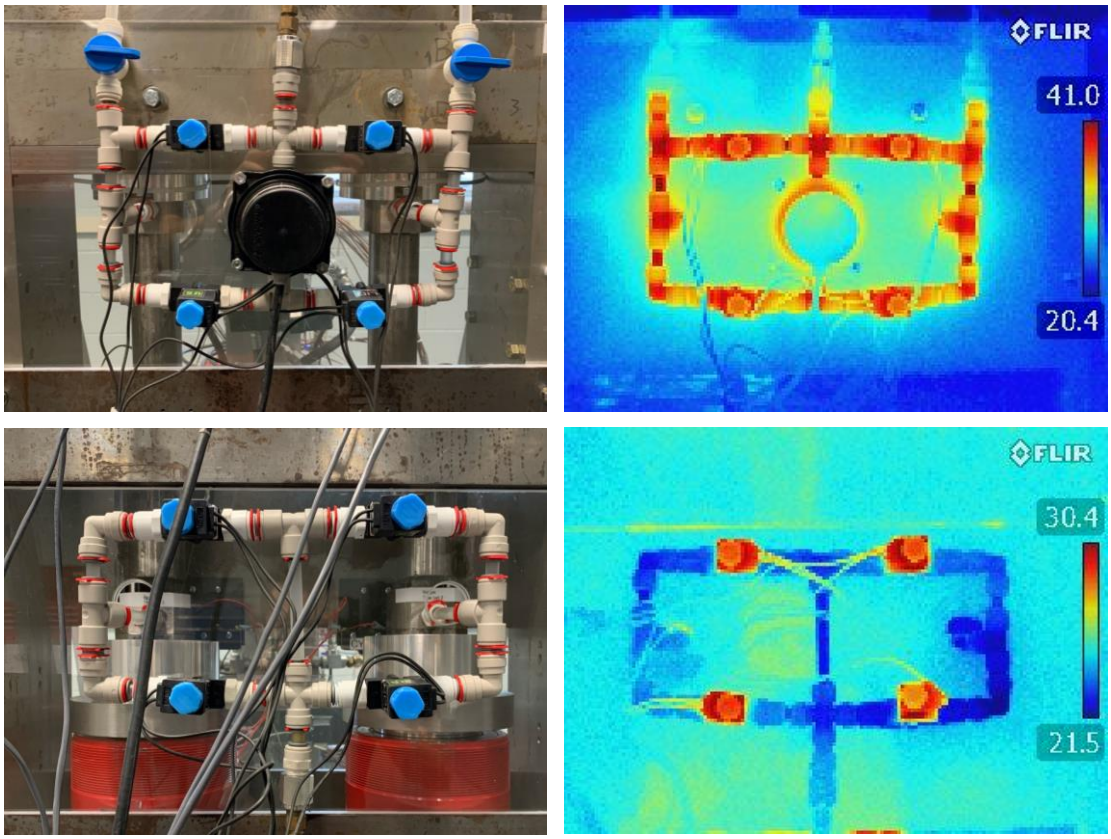

Figure 89: Infrared photography of cold side heat transfer loop

Another observation is that it does not seem that there is a significant heat transfer from the solenoid valve coil to the fluid, the heat rejection appears to be restricted to the coil region.

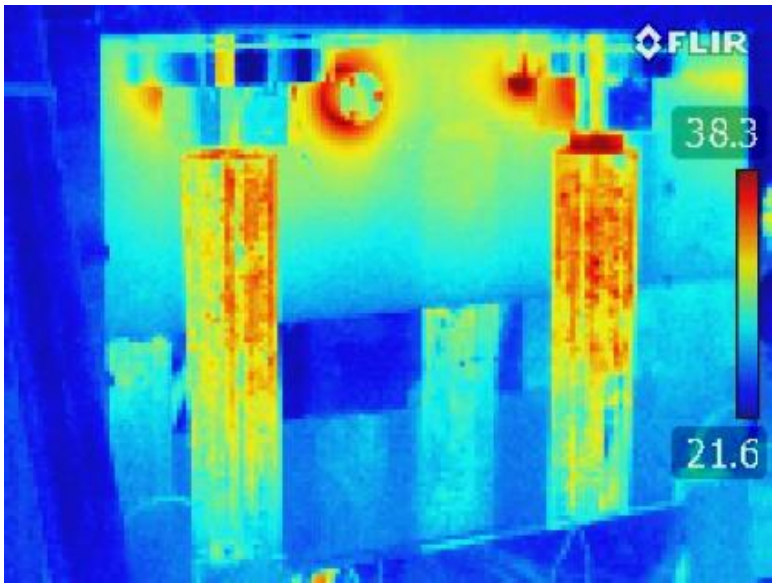

Figure 90: Infrared photography of regenerators.

Figure 90 shows an infrared image of the regenerators. It shows the temperature gradient through the tube holder, and it also shows that there is heat transfer to the neck of the loading head. The heat from the Ni-Ti tubes is transferred through the stainless steel tubes to the tube holder. The contact area between these parts, which ideally is supposed to be a contact line, in reality is a contact surface. Figure 41 showed that as the stainless steel is deformed, the contact area is larger. Since this is something that cannot be avoided the tube holders need to be insulated to prevent heat loss, particularly important in a system with a low cooling capacity as the one tested in this work. This can also be one of the factors that makes the differences between prediction and experiment to increase as the strain increases.

Chapter 5: Summary of main experimental results

The objectives for this chapter are the following:

1. Consolidate the test results and determine which system integration configuration offers the best performance.
2. Quantify the progress made with respect to magnetocaloric system performance.

Figure 91 shows the maximum temperature lift measured from all configurations. The temperature lift measurements obtained with the configurations that use the Ni-Ti heat exchanger as a regenerator are all superior to the one that does not.

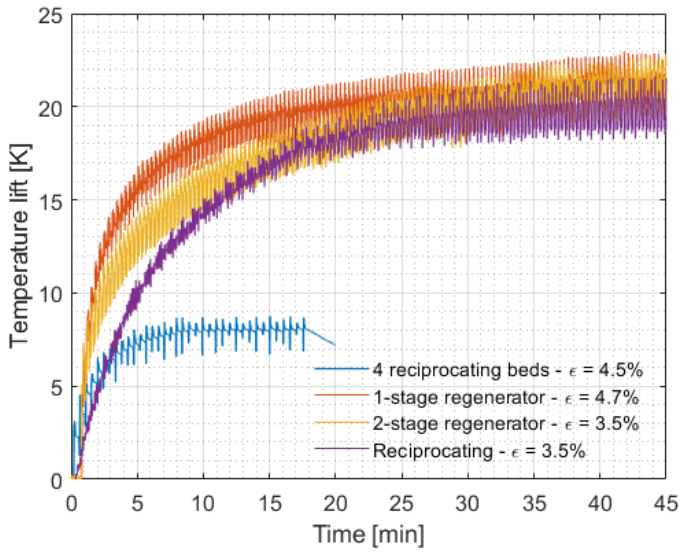

Figure 91: Comparison of maximum temperature lift measurements for all configurations

Comparing all three options with the Ni-Ti regenerator, the largest value was obtained with the two-stage configuration with an average strain of 3.5%. The difference is small with respect to the 2 reciprocating regenerators configuration which were also tested to an average strain of 3.5%. The strain level that is required from a one stage configuration in order to match that number is 4.7%, which is significantly higher.

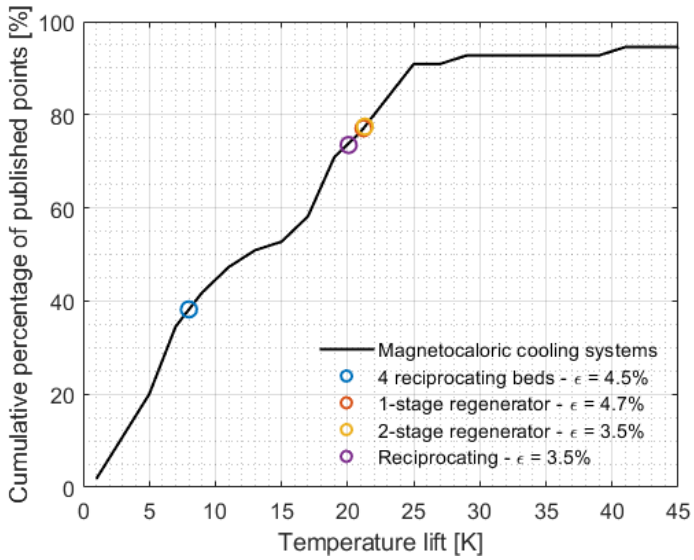

Figure 92: Progress made in comparison to surveyed magnetocaloric cooling systems

In comparison to magnetocaloric cooling systems, the first configuration was close to surpassing the performance of 40% of the surveyed data, while with the active regeneration cycle this number rose to 80%. This is a significant improvement in the effort to surpass what has been done. In order to reach the value of 25 K, an increase in strain could be enough, and strategies to go beyond that will be discussed in the next chapter.

Figure 93 shows the cooling capacity performance of all configurations. From the point of view of maximum useful temperature lift, the configurations that used the Ni-Ti heat

exchanger as a regenerator produced larger numbers than the one without. However, the maximum cooling capacity and the area under the cooling capacity-useful temperature lift curve is significantly smaller. However, this can be overcome by an increase in strain, or by adding more Ni-Ti regenerators.

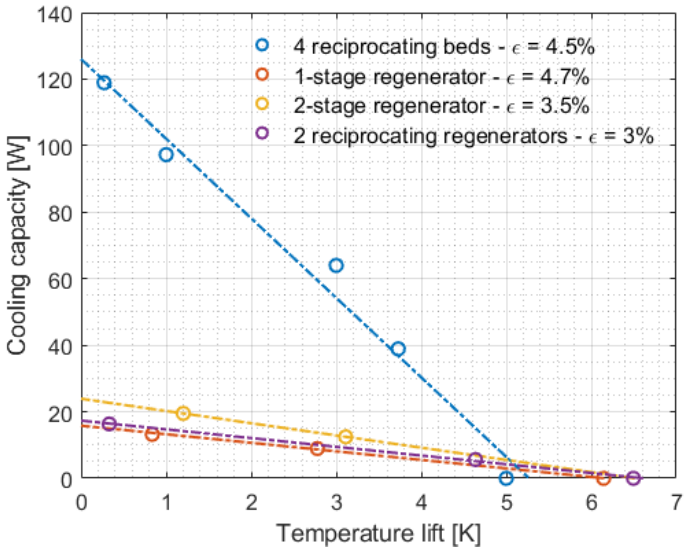

Figure 93: Cooling capacity and temperature lift performance of all configurations

Figure 94 shows the progress made in comparison to surveyed magnetocaloric cooling systems. Because of the limited maximum cooling capacity that was achieved with the active regeneration configurations, there was a regression in comparison to the performance achived by magnetocaloric cooling devices. However, there is room for improvement.

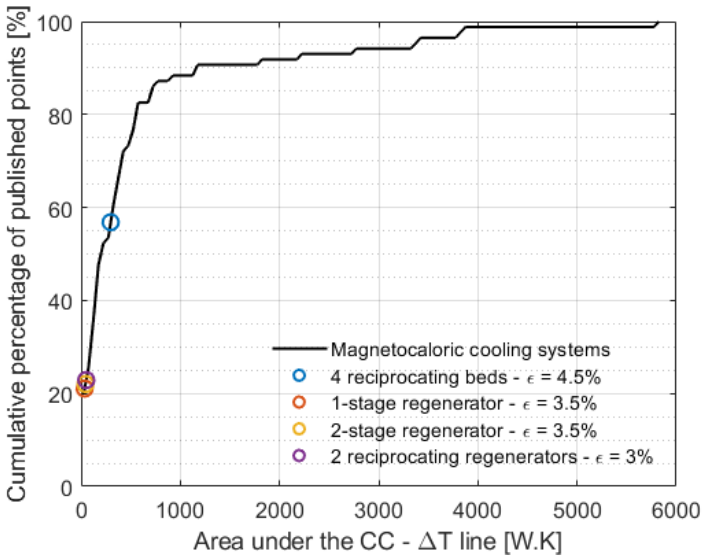

Figure 94: Progress made in comparison to surveyed magnetocaloric cooling systems

Chapter 6: Engineering design improvement considerations

6.1 Regenerator thermal performance

In the baseline configuration a plastic triangular insert is used to improve the heat transfer performance. A pathway to further improvement is to increase the cross-section blockage. Figure 95 shows the effect of using an insert with a square, a pentagon or hexagon cross section and compared to the baseline.

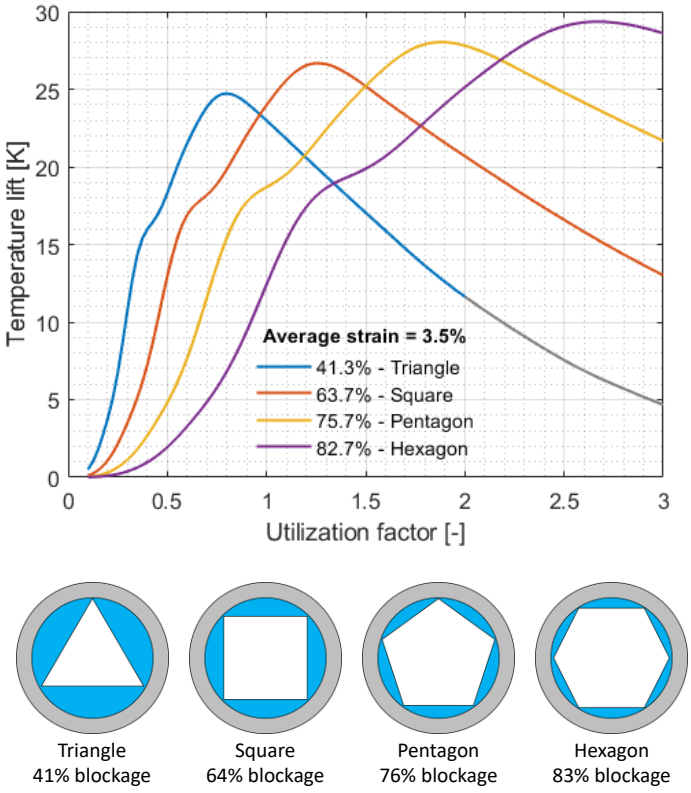

Figure 95: Temperature lift for different inscribed polygonal inserts

As the cross-section blockage increases, the mass of heat transfer fluid inside the regenerator decreases so the peak in the curve shifts towards larger utilization factor values. The temperature lift value at the peak is higher as the blockage increases, however the improvement is not significant. Figure 96 shows the effect of using thin-wall stainless steel tubes instead of solid cross-section plastic inserts.

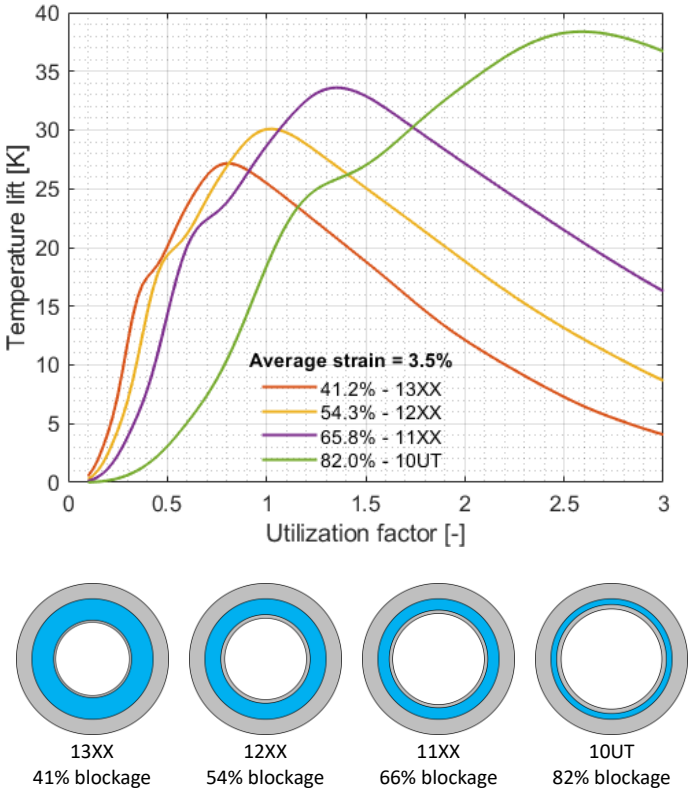

Figure 96: Temperature lift for different thin wall stainless steel inserts

The identification of the tubes as 13XX, 12XX, 11XX and 10UT refers to the commercial denomination and corresponds to specific tube dimensions (OD, ID).

Increasing the blockage by adding sides to the inscribed polygon also increases the mass of the insert, while in the case of the thin wall stainless steel tube the internal volume of

the tube is filled with air. It is important to analyze how the thermal mass of the Ni-Ti tube, the water and the insert relate to one another as the cross-section blockage changes. Equation 31 shows the definition of the non-dimensional number κ which establishes the relationship between the thermal masses. Analyzing a few extreme situations are useful to understand the physical meaning of κ. When κ = 1 it means that the thermal mass of the insert and the water inside the regenerator are insignificant with respect to the thermal mass of the regenerator. When the blockage percentage equals to 0, Figure 97 shows that κ is approximately 3.5, which indicates that the thermal mass of the water inside the regenerator is 2.5 times larger than the thermal mass of the regenerator itself. As the blockage percentage increases, a fraction of that water is replaced by the insert, either plastic or thin-wall stainless steel, and so the thermal mass inside the regenerator will have two contributions and the final value will depend on the specific geometry.

$$\kappa = \frac{\left(X^{sec}\rho c_p\right)_{Ni-Ti} + \left(X^{sec}\rho c_p\right)_{Fluid} + \left(X^{sec}\rho c_p\right)_{Insert}}{\left(X^{sec}\rho c_p\right)_{Ni-Ti}} \qquad \text{Equation 31}$$

Figure 97 shows the non-dimensional number κ for different combinations of insert geometries. The points in the thin wall hollow stainless-steel inserts series show the values calculated with the standard dimensions for hypodermic tubing products obtained from manufacturers, while the points in the solid plastic inserts series show the changes in κ as the number of sides (n = 3 to 8) in the inscribed polygon increases.

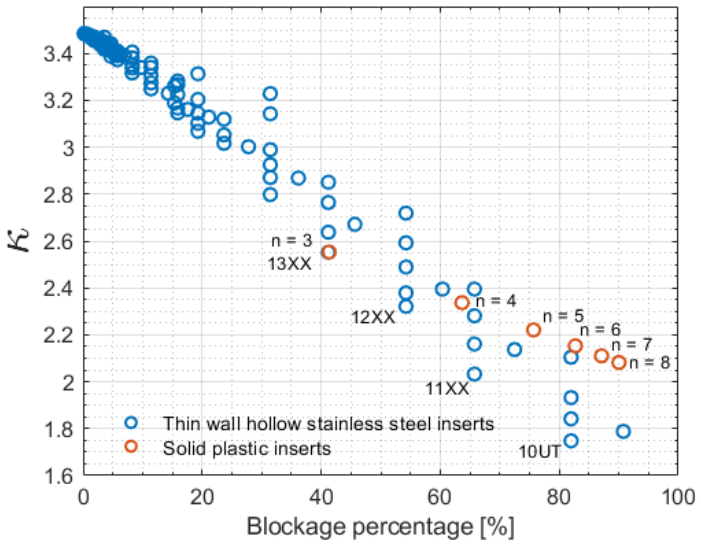

Figure 97: Thermal mass ratio k as a function of blockage percentage for different types of inserts

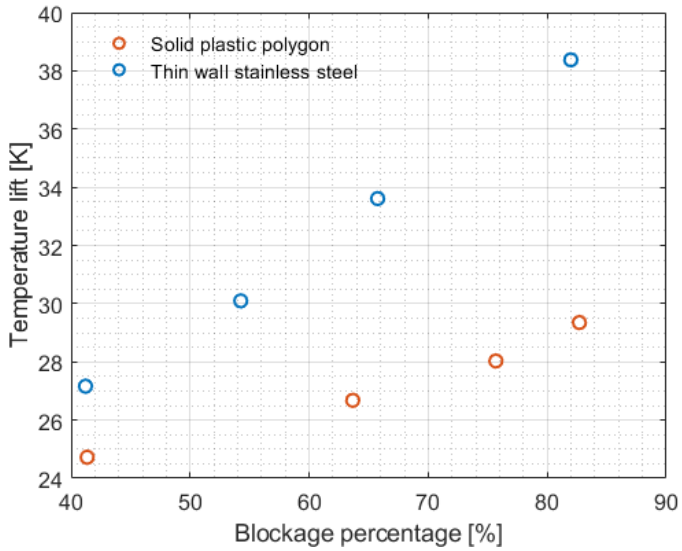

Figure 98: Maximum temperature lift trend calculated for specific insert geometries

Each series has a general trend and they show that as the blockage percentage increases, κ decreases. The number κ decreases faster when inserts are made out of hollow thin wall stainless steel tubes rather than solid plastic inserts. The selected products for analysis

(13XX, 12XX, 11XX and 10UT) were chosen because they were the ones with the thinnest wall thickness and increasing external diameters. They are shown in Figure 97 as the ones with lowest k values and a blockage percentage similar to the polygon. Figure 98 shows the maximum temperature lift for each of these selected options. Thin wall stainless steel inserts are better alternative than solid plastic polygon shape.

Figure 99 shows the effectiveness, NTU_0 and C_r^* as a function of the utilization factor. With the numerical model developed in the previous chapter it was possible to determine the value of utilization factor that would give each configuration the largest temperature lift. Both NTU_0 and C_r^* are a function of the mass flow rate (and thus of the utilization factor since the cycle time is kept constant), and so is the effectiveness. The general trend is that as the cross-section blockage increases, the effectiveness increases. In particular, the circles show the ε, NTU_0 and C_r^* values specified at the utilization factor that gives the temperature lift peak. The increase in temperature lift as the cross-section blockage increases corresponds with an increase in effectiveness. From the values of NTU_0 and C_r^* it is clear that this increase is mostly driven by an increase in NTU_0, because at each operating point, the value of C_r^* remains practically constant and close to 1. Since the heat transfer area is constant, since the mass flow rate at each peak is essentially the same, and since the heat capacity of the fluid is constant (a fair assumption over a limited temperature span that this regenerator would operate) the driver for this increase in NTU_0 is an increase of the heat transfer coefficient as the cross-section blockage increases.

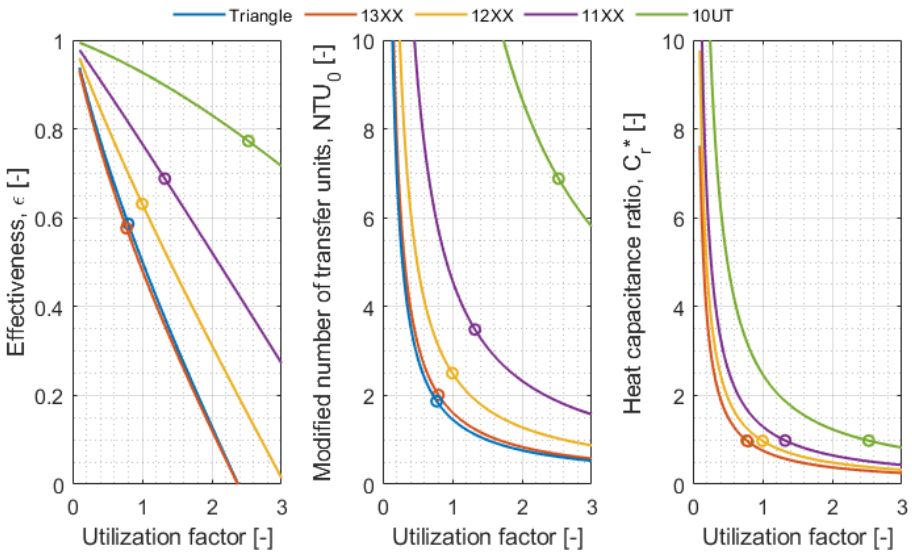

Figure 99: Effectiveness, NTU_0 and C_r* as a function of utilization factor

Table 8: Heat transfer non-dimensional numbers for each configuration

	Cross-section blockage	V* at peak	D_h	ε	NTU_0	C_r*	Re_D	Nu_D	h
Units	[%]	[-]	[mm]	[–]	[-]	[-]	[-]	[-]	[$Wm^{-1}K^{-1}$]
Triangle	41	0.800	1.206	0.587	2.013	0.955	63.84	3.786	1856
13XX	41	0.775	1.345	0.577	1.871	0.984	68.95	3.811	1675
12XX	54	1.000	0.989	0.632	2.506	0.980	65.44	3.767	2252
11XX	66	1.325	0.710	0.689	3.491	0.988	62.23	3.734	3111
10UT	82	2.525	0.354	0.774	6.919	0.987	59.19	3.696	6171

Table 8 shows that the increase in heat transfer coefficient is driven by the decrease in hydraulic diameter, according to Equation 29, since the variation in Nu_D for each condition is not significant.

It is possible to go further in analyzing this result by pointing out an important difference between an active and a passive regenerator. The active regenerator acts as a distributed heat source or heat sink when the phase transition is induced. If the transition is induced

adiabatically, then the change in entropy will translate into a temperature increase or decrease. However, it is not possible to induce this transition adiabatically when there is fluid and an insert inside the regenerator. This was pointed out in literature in the thermodynamic analysis of an idealized active magnetocaloric regenerator (Andrew Rowe, 2012). To further cement this concept, it is useful to compare the temperature change in solid and fluid during the loading and unloading steps, for the hexagonal plastic insert and the 10UT stainless-steel insert since both have a similar blockage percentage, but the κ of the plastic insert is higher than the one of the stainless-steel inserts. Figure 100 shows the temperature change after loading along the regenerator for the solid and the fluid, and Figure 101 the same type of plot except that it refers to the unloading process. The temperature change is not homogeneous along the regenerator because of the strain maldistribution previously addressed and that is why the data is plotted as a function of location.

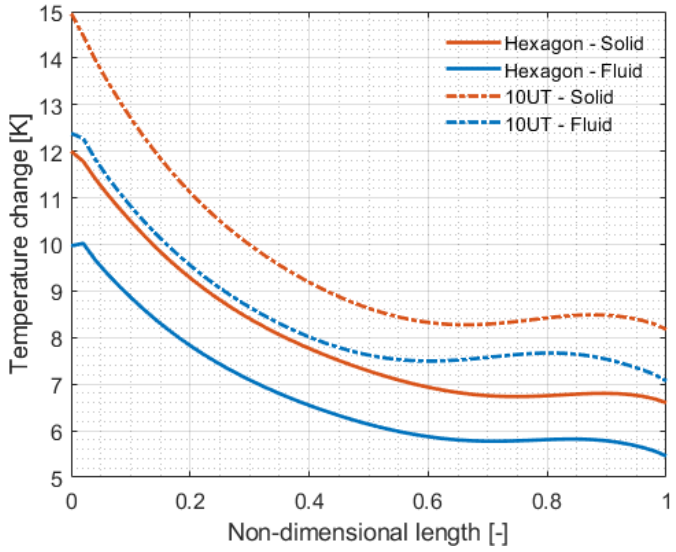

Figure 100: Solid and fluid temperature change during forward transformation along the regenerator

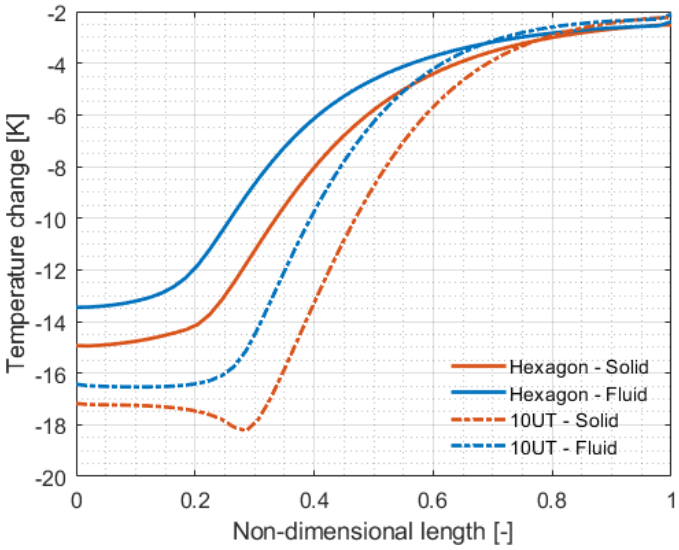

Figure 101: Solid and fluid temperature change during reverse transformation along the regenerator

Because the total amount of transformation heat is the same in both cases, proportional to the average strain, decreasing the amount of parasitic thermal mass allows the Ni-Ti to experience a larger “adiabatic” temperature increase and decrease, which helps develop a larger temperature lift. The current design is constrained by Ni-Ti tubes with fixed dimensions, so using an insert is a strategy to manage the ratio between thermal masses within this constraint. However, in future designs, this should be taken into consideration early to avoid the use of inserts. If the flow cross section could be designed without restrictions, Figure 102 shows as an example a channel elliptical cross section, with equivalent flow area and equivalent hydraulic diameter as the tube with the triangular insert. As a result, the heat transfer area is increased by almost 50%, with the benefits of not having dead thermal mass inside the channel, and no additional pressure drop.

Figure 102: Cross sections of equivalent flow area and hydraulic diameter, but the first with a triangular insert, the second without insert

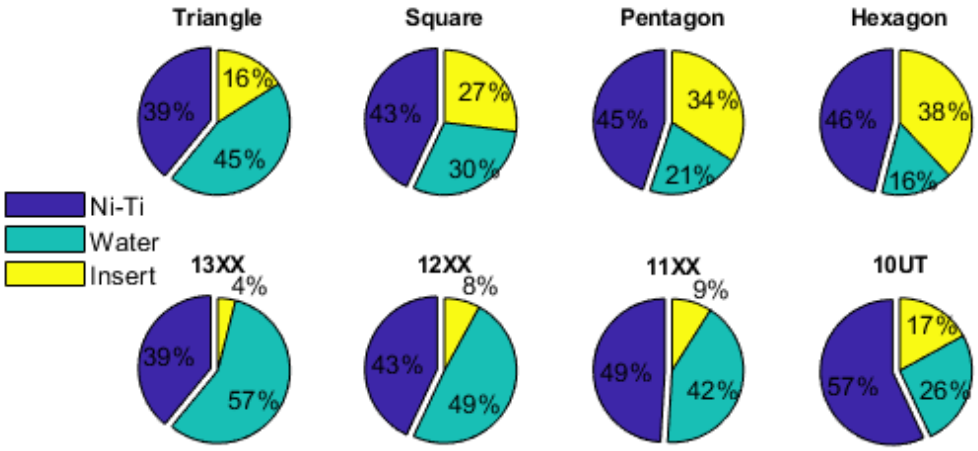

Figure 103: Thermal mass fraction between regenerator, fluid and insert for different insert geometries and materials

Figure 103 shows how the thermal mass of Ni-Ti, water and insert contribute to the value of κ. It is particularly interesting to see the split between the thermal mass of insert and fluid, the parasitic thermal mass. It is clear by looking at these pie charts the differences between each approach, better performing configurations have a large Ni-Ti thermal mass

percentage (k closer to 1) but also the split between the parasitic thermal masses favors the water and not the insert.

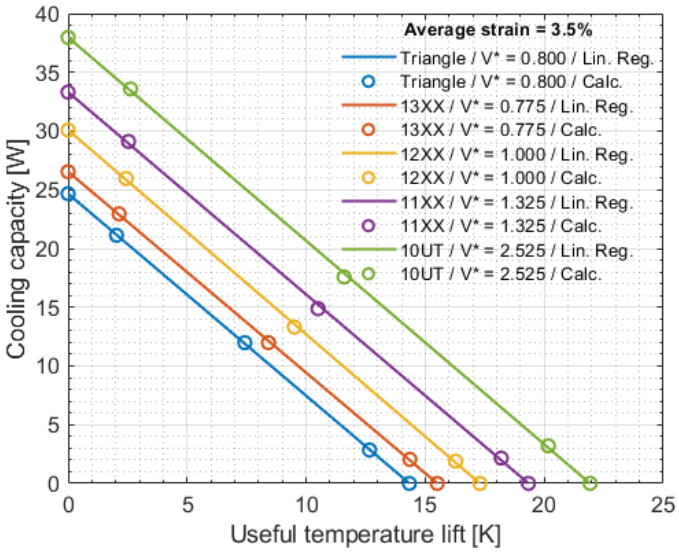

Figure 104: Cooling capacity performance for different thin wall stainless steel tubes

Figure 104 shows the cooling capacity as a function of useful temperature lift for the stainless-steel hollow tube inserts. As the blockage percentage increases, k decreases and both useful temperature lift and cooling capacity improve. This fact makes it a very effective strategy; however, it has to be considered that as the blockage increases so does the pressure drop across the regenerator. For an annular flow channel, the pressure drop is calculated with Equation 32:

$$\Delta P = 2f\left(\frac{L}{D_h}\right)\rho v^2 \qquad \text{Equation 32}$$

While f is defined in Equation 33

$$f = \frac{C}{Re}$$ Equation 33

The value of C depends on the ratio between the OD of the Ni-Ti tube and the OD of the stainless steel insert. Table 9 shows the pressure drop along a single tube and how much is affected by the blockage of the cross section. Taking as a reference the pressure drop using a 13XX with a 41% blockage, the pressure drop increases 2.4X by using a 12XX with a 54% blockage, 6.1X by using an 11XX with a 66% blockage and 47X by using an 10UT with a 82% blockage. This last option seems to be out of the experimental capabilities due to the significant pumping power that would be required. Options 12XX and 11XX could offer the best chance of success.

Table 9: Main numbers used to calculate the pressure drop along a single Ni-Ti tube with a stainless steel insert

	OD_{Ni-Ti}/OD_{SS}	C	Re	f	D_h	V	ΔP
Tube	[-]	[-]	[-]	[-]	[m]	[m s^{-1}]	[Pa]
13XX	1.557	23.92	68.95	0.34	0.00135	0.0077	7.7
12XX	1.357	23.96	65.44	0.36	0.00099	0.0099	18.4
11XX	1.233	23.98	62.23	0.38	0.00071	0.0131	47.3
10UT	1.104	23.99	59.19	0.40	0.00035	0.025	363.5

6.2 Regenerator length

The length of the regenerator is an important variable to take into consideration because it affects two important characteristics: buckling behavior and local strain distribution. Both of these are related to the likelihood of failure of the regenerator and essentially determine what is the maximum average strain that can be achieved during operation. In the baseline configuration presented and tested in the previous chapters it appears that both phenomena could be coupled. Critical buckling load is inversely proportional to the square of the length, so in principle it should be possible to double the critical buckling load by scaling down the length by a factor of $\sqrt{2}$ and to quadruple it by scaling down by a factor of 2. Figure 105 shows the temperature lift as a function of utilization factor for regenerators of three different lengths. As the length of the regenerator decreases, the maximum temperature lift that can be obtained decreases and it shifts towards larger values of utilization factor. One of the conditions to do this comparison is to maintain all tooling and connecting tubing the same, the only variable that changed is the length of the regenerator. The reason why the utilization factor for the peak temperature lift shifts towards higher values is that a larger fraction of the volume of the regenerator is required to evacuate the same volume of fluid from the loading heads. However, the regenerator effectiveness is higher for lower utilization factors, so shortening the regenerator results in a lower temperature lift.

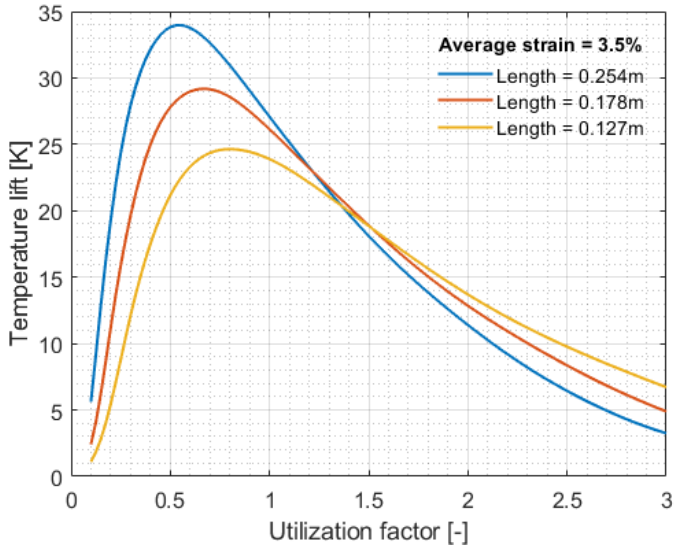

Figure 105: Temperature lift as a function of utilization factor for different lengths

Figure 106 shows the maximum temperature lift that can be obtained for these regenerators, but for various, larger strains. In principle it is possible to compensate for the temperature lift degradation caused by shortening the length, by increasing the strain. The same temperature lift that can be achieved at 3.5% strain in a 0.254 m-long regenerator can be achieved at 3.9% strain in a 0.178 m-long regenerator and at 4.4% strain in a 0.127 m-long regenerator. Since shorter regenerators are more resistant to buckling, increasing strain can be a potential solution as long that the required load to induce the additional strain does not scale up in the same proportion as the critical buckling load. It is also necessary to understand how what the local strain distribution during a complete cycle is.

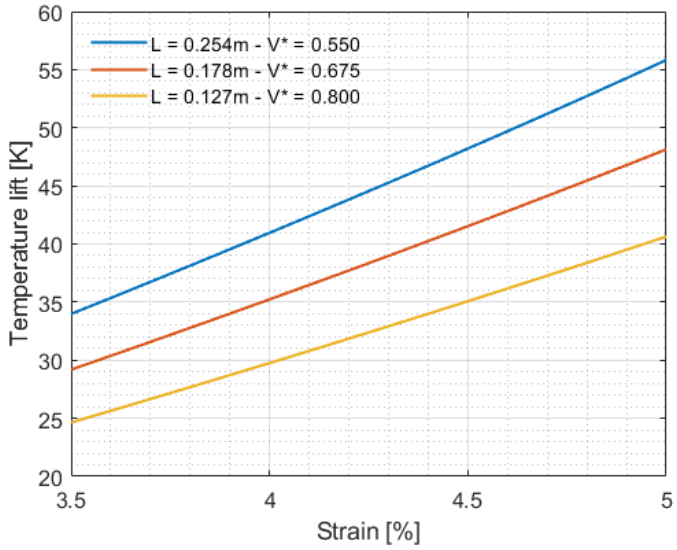

Figure 106: Maximum temperature lift as a function of strain for different regenerator lengths

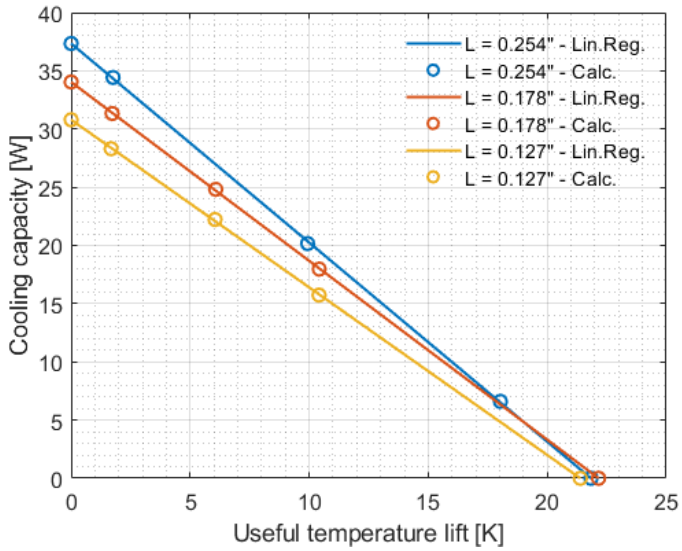

Figure 107: Cooling capacity for different regenerator lengths

Figure 107 shows the cooling capacity and temperature lift performance of the different configurations. There is a reduction in the cooling capacity as the length decreases, even if the strain is increased.

Figure 108 shows, however, that the reduction in cooling capacity does not scale down linearly with the reduction in Ni-Ti mass, in fact is proportionally smaller, so specific cooling capacity (per unit mass) is larger in the shorter regenerators.

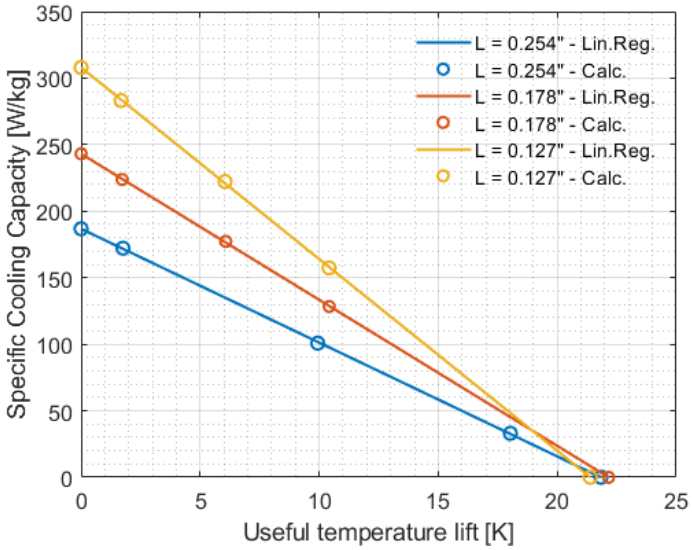

Figure 108: Specific cooling capacity for different regenerator lengths

6.3 Heat transfer fluid choice

Table 10 shows the properties of different heat transfer fluids. In this work the heat transfer fluid is water, which was chosen mainly because of its non-toxicity, availability and good thermal properties. In the case of magnetocaloric devices, water can corrode the magnetocaloric materials so instead of using pure water a mixture of water and different alcohols can prevent corrosion while decreasing the freezing temperature of the mixture. Silicone oil was selected because it is often used in various thermal applications. Different studies on magnetocaloric cooling systems concluded that the best cooling performance is achieved with liquid metals specially at high operating frequencies, while among other fluids water showed the best performance. Because of its low toxicity, Galinstan was selected over other liquid metals. Galinstan is a brand name for an alloy composed of 68.5 wt.% Ga, 21.5 wt.% In, and 10.0 wt.% Sn which melts at −19 °C (−2 °F) and is thus liquid at room temperature (Kitanovski et al., 2015).

Table 10: Properties of different working fluids (Kitanovski et al., 2015)

	Heat capacity	Density	Thermal conductivity	Thermal diffusivity	Dynamic viscosity
	$[J.kg^{-1}K^{-1}]$	$[kg.m^{-3}]$	$[Wm^{-1}K^{-1}]$	$[m^2s^{-1}]$	[Pa.s]
Water	4,180	998	0.599	1.44×10^{-7}	1.00×10^{-3}
Water + wt. 20% ethanol	4,350	968	0.465	1.10×10^{-7}	2.23×10^{-3}
Water + wt. 50% ethanol	3,470	922	0.342	1.07×10^{-7}	2.31×10^{-3}
Ethylene glycol	2,303	1,120	0.303	1.17×10^{-7}	3.00×10^{-3}
Silicone oil	1,620	855	0.163	1.18×10^{-7}	1.29×10^{-3}
Galinstan	370	6,440	16.05	6.74×10^{-7}	2.40×10^{-3}

The effect of these different working fluids on a one stage active regenerator configuration was studied numerically with the same model and Figure 109 shows the temperature lift as a function of utilization factor for six working fluids.

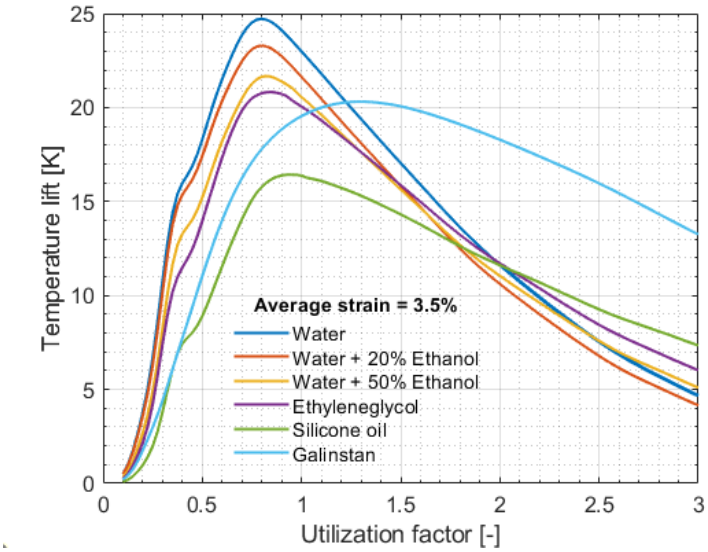

Figure 109: Maximum temperature lift for different heat transfer fluids

For utilization factors smaller than 1.2, the simulation results show that the largest temperature lift is developed using water as a heat transfer fluid. For utilization factors larger than 1.2, the simulation results show that the largest temperature lift is developed using Galinstan. To gain some insight about these results Figure 110 show the effectiveness analysis based on the solution of the idealized passive regenerator (see Figure 12) and the values of the non-dimensional groups NTU_0 and C_r^*. In all three subplots the x-axis is the utilization factor, which is the independent variable. Changing the utilization factor affects both NTU_0 and C_r^* and with each combination is possible to calculate a value of effectiveness.

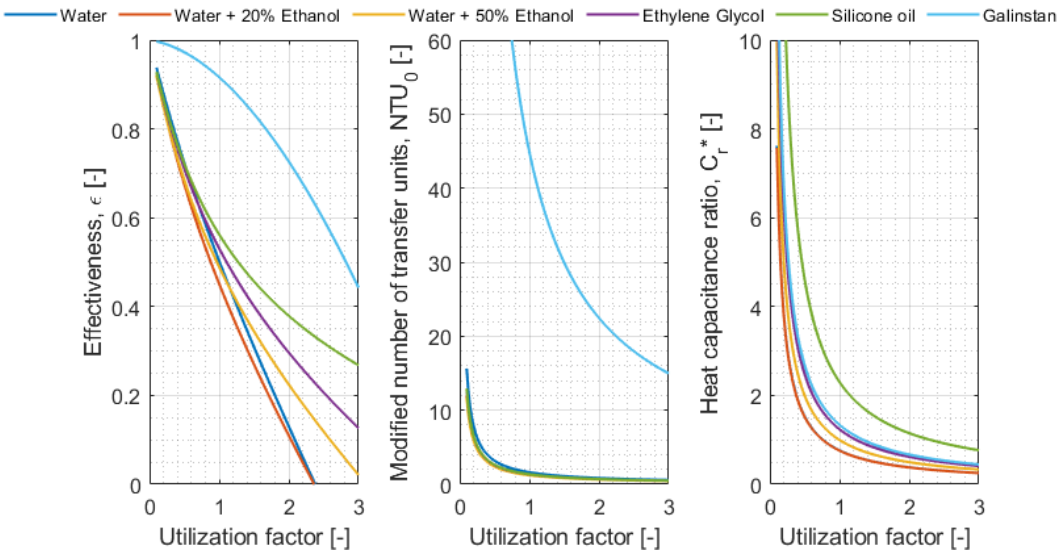

Figure 110: Non-dimensional analysis of ideal passive regenerator performance for six working fluids

As Figure 12 in section 1.2.5 (page 19) shows, for C_r* values larger than 10 the effectiveness is only a function of NTU_0. The effectiveness is higher for Galinstan over the entire range of utilization factor used for the simulation, and the main driver for it is NTU_0, as the subplot in Figure 110 shows.

Figure 111 shows the cooling capacity for water and Galinstan for two values of utilization factor that were determined from Figure 109: 1.2 (where the curves crossed) and 3 (in the regime where Galinstan was above all the working fluids). For V* = 1.2 the figure shows that the cooling performance of water is superior to Galinstan over the entire range of temperatures. For V* = 3, the figure shows that operating the system with Galinstan leads to larger temperature lifts than water at low cooling capacity, but lower cooling capacity than water at lower temperature lift. In general, what the model shows is that Galinstan has a larger operational flexibility, since by increasing flowrate the temperature lift does not get significantly affected and the cooling capacity increases. That is not the case for water.

If we use the area under the cooling capacity curve to quantify with one number the cooling performance, when using water increasing the flow rate does not change the area under the curve, while when using Galinstan, the area is significantly increased.

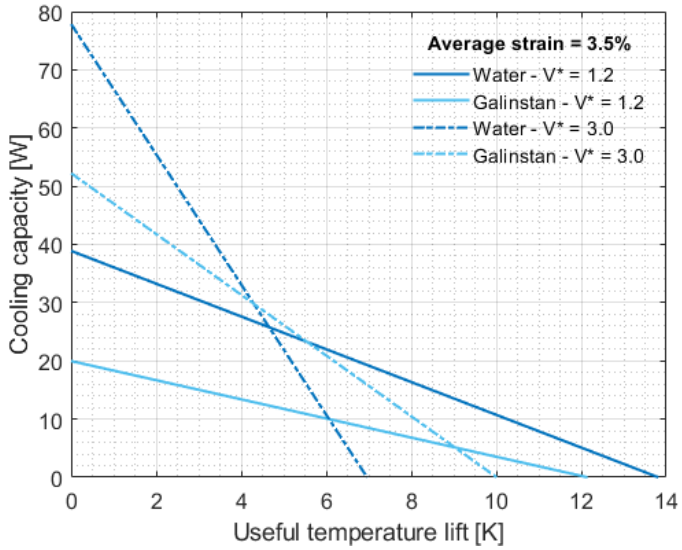

Figure 111: Cooling performance of a one stage system operating with water or Galinstan for two different utilization factors

6.4 Regenerator material

Having a material with a uniform set of transformation temperatures (M_f, M_s, A_s and A_f) along the regenerator causes an inhomogeneous strain distribution once the temperature profile is established. This maldistribution results in several performance degradation mechanisms in one- and multi-stage system configurations. This section studies how an active regenerator with a linear variation of transformation temperatures in the longitudinal direction performs in comparison to an active regenerator with a constant set of transformation temperatures. Figure 112 shows the temperature lift as a function of the utilization factor for a regenerator with a constant set of transformation temperatures and another with a linear variation from A_f to A_f + 34 K for an average strain of 3.5%.

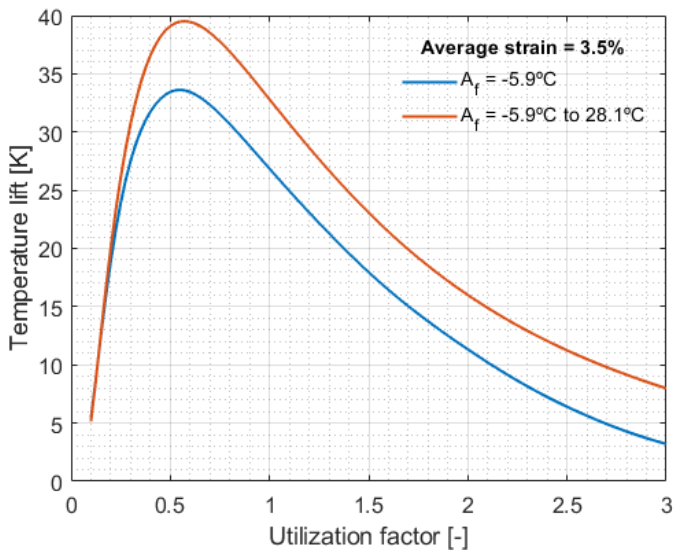

Figure 112: Temperature lift for a uniform-A_f and a variable-A_f regenerator with identical geometry

Under similar operating conditions the temperature lift of the variable transformation temperature regenerator is larger than the one obtained with the constant transformation temperature regenerator by approximately 5 K. This is an improvement close to 10%. Figure 113 shows the difference in local mechanical response after the temperature profile is established. The difference between both regenerators is significant and here is where the most meaningful effect resides. The local mechanical response in the regenerator with the variable transformation temperature is more homogeneous along the length, and this can enable an increase in the average strain. Another significant difference is that the maximum stress that is required to induce the same average strain is smaller for the regenerator with the variable transformation temperature. This is because the material's equilibrium transformation temperature along the regenerator follows closely the local temperature along the regenerator.

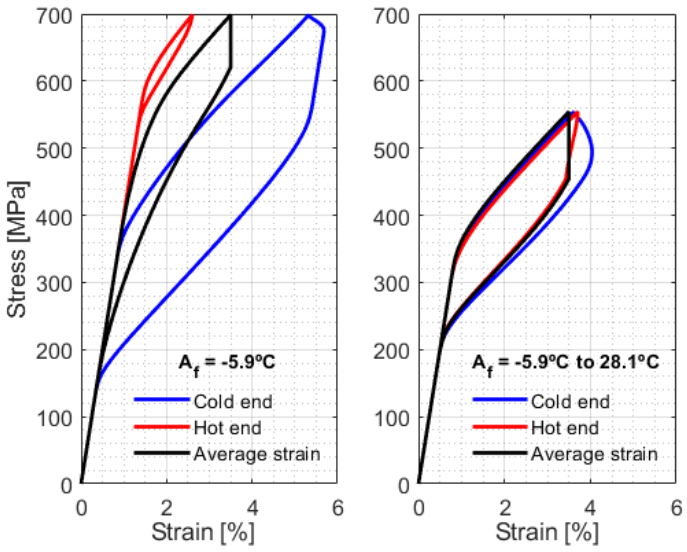

Figure 113: Regenerator mechanical response of a uniform-A_f and a variable-A_f regenerator.

Figure 114 shows how the strain evolves in time during one cycle during steady state and also a metric of the strain inhomogeneity, the standard deviation.

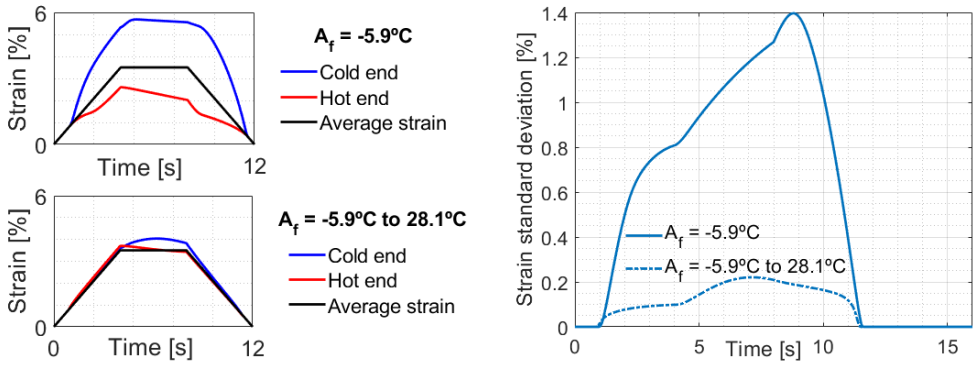

Figure 114: Time variation and standard deviation of strain for a uniform-A_f and a variable-A_f regenerator.

Figure 113 shows that the maximum stress in a regenerator with uniform A_f is larger, which is correct.

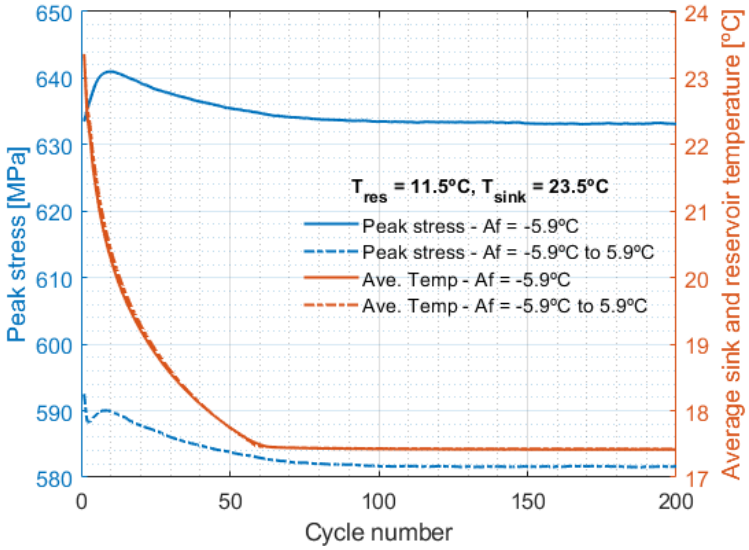

Figure 115: Peak stress as a function of cycle number for a uniform and a variable A_f regenerator.

However, to isolate the effect of the variable A_f from that of the rise in temperature during heat regeneration without heat rejection (which also drives the stress up), the system was simulated to operate between a constant sink and reservoir temperatures to maintain not only a constant temperature difference between them, but also fixed temperatures, so that the average temperatures stays constant. Figure 115 shows that effectively, the maximum stress that is necessary to induce the transformation is lower for the variable A_f regenerator than for the uniform A_f for identical operating conditions.

Figure 116 shows the martensite phase fraction along both regenerators, at two different moments during the cycle: after loading and before unloading. The time between these moments is the heat rejection stage and that is when the local strain is reallocated based on local temperatures and stress. The first case was discussed in Figure 72 and Figure 74. The martensite phase fraction is larger in the cold side of the regenerator and decreases towards the hot side. As heat is rejected and the temperature of the regenerator decreases, the cold side transforms further, promoting a decrease in the stress that causes the hot side to reverse the transformation. The total strain is locally reallocated and made more inhomogeneous. In the second case the dynamic is different. The first observation is that the martensite phase fraction is more homogeneous along the regenerator at around 55%. As heat is rejected the martensitic phase fraction increases all along the regenerator. This can happen as a result of a decrease in the stress and because of that a decrease in the elastic strain, because during the heat rejection period the total strain is remains constant.

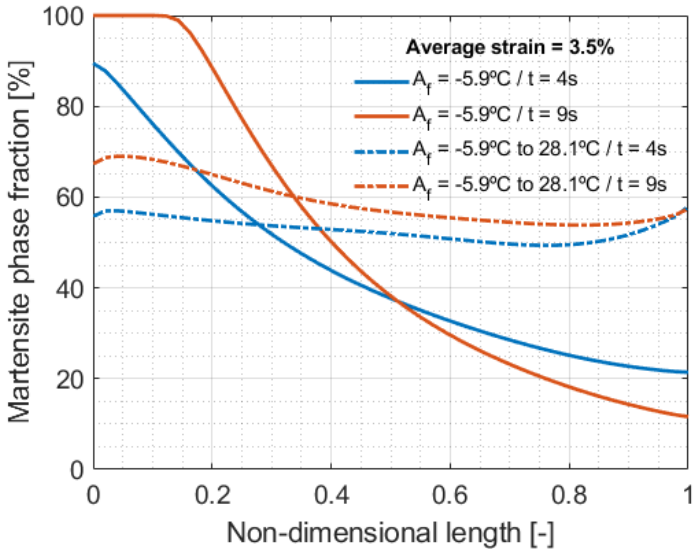

Figure 116: Martensite phase fraction longitudinal distribution for a uniform-A_f and a variable-A_f regenerator.

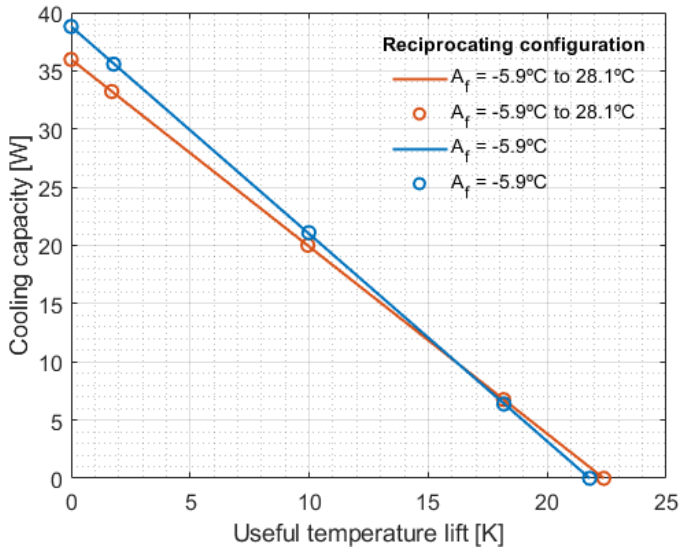

Figure 117: Cooling performance comparison between variable and uniform A_f regenerators.

Figure 117 shows the cooling performance comparison between a set of regenerators with variable A_f and another with uniform A_f. For larger temperature lift, the regenerator with variable A_f produces a larger maximum temperature lift than the one with uniform A_f.

However, for low temperature lift, as it could be expected, the uniform A_f regenerator can produce a larger maximum cooling capacity.

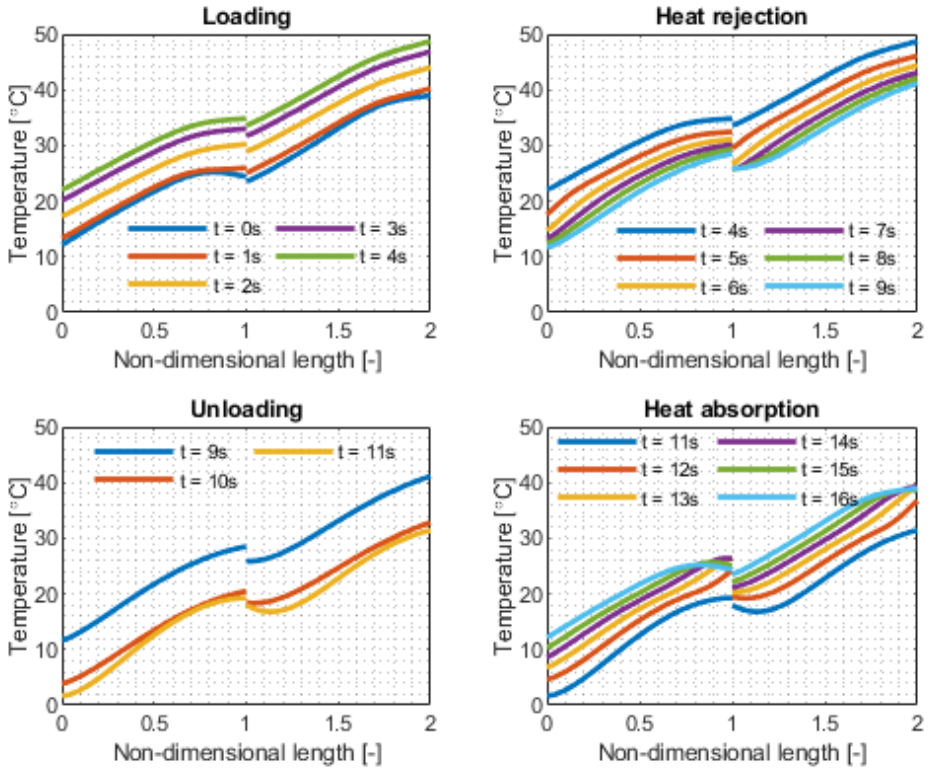

Figure 118: Time evolution of temperature profile during a steady state cycle

In Chapter 3: it was described how the difference in martensite phase fraction along a regenerator caused the large temperature gap between regenerators in the two-stage configuration. Figure 118 is analog to Figure 77 and shows the temperature profiles at different instants in time during a steady state cycle for a variable A_f regenerator. The variation imposed is linear and it is split between both regenerators: for the cold regenerator A_f varies linearly from -5.9ºC to 10.9ºC and for the hot regenerator A_f varies linearly from 10.9ºC to 25.9ºC. It is clear that the temperature gap upon unloading is not present and that

the temperature changes during loading and unloading are more homogeneous. Figure 119 shows a similar behavior as the reciprocating configuration: improved performance at larger temperature lift for the variable A_f regenerator, and the opposite for small temperature lift.

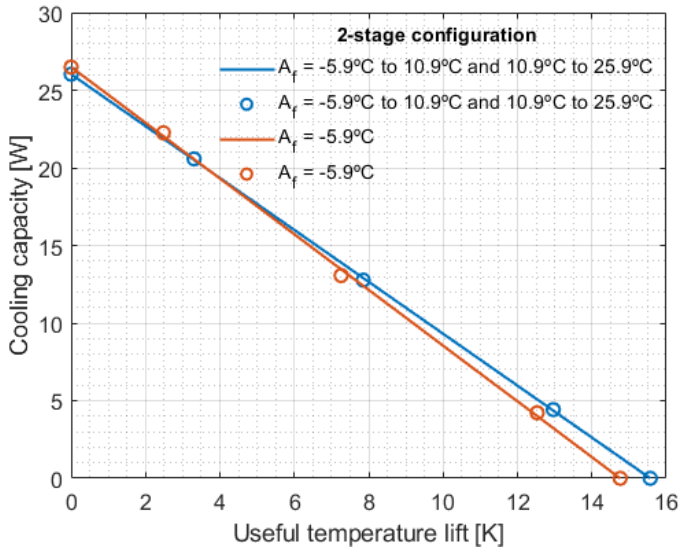

Figure 119: Cooling performance comparison between variable and uniform A_f regenerators

A general observation after comparing the cooling performance of both regenerators, with compositional gradient and without, is that it seems that there is not a significant increase in cooling performance. This is reasonable if we think that for the same average strain it can be expected that there should not be a large difference. When the material has a uniform transformation temperature, the cold side of the regenerator is over strained in comparison to the average strain, and so "over performs" compensating for the hot side of the regenerator. When the material has a variable transformation temperature, all the

regenerator works together around the average strain. The main benefit is the possibility of increasing the strain without premature failure.

6.5 Decreasing load requirements by dynamic operation

The concepts presented in this section originated as an attempt to imagine a system that could be operated at higher frequency, and so the amount of material could be reduced. The original estimation aimed at decreasing the amount of tubes inside a regenerator from 19 to 1, and to increase the operating frequency by 20 (approximating 1 Hz). The next step is to try to operate the system continuously, and add a mass so that the natural frequency of the configuration could be the operating frequency. Due to the limitations of the mathematical model to capture the hysteresis accurately, this section got reduced to the measurement of materials properties to just determine whether the material hysteretic losses are low enough to prevent it from being overdamped.

In dynamics, the spring-mass-damper system is the almost the simplest configuration that can be studied, second only to the spring-mass system. The spring component represents the stiffness. The mass represents the inertia of the system. The damper represents the dissipation of energy. In the schematic shown in Figure 120, the elastocaloric material is represented by the spring and the damper, while the mass is an additional component that was not present in the previous system and now represents the inertial component used to tune the resonance frequency. The reason for it being an oscillating configuration is that the distances a and b, can also be used to affect the rotational inertial component without changing the mass, so that will give the design more degrees of freedom. The behavior of a spring-mass-dashpot system responds to Equation 34 with the assumption of small angle approximation ($\sin\theta \approx \theta$).

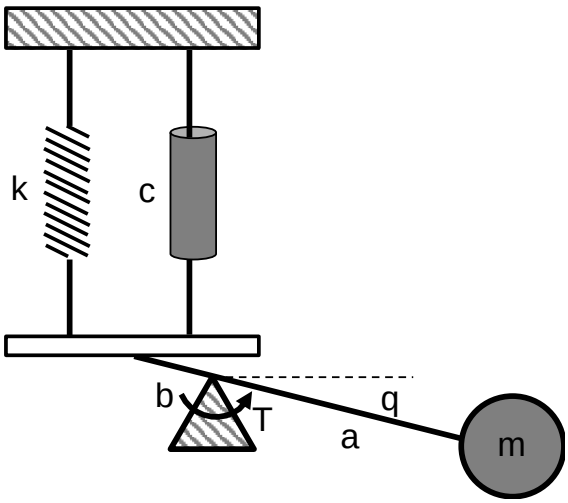

Figure 120: Schematic of a spring-mass-dashpot system. As a starting set of parameters, b = 0.05 m, a = 1 m, m = 25 kg.

$$T(t) = ma^2\ddot{\theta} + cb^2\dot{\theta} + kb^2\theta$$ Equation 34

When a system governed by the differential equation described in Equation 34, and the externally applied torque T(t) is a harmonic function, the forced response of the system is also expected to be harmonic plus or minus a phase shift. If the frequency of application of the external force is very close or equal to the natural frequency of the system, a large amplitude response can be expected. The natural frequency of the system is mostly dependent on the rotational inertia and the stiffness, while the damping will determine the maximum amplitude of the resonant response. One of the main objectives of this section is to determine if the energy dissipated by the phase change will make the system overdamped.

6.5.1 Mechanical behavior of a single tube under constraint

The first step into the study of this concept is to develop the ability to compress a single 0.254m-long tube to high strain without it being susceptible to buckling. Once this is achieved, then the stiffness in a constraint condition similar to an operating condition, can be measured. A test fixture was built to constrain the tube laterally during compression. The lateral constraint was achieved by using three rails with roller bearings. Each rail was located around the tube at 120 degrees from each other, all bearings in contact with the tube and oriented in the longitudinal direction. A linear bearing was used as a guide to ensure a proper alignment between the testing machine actuator, the tube and the position of the rails. In the first design the rails had 11 bearings each, for 11 contact points along the tube. This amount of bearings proved to be insufficient, only allowing to achieve a 3% strain before buckling. In the second design, the rails had 25 bearings each, which proved to be significantly better, allowing to achieve 4% strain.

Figure 121: Photo of the two rails used to constrain the single tube.

Figure 121 shows the two rail structures that were tested. Figure 122 shows the structure placed in the universal testing machine. The tests were done imposing a sinusoidal crosshead displacement, at a frequency of 1 Hz, to different strain levels and the load response was recorded.

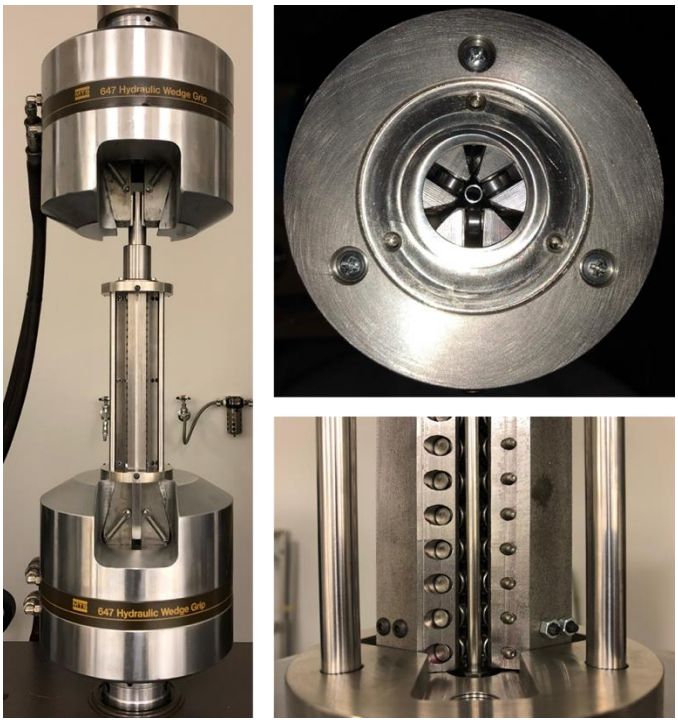

Figure 122: Constraint structure mounted on the testing machine

Figure 123 shows the mechanical response of the single tube. One observation that can be made is that despite the fact that the constraint structure was able to provide the necessary support for the tube to be compressed to 4% strain, ideally it would be desired to reach higher strains, 4.5% to 5%, to be able to take advantage of all the transformation latent heat available. This was not possible, as the material failed by buckling between 4% and 4.5% strain.

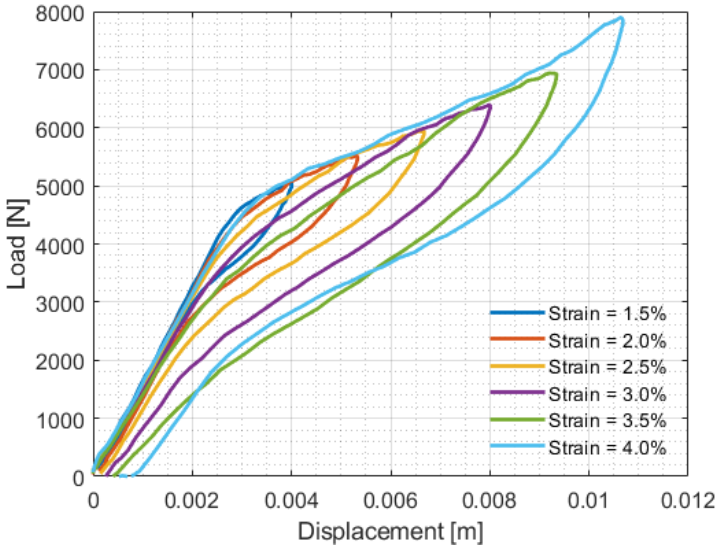

Figure 123: Mechanical response of a single tube laterally contrained between roller structure.

6.5.2 Resonance frequency approximation based on single tube mechanic response

Figure 124 shows a schematic of the geometric configuration of the regenerator arrangement.

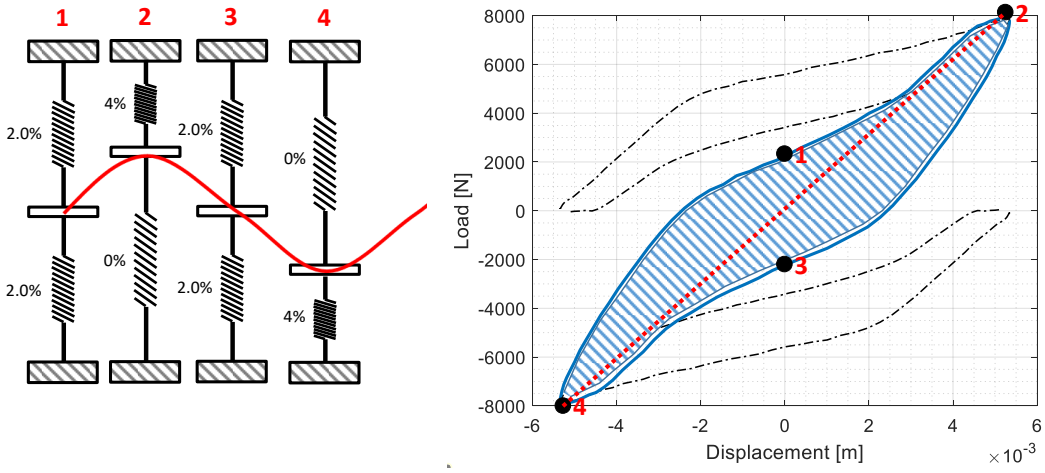

Figure 124: Load-displacement behavior of a two pre-compressed tube arrangement

From the mechanical response of the single tube, it is possible to extrapolate what would be the mechanical response of two, precompressed tubes that as a whole would behave as a spring. The load span divided by the displacement span represent the stiffness of the spring, represented by the dotted red line that connects points 2 and 4 in Figure 124. The area inside the load-displacement loop represents the amount of energy dissipated in each cycle. For a conventional dashpot, the amount of energy dissipated is a function of the velocity. However, studies on the mechanical properties of superelastic alloys show that the mechanical response of the material not dependent of frequency beyond a certain value over which the transformation can be considered to happen adiabatically (Dolce and Cardone, 2001). In that case, the dissipation behavior is similar to a process called "structural damping". In this case the energy dissipated per cycle is approximately proportional to the square of the motion amplitude by it is not dependent on the frequency, as shown in Equation 35:

$$W_d \approx -\alpha \hat{u}^2 \qquad \text{Equation 35}$$

To deal with this it is necessary to introduce the concept of "equivalent dashpot constant, c_{eq}". In the case of a viscous dashpot, the energy dissipated in one cycle can be calculated with the Equation 36, where Ω is the angular frequency of the forcing function:

$$W_d = -\pi c \hat{u}^2 \Omega \qquad \text{Equation 36}$$

The next step is to calculate what needs to be the value of c such that the energy dissipated in one cycle by the viscous dashpot is equal to the energy dissipated by structural damping, which can be seen in Equation 37:

$$\pi c_{eq} \hat{u}^2 \Omega = \alpha \hat{u}^2 \rightarrow c_{eq} = \frac{\alpha}{\pi \Omega} \qquad \text{Equation 37}$$

The dissipated work is equal to the hysteretic area for each maximum displacement (see Figure 125). Next step is to plot W_d against u^2, and from the slope to calculate α, see Figure 126. Once the value of α is known, the value of c_{eq} can be calculated for each frequency. Once the stiffness "k" and the equivalent dashpot coefficient "c_{eq}" are calculated it is possible to solve the differential equation and calculate the dynamic amplification factor as a function of the operating frequency.

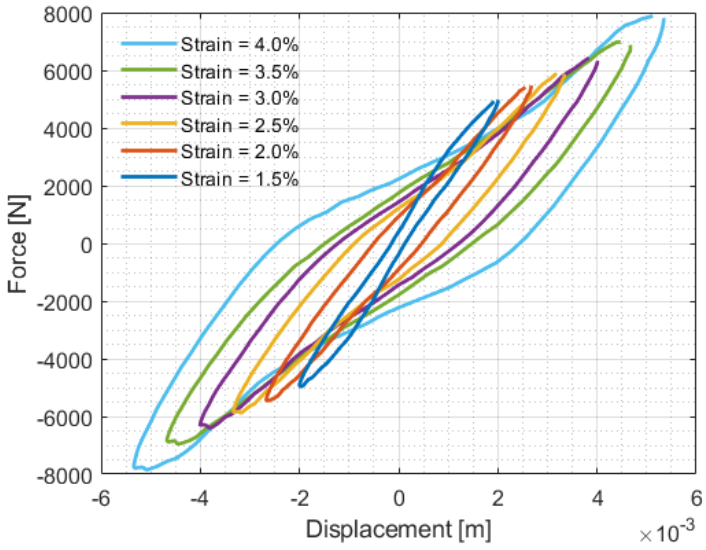

Figure 125: Load-displacement behavior of a two pre-compressed tube for different strains.

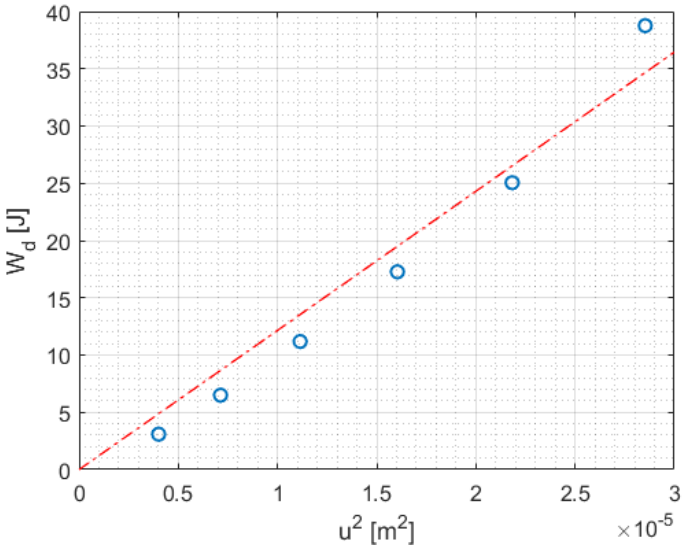

Figure 126: Dissipated energy-maximum displacement squared to calculate equivalent dashpot coefficient.

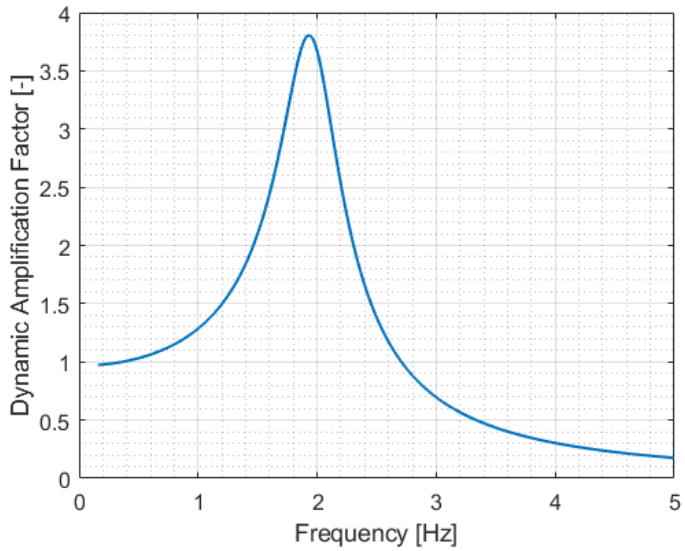

Figure 127: Dynamic Amplification Factor for different frequencies.

The results are shown in the Figure 127. The main result of this calculation is the confirmation that the energy dissipated during the transformation does not make the material behave as an overdamped system. There is a dynamic amplification factor that is

larger than 1, in fact it is almost 4, and the inverse of that coefficient is the factor that will determine how much lower the applied load can be by operating at the resonance frequency instead of operating in a static regime.

Chapter 7: Conclusions

During this dissertation four elastocaloric cooling system configurations were built and studied by measuring the maximum temperature lift and the cooling performance. They were compared to one another and to magnetocaloric cooling systems.

The first system configuration, four reciprocating Ni-Ti heat exchangers with thermo-wave heat recovery, surpassed its predecessor in both temperature lift and cooling capacity by achieving a maximum temperature lift of 8 K in closed-loop and with no heat rejection, and a cooling performance of 5 K maximum useful temperature lift and 120 W maximum cooling capacity in open-loop configuration, all obtained with a 4.5% average strain. From the temperature lift point of view, the system surpassed almost 40% of surveyed magnetocaloric prototypes, from the maximum cooling capacity point of view, 90% of the surveyed magnetocaloric cooling prototypes. For a cooling application, the temperature lift is still low, so increasing the temperature lift was an imperative.

By implementing an active heat regeneration cycle, all three remaining configurations surpassed the previous marks and almost tripled it, achieving a maximum of 21.3 K at 3.5% strain in closed loop. This value is superior to 90% of the surveyed temperature lift values of magnetocaloric cooling systems. With respect to cooling performance, the maximum cooling capacity that was measured was 25 W and the maximum useful temperature lift was 6.7 K, both with an average strain of 3.5%. There is potential for improvement

considering that with a lower strain it was possible to achieve a larger useful temperature lift and these configurations have not been scaled up yet.

Through numerical simulation and experimentation, a fundamental limitation of active elastocaloric regenerator cycles was identified. Once a temperature gradient is established along the regenerator, a material with uniform transformation temperatures will have a non-uniform strain distribution: the low temperature regions will deform more than the high temperature regions. This can limit the applicability limit of the material, because the cold regions will reach the end of the transformation prematurely.

Different strategies for improvement were identified and assessed using a numerical model developed during this dissertation but also using theoretical elements from heat transfer analysis of ideal passive heat regenerators. They showed that the key to performance improvement is related to improving the heat transfer coefficient between the fluid and Ni-Ti by reducing the hydraulic diameter of the flow channels with the use of low thermal mass inserts.

The numerical model was also used to evaluate the performance of hypothetical materials with a transition temperature with the potential of being tuned to the temperature profile developed along the regenerator during operation. When these structures can be developed, a leap in performance will be achieved enabling in principle the increase in average strain that material can be subjected to during operation and minimizing the strain maldistribution. This, however, could limit the operational range to the one the material is

tuned for. It might still be necessary to develop ways to locally limit the strain during operation.

Chapter 8: Future work

8.1 Thin wall stainless-steel inserts with reciprocating configuration and double capacity

The most straight forward way to boost performance of the regenerator is to replace the solid plastic insert with the thin wall stainless steel tube. The challenge is to find a way to keep it centered inside the tube and to seal the end so that water cannot flow inside. One of the benefits of the inscribed polygon shape is that it is self-centering. However, once that technical issue is overcome, there is significant potential for improvement.

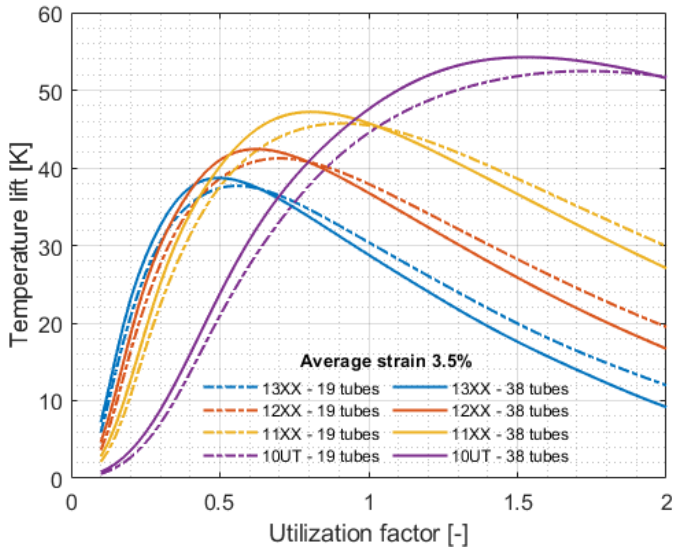

Figure 128: Temperature lift model calculation with thin-wall stainless steel tubes and double amount of tubes

Figure 128 shows the temperature lift of the reciprocating configuration using stainless steel tube inserts instead of plastics, for an arrangement of two reciprocating regenerators, and four reciprocating regenerators (two and two). The gains in temperature lift by doubling up the amount of tubes are not significant, but they are with respect to cooling capacity according to Figure 129.

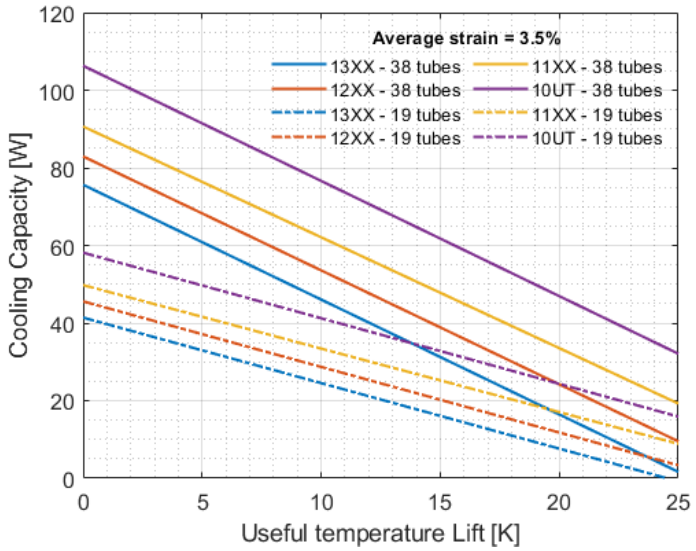

Figure 129: Cooling performance model calculation with thin-wall stainless steel tubes and double amount of tubes

8.2 Reassess regenerator structural specification

As it was shown in previous sections, the regenerator experiences failure at around 4.5% strain. Two mechanisms seem to be competing, buckling and strain maldistribution. Based on the experimental observations, it seems that buckling could be more critical. Decreasing the regenerator length not only would improve the critical buckling load of the regenerator,

but also reduce the total displacement to induce the same strain than in a longer regenerator. Once the total displacement is reduced, the exposed length of the tube is also reduced (what is not constrained by the stainless-steel tube) and that could help in preventing buckling and decoupling both phenomena. It would be important to ensure the tube holder can be compressed to the maximum strain consistently.

8.3 Optimize connecting tubing length, diameter and material combination

Figure 130 shows an example of how the length of the connecting tubing (or the volume) can affect temperature lift and cooling performance.

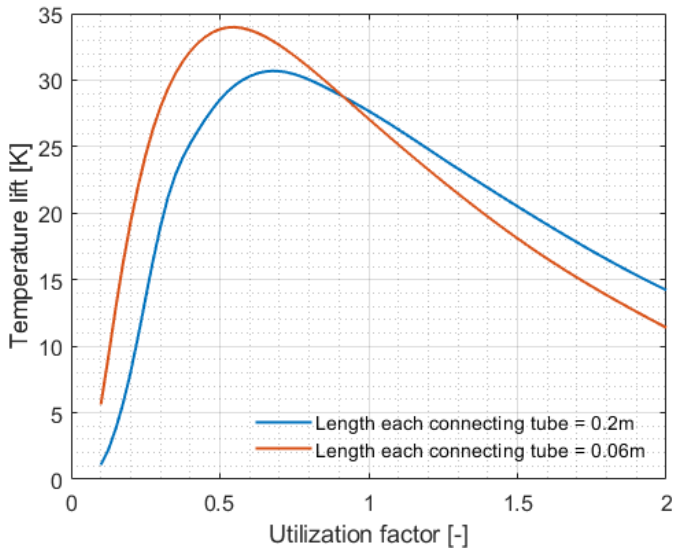

Figure 130: Effect of connecting tubing length in temperature lift performance

Having shorter connecting tubing (or a smaller volume between the loading head and the heat sink or reservoir requires less fluid to be displaced before the water can leave the regenerator and make it past the solenoid valve. This allows the regenerator to operate at a lower utilization factor and higher effectiveness, so the maximum temperature lift

increases. However, for larger utilization factors the temperature lift that can be obtained is larger for the configuration with the longer connecting tubing.

8.4 Upgrade superelastic material thermodynamic model

The single-crystal material model that was used in this work was a very efficient tool to understand the phenomena taking place in an elastocaloric active regenerator. The actual material, is a polycrystalline material, so the behavior cannot be completely captured, as it was shown how it did not represent hysteresis accurately. An computationally effective alternative that has been implemented and requires the experimental determination of some parameters (Qian et al., 2018) (Heintze and Seelecke, 2008).

Chapter 9: Contributions

During the duration of this project the following contributions to the field have been done:

A large scale elastocaloric regenerator system was built, operated and tested. All prototypes currently being tested in other countries are miniature size.

A two-stage regenerator system was built, operated and tested. There are no reports of such device having been built anywhere else.

Parts of the work done here was reported in conference papers.

David Catalini, Yunho Hwang, ICR 2019 International Congress of Refrigeration, “Recent advances in elastocaloric cooling technologies: Where they stand and what prospects are”.

David Catalini, Nehemiah Emaikwu, Jan Muehlbauer, Suxin Qian, Yunho Hwang, Reinhard Radermacher, Ichiro Takeuchi, 2018 MRS Fall Meeting and Exhibit, Symposium TP01: Caloric Materials for Highly Efficient Cooling Applications, “Design and Operation of a 100 W Elastocaloric Compression-Based Active Regenerator”.

Hou, Huilong, Jun Cui, Suxin Qian, David Catalini, Yunho Hwang, Reinhard Radermacher, and Ichiro Takeuchi. "Overcoming fatigue through compression for advanced elastocaloric cooling." MRS Bulletin 43, no. 4 (2018): 285-290.

Other parts of the work is in the revision stage for a journal publication about inhomogeneous strain distribution and solutions to address it.

A publication about a summary of the test results is in the process of being written.

Appendix A

Table A-1 shows all the surveyed data about magnetocaloric cooling systems used in Introduction.

Table 11: Temperature lift and cooling capacity surveyed data for magnetocaloric cooling systems

	ΔT [K]	CC [W]		ΔT [K]	CC [W]		ΔT [K]	CC [W]		ΔT [K]	CC [W]
[1]	47	0	[9]	0	60	[16]	7	20	[31]	2	190
[2]	11	0		2	50		14.5	15		10	150
[3]	28	0		3	40		19.5	10		15	100
	20	2		4	30		10.5	20		15.5	50
	9	5		4.5	20		16	15		16	0
[4]	7	550		5.5	10		22	10		3	300
	8	510		7.5	0		14	20		13	200
	10	450		0	50		19.5	15		17	100
	12	320		1	40		22.5	10		17.5	0
	8	575		2	30		13	20.5		2	350
	10	600		3	20		17.5	15.5		14	250
	11	565		4	10		22	10		18	120
	12	560		5	0		11.5	30		19	0
	13	480	[10]	7	1		25.5	16		2	350
	15	400		4	8		29.5	10		14	250
	16	380	[11]	19	0		14	30.5		18	120
	18	300		16	1.2		22.5	20		18.5	0
	20	225		14	2		30.5	10		5	320
	21	200		12	3.2		14.5	32		10	270
	23	110		7	5.2		27.5	20.5		18	170
[5]	1.6	0		5	7.2		35	10		20	100
[6]	7	30		15.5	0		16	37		22	0
	9	20		14	1.2		31	20		5	300
	11	10		12	2.1		36.5	10		16	200
	13	0		11	3.6		7	14		21	100
	14	40		8.5	4.9		13	10		24	0
	17	20		7	7.2		16.5	6	[32]	0	3.5

	20	0	[12]	50	0		15	14		0.8	2.7
	25	40		46	2		20	10		1.5	1.25
	27	20		40	4		23	6		2.2	0.6
	23	100		34	6		8	25		2.7	0
	30	60		28	8		19	17		0	2.25
[6a]	16	0.8		21	10		25	10		1.25	1.25
[6a]	13.5	0.8	[12]	47	0	[16]	9	28	[32]	2.1	0.6
	15	0.8		43	2		22	18		3	0
	18	0.8		40	4		29	10		0	1.75
	18	0.8		36	6		11	30		0.5	1.25
	14	0.8		30	8		24	18		1.6	0.75
	23	0		23	10		31	10		3	0
	13	1.4		41	0		15	21	[33]	9	0
	13	2.8		37	2		20	16.5		8.5	20
	13.5	2.9		34	4		23	10		7.5	40
	13.5	3		31	6		15	31.5		6	60
	14.5	2.6		27	8		24	21		4	80
	14.5	2.2		22	10		29	10		3	100
	14	2	[13]	5	0		13	40.5		9	0
[7]	13	0	[14]	3	17		29	21		8	20
	18	0		3	15		33.5	10		6	40
	20	0		3	14		12.5	44		5	60
[8]	19	0		3	14		33	21		2.7	80
	15	5		3	14.5		37	10		1	100
	9	10		3	11.5		10	48		7	0
	0	15		3	7		35	21		6.8	20
	22.5	0		3	7		40	10		5.6	40
	20.5	10		3	6.5		16	30		4	60
	11.5	19		3	7		23	20		1.8	80
	0	28		3	6		27	10	[34]	0	54
	25	0		3	16.5		18	39		2.5	47
	22	13		3	17		29	20		4.5	40
	14	27		3	19		32	10		7	34.5
	1	41		3	17.5		13	51		11.5	27.5
	18	0		3	17		33	20		15.5	19.5
	14	15		3	17		36	10		18	12.5
	8	29		3	16		15	50		19	8
	1	44		3	16		31	32		0	40

	24.5	0		3	11		39.5	10		4.5	34
	21.5	13		3	0		18	51		9.5	28
	14	27		3	1		32.5	32		16	23
[8]	1	41	[14]	3	2	[16]	40.5	10	[34]	20	13
	18	0		3	7	[22]	24	0		23	8
	14	16		3	6	[24]	8	0		25	5
	7.5	32	[15]	10.5	0	[25]	16	0		0	27
	1	49		8	0.5	[27]	23	0		7.5	23
[9]	0.25	25		7	1		16	20		17	17.5
	1	20		6	1.2		11	30		23	13
	4	10		4	2		7	40		26	7
	6.5	0	[16]	6	9	[29]	7	0		29	5
	0.25	45		10.5	6		4.4	0.35		0	20
	1.5	40		13	3		2.6	0.7		3.5	18.5
	3	30		6	16.5		6.6	0		15	14
	4.75	20		13	11		4.8	0.35		23	9
	6	10		18	6		3.2	0.7		27	6
	7.5	0		7	20		5.8	0		30.5	4.5
	0.5	60		13	15		4.8	0.35		0	14.5
	1.5	50		18	10		5	0		12	13
	3	40		10.5	20		1.8	0.35		22	7
	4	30		16	15		4.8	0		26	6
	5.5	20		22	10		3	0.35		31	3
	6.5	10		10	22	[30]	20	0		0	9
	7.5	0		15	16		16	60		10.5	8.5
	0	20		21	10		10	100		13	7.5
	1	10		11	25		8	120		23.5	5
	3	0		18	17.5		5	140		28.5	3
	0	40		24	10	[31]	8.5	324	[37]	0	200
	1.5	30		7	20		2.9	498		2.5	160
	3	20		13	15		13.8	400		6	100
	5	10		18	10		3.1	746		9	50
	6	0					0.3	1010		11	0
										0	110
										2	90
										3	85
										6	55
										8.5	0

[1] (Brown, 1976)

[2] (Kirol and Dacus, 1988)

[3] (Green et al., 1990)

[4] (Zimm et al., 1998)

[5] (Bohigas et al., 2000)

[6] (Hirano, 2003)

[6a] (Blumenfeld, 2003)

[7] (A. M. Rowe, 2003)

[8] (Zimm et al., 2006)

[9] (Okamura et al., 2006)

[10] (Clot et al., 2003)

[11] (Richard et al., 2004)

[12] (A. Rowe and Tura, 2006)

[13] (Shir et al., 2005)

[13a] (Vasile and Muller, 2006)

[14] (Gao et al., 2006)

[16] (Yao et al., 2006)

[15] (Kawanami and Sakurai, 2007)

[22] (Nakamura et al., 2008)

[24] (Dupuis et al., 2009)

[25] (Kim and Jeong, 2010)

[27] (Tura and Rowe, 2011)

[28] (Arnold et al., 2014)

[29] (K. Engelbrecht et al., 2011)

[30] (Eriksen et al., 2015)

[31] (K. Engelbrecht et al., 2012)

[32] (Trevizoli et al., 2011)

[33] (Lozano et al., 2016)

[34] (Trevizoli et al., 2016)

[37] (Aprea et al., 2016)

Bibliography

Aprea, C., Cardillo, G., Greco, A., Maiorino, A., and Masselli, C. (2016). A rotary permanent magnet magnetic refrigerator based on AMR cycle. *Applied Thermal Engineering*. https://doi.org/10.1016/j.applthermaleng.2016.01.097

Arnold, D. S., Tura, A., Ruebsaat-Trott, A., and Rowe, A. (2014). Design improvements of a permanent magnet active magnetic refrigerator. *International Journal of Refrigeration*. https://doi.org/10.1016/j.ijrefrig.2013.09.024

Blumenfeld, P. E. (2003). *High temperature superconducting magnetic refrigeration*. https://doi.org/10.1063/1.1472124

Bohigas, X., Molins, E., Roig, A., Tejada, J., and Zhang, X. X. (2000). Room-temperature magnetic refrigerator using permanent magnets. *IEEE Transactions on Magnetics*. https://doi.org/10.1109/20.846216

Brantley, W., Berzins, D., Iijima, M., Tufekçi, E., and Cai, Z. (2017). *1 - Structure/property relationships in orthodontic alloys* (T. Eliades and W. A. B. T.-O. A. of B. Brantley (eds.); pp. 3–38). Woodhead Publishing. https://doi.org/https://doi.org/10.1016/B978-0-08-100383-1.00001-1

Brown, G. V. (1976). Magnetic heat pumping near room temperature. *Journal of Applied Physics*, *47*(8), 3673–3680. https://doi.org/10.1063/1.323176

Bruederlin, F., Ossmer, H., Wendler, F., Miyazaki, S., and Kohl, M. (2017). SMA foil-based elastocaloric cooling: from material behavior to device engineering. *J. Phys. D: Appl. Phys*. https://doi.org/10.1088/1361-6463/aa87a2

Clot, P., Viallet, D., Allab, F., Kedous-Lebouc, A., Fournier, J. M., and Yonnet, J. P.

(2003). A Magnet-Based Device for Active Magnetic Regenerative Refrigeration. *IEEE Transactions on Magnetics*. https://doi.org/10.1109/TMAG.2003.816253

Cui, J., Wu, Y., Muehlbauer, J., Hwang, Y., Radermacher, R., Fackler, S., Wuttig, M., and Takeuchi, I. (2012). Demonstration of high efficiency elastocaloric cooling with large ΔT using NiTi wires. *Applied Physics Letters*, *101*(7), 73904. https://doi.org/10.1063/1.4746257

Dolce, M., and Cardone, D. (2001). Mechanical behaviour of shape memory alloys for seismic applications 2. Austenite NiTi wires subjected to tension. *International Journal of Mechanical Sciences*, *43*(11), 2657–2677. https://doi.org/10.1016/S0020-7403(01)00050-9

Dupuis, C., Vialle, A. J., Legait, U., Kedous-Lebouc, A., and Ronchetto, D. (2009). New investigations in magnetic refrigeration device, AMR cycle and refrigerant bed performance evaluation. *Third IIF-IIR International Conference on Magnetic Regrigeration at Room Temperature, Thermag I, Des Moines, Iowa, USA*.

Engelbrecht, K., Bahl, C. R. H., and Nielsen, K. K. (2011). Experimental results for a magnetic refrigerator using three different types of magnetocaloric material regenerators. *International Journal of Refrigeration*. https://doi.org/10.1016/j.ijrefrig.2010.11.014

Engelbrecht, K., Eriksen, D., Bahl, C. R. H., Bjørk, R., Geyti, J., Lozano, J. A., Nielsen, K. K., Saxild, F., Smith, A., and Pryds, N. (2012). Experimental results for a novel rotary active magnetic regenerator. *International Journal of Refrigeration*. https://doi.org/10.1016/j.ijrefrig.2012.05.003

Engelbrecht, Kurt, Tušek, J., Eriksen, D., Lei, T., Lee, C. Y., Tušek, J., and Pryds, N.

(2017). A regenerative elastocaloric device: Experimental results. *Journal of Physics D: Applied Physics*. https://doi.org/10.1088/1361-6463/aa8656

Eriksen, D., Engelbrecht, K., Bahl, C. R. H., Bjørk, R., Nielsen, K. K., Insinga, A. R., and Pryds, N. (2015). Design and experimental tests of a rotary active magnetic regenerator prototype. *International Journal of Refrigeration*. https://doi.org/10.1016/j.ijrefrig.2015.05.004

Gao, Q., Yu, B. F., Wang, C. F., Zhang, B., Yang, D. X., and Zhang, Y. (2006). Experimental investigation on refrigeration performance of a reciprocating active magnetic regenerator of room temperature magnetic refrigeration. *International Journal of Refrigeration*. https://doi.org/10.1016/j.ijrefrig.2005.12.015

Greco, A., Aprea, C., Maiorino, A., and Masselli, C. (2019). A review of the state of the art of solid-state caloric cooling processes at room-temperature before 2019. *International Journal of Refrigeration*, *106*, 66–88. https://doi.org/https://doi.org/10.1016/j.ijrefrig.2019.06.034

Green, G., Chafe, J., Stevens, J., and Humphrey, J. (1990). Gadolinium-terbium active regenerator. In *Advances in Cryogenic Engineering*.

Heintze, O., and Seelecke, S. (2008). A coupled thermomechanical model for shape memory alloys-From single crystal to polycrystal. *Materials Science and Engineering A*. https://doi.org/10.1016/j.msea.2007.08.028

Hirano, N. (2003). *Development of magnetic refrigerator for room temperature application*. https://doi.org/10.1063/1.1472125

Kawanami, T., and Sakurai, K. (2007). Cooling performance of room-temperature magnetic refrigerator with active magnetic regenerator (numerical analysis on cooling

performance). *Nihon Kikai Gakkai Ronbunshu, B Hen/Transactions of the Japan Society of Mechanical Engineers, Part B*. https://doi.org/10.1299/kikaib.73.2323

Kim, Y., and Jeong, S. (2010). Investigation on the room temperature active magnetic regenerative refrigerator with permanent magnet array. *AIP Conference Proceedings*. https://doi.org/10.1063/1.3422444

Kirol, L. D., and Dacus, M. W. (1988). Rotary recuperative magnetic heat pump. *Advances in Cryogenic Engineering*. https://doi.org/10.1007/978-1-4613-9874-5_92

Kirsch, S.-M., Welsch, F., Michaelis, N., Schmidt, M., Wieczorek, A., Frenzel, J., Eggeler, G., Schütze, A., and Seelecke, S. (2018). NiTi-Based Elastocaloric Cooling on the Macroscale: From Basic Concepts to Realization. *Energy Technology*, *6*(8), 1567–1587. https://doi.org/10.1002/ente.201800152

Kitanovski, A., Tušek, J., Tomc, U., Plaznik, U., Ožbolt, M., and Poredoš, A. (2015). Magnetocaloric Energy Conversion. In *Green Energy and Technology*. https://doi.org/10.1007/978-3-319-08741-2

Kittel, C. (1969). *Thermal Physics* (1st editio). John Wiley and Sons.

Lozano, J. A., Capovilla, M. S., Trevizoli, P. V., Engelbrecht, K., Bahl, C. R. H., and Barbosa, J. R. (2016). Development of a novel rotary magnetic refrigerator. *International Journal of Refrigeration*. https://doi.org/10.1016/j.ijrefrig.2016.04.005

Nakamura, K., Kawanami, T., Hirano, S., Ikegawa, M., and Fumoto, K. (2008). Improvement of room temperature magnetic refrigerator using air as heat transfer fluid. *2008 2nd International Conference on Thermal Issues in Emerging Technologies, ThETA 2008*. https://doi.org/10.1109/THETA.2008.5167187

Okamura, T., Yamada, K., Hirano, N., and Nagaya, S. (2006). Performance of a room-

temperature rotary magnetic refrigerator. *International Journal of Refrigeration*. https://doi.org/10.1016/j.ijrefrig.2006.07.020

Ossmer, H., Wendler, F., Gueltig, M., Lambrecht, F., Miyazaki, S., and Kohl, M. (2016). Energy-efficient miniature-scale heat pumping based on shape memory alloys. *Smart Materials and Structures*. https://doi.org/10.1088/0964-1726/25/8/085037

Otsuka, K., and Wayman, C. M. (1999). *Shape memory materials*. Cambridge university press.

Qian, S. (2015). *Development of thermoelastic cooling systems*.

Qian, S., Geng, Y., Wang, Y., Muehlbauer, J., Ling, J., Hwang, Y., Radermacher, R., and Takeuchi, I. (2016). Design of a hydraulically driven compressive elastocaloric cooling system. *Science and Technology for the Built Environment*. https://doi.org/10.1080/23744731.2016.1171630

Qian, S., Ling, J., Hwang, Y., Takeuchi, I., and Radermacher, R. (2015). Modeling and Optimization of a Novel Heat Recovery Design for Thermoelastic Cooling Systems. *Volume 6B: Energy*. https://doi.org/10.1115/IMECE2015-52624

Qian, S., Yuan, L., Hou, H., and Takeuchi, I. (2018). Accurate prediction of work and coefficient of performance of elastocaloric materials with phase transformation kinetics AU. *Science and Technology for the Built Environment*, *24*(6), 673–684. https://doi.org/10.1080/23744731.2018.1457411

Qian, S., Yuan, L., Yu, J., and Yan, G. (2017). Numerical modeling of an active elastocaloric regenerator refrigerator with phase transformation kinetics and the matching principle for materials selection. *Energy*. https://doi.org/10.1016/j.energy.2017.09.116

Richard, M. A., Rowe, A. M., and Chahine, R. (2004). Magnetic refrigeration: Single and multimaterial active magnetic regenerator experiments. *Journal of Applied Physics*. https://doi.org/10.1063/1.1643200

Rowe, A. M. (2003). *Design of an active magnetic regenerator test apparatus*. https://doi.org/10.1063/1.1472121

Rowe, A., and Tura, A. (2006). Experimental investigation of a three-material layered active magnetic regenerator. *International Journal of Refrigeration*. https://doi.org/10.1016/j.ijrefrig.2006.07.012

Rowe, Andrew. (2012). Thermodynamics of active magnetic regenerators: Part II. *Cryogenics*, *52*(2), 119–128. https://doi.org/https://doi.org/10.1016/j.cryogenics.2011.09.007

Seelecke, S., and Müller, I. (2004). Shape memory alloy actuators in smart structures: Modeling and simulation. *Applied Mechanics Reviews*, *57*(1), 23–46. http://dx.doi.org/10.1115/1.1584064

Shah, R. K., and Sekulic, D. P. (2003). *Fundamentals of heat exchanger design*. John Wiley and Sons.

Shir, F., Mavriplis, C., Bennett, L. H., and Torre, E. Della. (2005). Analysis of room temperature magnetic regenerative refrigeration. *International Journal of Refrigeration*. https://doi.org/10.1016/j.ijrefrig.2004.08.015

Trevizoli, P. V., Barbosa, J. R., and Ferreira, R. T. S. (2011). Experimental evaluation of a Gd-based linear reciprocating active magnetic regenerator test apparatus. *International Journal of Refrigeration*. https://doi.org/10.1016/j.ijrefrig.2011.05.005

Trevizoli, P. V., Nakashima, A. T., Peixer, G. F., and Barbosa, J. R. (2016). Performance

evaluation of an active magnetic regenerator for cooling applications – part I: Experimental analysis and thermodynamic performance. *International Journal of Refrigeration*.

Tura, A., and Rowe, A. (2011). Permanent magnet magnetic refrigerator design and experimental characterization. *International Journal of Refrigeration*. https://doi.org/10.1016/j.ijrefrig.2010.12.009

Tušek, J., Engelbrecht, K., Eriksen, D., Dall'Olio, S., Tušek, J., and Pryds, N. (2016). A regenerative elastocaloric heat pump. *Nature Energy*. https://doi.org/10.1038/nenergy.2016.134

Vasile, C., and Muller, C. (2006). Innovative design of a magnetocaloric system. *International Journal of Refrigeration*. https://doi.org/10.1016/j.ijrefrig.2006.07.016

Wollants, P., Roos, J. R., and Delaey, L. (1993). Thermally- and stress-induced thermoelastic martensitic transformations in the reference frame of equilibrium thermodynamics. *Progress in Materials Science TA - TT -*, *37*(3), 227–288. https://doi.org/10.1016/0079-6425(93)90005-6 LK - https://umaryland.on.worldcat.org/oclc/4648535118

Yao, G. H., Gong, M. Q., and Wu, J. F. (2006). Experimental study on the performance of a room temperature magnetic refrigerator using permanent magnets. *International Journal of Refrigeration*. https://doi.org/10.1016/j.ijrefrig.2006.07.010

Yu, B., Liu, M., Egolf, P. W., and Kitanovski, A. (2010). A review of magnetic refrigerator and heat pump prototypes built before the year 2010. *International Journal of Refrigeration*, *33*(6), 1029–1060. https://doi.org/https://doi.org/10.1016/j.ijrefrig.2010.04.002

Zimm, C., Boeder, A., Chell, J., Sternberg, A., Fujita, A., Fujieda, S., and Fukamichi, K. (2006). Design and performance of a permanent-magnet rotary refrigerator. *International Journal of Refrigeration*. https://doi.org/10.1016/j.ijrefrig.2006.07.014

Zimm, C., Jastrab, A., Sternberg, A., Pecharsky, V., Gschneidner, K., Osborne, M., and Anderson, I. (1998). Description and Performance of a Near-Room Temperature Magnetic Refrigerator. In *Advances in Cryogenic Engineering*. https://doi.org/10.1007/978-1-4757-9047-4_222